Universidade do Minho
Escola de Ciências

Maria do Carmo Mourato Leitão Vinagre Lucas

Polymeric-based ternary solid-state electrolytes for Lithium-ion batteries. Computer modeling of solid-state batteries

October 2023

Polymeric-based ternary solid-state electrolytes for lithium-ion batteries. Computer modeling of solid-state batteries

Maria Lucas

UMinho | 2023

Universidade do Minho
Escola de Ciências

Maria do Carmo Mourato Leitão Vinagre Lucas

Polymeric-based ternary solid-state electrolytes for Lithium-ion batteries. Computer modeling of solid-state batteries

Master's Dissertation
Mestrado em Ciências e Tecnologias do Ambiente – Energia

Work accomplished under the supervision of:
Doutor Carlos Miguel Silva Costa
Professora Maria Teresa Mesquita Cunha Machado Malheiro

October 2023

Direitos de autor e condições de utilização do trabalho por terceiros

Acknowledgements

It is with great pride that I acknowledge that the final stage of my two-year master's is close to its end, and the sense of fluffiness is overwhelming. I hope my thesis will live up to the expectations of the excellent scientific work that is performed both at the University of Minho and at Aalto University, where I have completed my master's thesis.

Firstly I would like to thank my advisors, who granted me the opportunity to enroll in this journey, my Master's thesis. In this year Prof. Carlos guided me through his electrochemical knowledge, always supporting my journey in academic writing. His ambition, work ethic, and the unceasing urge to fight for me and my dreams were definitely determinants in this journey, without him I would not be able to get where I am today. He is someone unparalleled and is among those who have exceptionally well-crafted work, and made me a better scientist. Prof. Stéphane is the most committed, hard-working, and organized person that I have come across which reflects the unraveling work he pursues with his high prestige, definitely someone I look up to in both the scientific world and personally. Prof. Maria who is a committed, kind, highly motivated person and definitely indispensable in this project, her work with me was patient and angel wordy. Definitely, an incredible woman who shared her knowledge of mathematics and never stopped giving me the greatest advice.

A special acknowledgment to the wonderful EECG group. It was a privilege to work in this group, everybody will always have time to help you in all types of matters. From simulations to laboratory assistance, I was always in good hands, and for that, I will be forever grateful to EECG. The working force of this group was only achieved thanks to Prof. Tanja Kallio, your strong sense of leadership and organization are the foundation ground for the unraveling work you have made. I will never forget Sara Pakseresht, I have great respect for her work. She revealed to be more than a lab buddy, but a true friend, who supports me in every situation. I have learned a lot from you, and believe I have become a better scientist and person thanks to you.

To my family, my mother especially, who always sacrificed herself in many different ways so that I could have everything effortlessly, she is my biggest supporter, my inspiration, the best mother, the strongest person I know, and my greatest friend, words cannot describe how I fell for you. To my late father, I wonder if you would be proud of who I became, as your dream was always to see me fulfilled and happy. A special thanks to my siblings.

To my closest friend, Gabriela, who has always been in every step of my life, it has been wonderful to share these experiences with you. Hopefully, we can share many more moments for the rest of our lives. From our walks to late nights studying, I would not choose anything else in the world besides your friendship.

To my boyfriend and best friend Bernardo, who is definitely the smartest person I have come across. You have turned my world upside down, changing me and my perspective in these last years, thank you for making me more ambitious, and always bringing out the best in me. Thank you for your patience, support, and for believing in me even when I did not.

Statement of integrity

I hereby declare having conducted this academic work with integrity. I confirm that I have not used plagiarism or any form of undue use of information or falsification of results along the process leading to its elaboration. I further declare that I have fully acknowledged the Code of Ethical Conduct of the University of Minho.

University of Minho, 31st October 2023

Name: Maria do Carmo Mourato Leitão Vinagre Lucas

Signature: _____

Resumo

A crescente exigência energética requer a toma de medidas ao nível tecnológico, nomeadamente o desenvolvimento de aparelhos com capacidade de armazenamento de energia, como é o caso das baterias. Hoje em dia as baterias de ião-lítio ainda representam um perigo à sociedade pois são aparelhos que, devido à sua constituição com uma componente liquida, tem alguns riscos associados. A busca por uma solução de modo a mitigar as desvantagens associadas às baterias comerciais culmina nos eletrólitos em estado sólido. Os eletrólitos sólidos ternários de base polimérica mostram ser uma aposta relevante.

Este trabalho aborda a síntese de novos materiais (eletrólitos sólidos) para baterias de próxima geração. Por conseguinte, foram sintetizados eletrólitos sólidos com uma base polimérica dopados com partículas cerâmicas (BTO, BST e PZT) e líquido iónico, de modo a se obter uma melhor performance destes materiais. Posteriormente as características físicas, morfológicas e eletroquímicas foram estudadas. O liquido iónico detem a capacidade de melhorar a condutividade ionica em eletrólitos sólidos, tornando-os mais eficientes na condução de iões Litío, o que é crucial em dispositivos de armazenamento de energia. Por outro lado, as particulas cerâmicas reforçam a matriz sólida do eletrólito, melhorando sua resistência mecânica e estabilidade térmica. A componente experimental foi acompanhada por uma secção teórica que permitiu um conhecimento mais profundo sobre o funcionamento da bateria. O modelo formulado foi baseado na componente física da bateria, o qual foi elaborado de raiz contribuindo para um profundo conhecimento da componente numérica associada à bateria.

Apartir deste estudo foi percétivel uma bénefica influência tanto por parte das particulas cerâmicas e do liquido iónico, promovendo uma melhor performance da bateria, obtendo-se uma condutividade iónica na ordem dos 1.34×10^{-5} S/cm, complementada por uma performance ao nível da capacidade muito próxima da teórica. O desempenho da bateria com os componentes BST/IL e BTO/IL mostrou-se bem-sucedido em ciclagens de longa duração, mantendo uma capacidade e estabilidade elevadas. No entanto, ao aplicar taxas de descarga variáveis, a amostra BST/IL destacou-se com resultados superiores, demonstrando uma maior estabilidade em comparação com as outras amostras. A componente teórica sempre de forma paralela permite o enriquecimento dos processos físicos que dominam a componente experimental.

Concluindo, neste trabalho foram desenvolvidos electrolitos sólidos com excelente performance, paralelamente o desenvolvimento teórico foi imprescindível para uma melhor compreensão dos mecanismos que promovem o funcionamento de baterias de estado solido. Tudo isto é essencial para a sintese e uma contínua progressão na próxima geração de electrólitos sólidos.

Palavras-chave: Eletrólitos em estado sólido, polímero (PVDF-HFP), liquido iónico, Cerâmicas, bateriais de ião litio, modelos numérico, métodos numéricos.

Abstract

The increasing demand for energy necessitates technological measures, particularly the development of energy storage devices such as batteries. Nowadays, lithium-ion batteries still pose a risk to society due to their liquid component. The quest for a solution to mitigate the drawbacks associated with commercial batteries leads to solid-state electrolytes. Ternary solid polymer electrolytes prove to be a promising area of study.

This work addresses the synthesis of new materials (solid-state electrolytes) for next-generation batteries. Consequently, solid-state electrolytes were synthesized based on a polymer matrix doped with ceramic particles (BTO, BST, and PZT) and an ionic liquid, aiming to enhance their performance. Subsequently, their physical, morphological, and electrochemical characteristics were studied. The ionic liquid has the capacity to improve ionic conductivity in solid-state electrolytes, making them more efficient in conducting lithium ions, which is crucial in energy storage devices. On the other hand, ceramic particles reinforce the solid electrolyte matrix, enhancing its mechanical strength and thermal stability.

The experimental component was complemented by a theoretical section, providing a deeper understanding of battery operation. The formulated model was based on the physical aspects of the battery and was developed from the ground up, contributing to a comprehensive understanding of the numerical aspects associated with the battery. From this study, a beneficial influence of both ceramic particles and the ionic liquid was evident, leading to improved battery performance. Ionic conductivity on the order of 1.34×10^{-5} S/cm was achieved, accompanied by a capacity performance very close to the theoretical values. The battery's performance with BST/IL and BTO/IL blend proved to be successful in long-life cycling, bearing a high capacity and stability. Whereas when applying varying C-rates, the BST/IL blend stood out with superior results, revealing higher stability, when compared to the other samples. The theoretical component, running in parallel, enriches the understanding of the physical processes governing the experimental component.

In conclusion, this work resulted in the development of solid-state electrolytes with excellent performance. Simultaneously, the theoretical development was indispensable for a better comprehension of the mechanisms driving the operation of solid-state batteries. All of this is essential for synthesis and the continuous advancement of the next generation of solid-state electrolytes.

Keywords: Solid-state electrolytes, polymer (PVDF-HFP), ionic liquid, ceramics, lithium-ion batteries, numerical models, numerical methods.

Table of contents

List of Figures

List of tables

List of Acronyms

BTO	Barium Titanate Oxide
BTCS	Backward in Time Centered in Space
BST	Barium Strontium Titanade
CA	Chronoamperometry
CPE	Constant Phase Element
DNF	Doyle-Newman-Fuller
DMF	N, N-dimethyl formaldehyde
DSC	Differential Scanning Calorimetry
EDS	Energy Dispersive Analysis of X-rays
EIS	Electrochemical Impedance spectroscopy
EVs	Electric Vehicles
FWHM	Full Width at Half Minimum
FTCS	Forward in Time Centered in Space
FTIR-ATR	Fourier Transformed Infrared Spectroscopy – Attenuated Total Reflectance
HR-SEM	High Resolution – Scanning Electron Microscopy
IL	Ionic Liquid
Li^+	Lithium Ion
LiPON	Lithium Phosphorous Oxy – Nitride
LISICON	Lithium Super Ionic CONductor
LFP	Lithium Iron Phosphate

NASICON	NAtrium SUper Ionic CONductor
NWs	Nanowires
PE	Polyetylene
PEO	Polyethylene Oxide
PVDF	Poly(vinylidene Flouride)
PVDF – HFP	Poly(vinylidene Flouride–co–hexafluoropropylene)
PZT	Lead Zirconate Titanate
SPM	Single Particle Model
SPMe	Single Particle Model with electrolyte
SSE	Solid State Electrolyte
TGA	Thermogravimetric Analysis
TSFI	Triflimidate
XRD	X-Ray Diffraction

List of Symbols

k_a	Activity of the anode
k_c	Activity of the cathode
k_s	Activity of the solid electrolyte
i_a	Anode current density
i_i	Bulk current density
$\mathcal{F}_a$	Bulk ionic flux
ϕ_a	Bulk ionic potential
i_a	Cathode current density
i_c	Cathode current density
L	Characteristic size of the cell
C_{Li}	Density of lithium in the anode
C_{Ox}	Density of oxide in the cathode
D	Diffusion coefficient
D_a	Diffusion coefficient in the anode
D_c	Diffusion coefficient in the cathode
A_a	Effective area of the anode
A_a	Effective area of the cathode
i_i	Exchange current density
G_a	Exchange ion density in the anode
G_c	Exchange ion density in the cathode
R_{ext}	External resistance
j_c	Flux in the anode
j_c	Flux in the cathode
R	Gas constant

I	Intensity
I_a	Intensity at the anode current collector
I_c	Intensity at the cathode current collector
κ_a	Ionic mobility in the anode
κ_c	Ionic mobility in the cathode
k_{a0}	Kinetic rate constant in the anode
k_{c0}	Kinetic rate constant in the cathode
α_a	Kinetic transfer power in the anode
α_c	Kinetic transfer power in the cathode
t^+	Lithium Transfer number
$C_{Li_{max}}$	Maximum density of Lithium
$C_{Ox_{max}}$	Maximum density of the oxide
η	Overpotential
η_a	Overpotential in the anode
η_c	Overpotential in the cathode
ε_a	Porosity of the anode
ε_c	Porosity of the cathode
ϕ_a	Potential in the anode
ϕ_a	Potential in the cathode
P_a	Predictor source term of the anode
P_c	Predictor source term of the cathode
R_s	Radius of the grain structure
s_a	Source term in the anode
s_c	Source term in the anode

S_a	Specific active length in the anode
S_c	Specific active length in the cathode
I_{tot}	Total current
v	Velocity

Chapter 1

Introduction

This chapter introduces the dissertation's main theme. It includes introductory context on the theme. Also contains a succinct approach to theoretical notes and chemical properties of solid-state batteries, explaining the basic principles and components of solid-state electrolytes, are approached. Finally, the thesis objectives and structure.

Introduction

1.1 Energy storage systems

With the increased energy consumption from society, it is urgent to find a solution to the depletion of resources caused by the growth in energy exhaustion. The need for energy storage systems worldwide has become increasingly critical due to several key factors. One may mention the production of carbon dioxide (CO_2) due to the burning of fossil fuels is a major contributor to climate change and global warming. To mitigate these harmful emissions, there is a growing demand for alternative energy storage systems. Fossil fuels, such as coal, oil, and natural gas, are the primary sources of CO_2 emissions in energy production. By shifting to alternative energy storage systems, we can reduce our dependence on fossil fuels for electricity generation (Association, 2022).

The transition to renewable energy sources like wind and solar power is expanding. Energy storage systems are essential for storing excess energy generated during periods of high renewable energy production, which can be used when energy generation is low, ensuring a stable and reliable power supply, energy storage also allows for time-shifting energy production from renewables (News, 2019). Excess energy generated during the day can be stored and used during the night, aligning energy supply with demand patterns.

There are other crucial factors that come to mind that reinforce the need to invest in energy storage systems, such as maintaining grid stability by providing rapid-response solutions to balance supply and demand. They help mitigate issues such as grid congestion, voltage fluctuations, and frequency deviations. Also, energy storage helps reduce peak demand on power grids by supplying stored energy during peak usage hours, thus preventing blackouts and reducing strain on infrastructure. Finally, nowadays the world is surrounded by electrical devices, of course, emphasizing the growth of electric vehicles, for these energy storage systems are needed for fast and efficient charging infrastructure, ensuring that electric vehicles are a viable transportation option.

The increased energy consumption demands an equally fast growth in the usage of different energy resources. The answer to reducing imbalances between societal energy consumption and energy production has been relying on energy storage systems. These systems demand changes through technology development in order to work towards a solution. The energy storage systems range from quick responses to longer-duration solutions based on supply and demand seasonal variations known in advance.

The different types of energy storage technologies can be divided into the following categories: magnetic systems; electrochemical systems; mechanical systems; hydro systems; pneumatic systems; and thermal systems (Olabi & Abdelkareem, 2021). This work will be focused on electrochemical systems, specifically in batteries as an energy storage technology.

1.1.1 Lithium based batteries: evolution

In the past decades, electrochemical technology has suffered significant evolution due to its continuous demand for applications. In the domain of rechargeable battery technology, the Lithium-ion galvanic cell stands as the preeminent choice. This preference arises from the remarkable characteristics of Lithium-ion electrode chemistries, which yield the highest recorded volumetric and gravimetric energy density in the field. The trajectory of Lithium-ion cell technology has been chiefly propelled by the portable electronics sector in its nascent stages. The substantial energy density inherent to Lithium-ion batteries has facilitated the downsizing of electronic devices, ushering in the era of compact and intelligent gadgets such as smartphones and tablets (Blomgren, 2016).

The evolution of Lithium-ion technology has, in more recent times, spurred advancements directed primarily toward electric vehicles (EVs). This includes both plug-in EVs and full EVs, which are anticipated to consume a significant share, exceeding 50%, of the total production of lithium-ion batteries. In the context of EVs, the primary driving forces are energy density and power density. Additionally, there is a growing demand for stationary energy storage solutions, particularly for localized or home-based storage. This burgeoning demand has redirected research and development efforts toward cost reduction, prolonged battery lifespan, and enhanced safety measures (X. Chen & Vereecken, 2019) (OU, 2017). Remarkably, since its commercial debut by Sony in 1991, the energy density of high-energy Lithium-ion batteries has witnessed a twofold increase, advancing from 100 Wh/kg (250 Wh/L) to 200 Wh/kg (500 Wh/L) (Nishi, 2014). This substantial enhancement can be chiefly attributed to the introduction of innovative electrode chemistries with augmented Lithium ion capacity and refinements in electrode formulations.

On the other hand, solid-state electrolytes offer the potential to establish the required electrochemical range, exemplified by materials like lithium phosphate glass with nitrogen doping, such as LiPON, which demonstrates stability within the voltage range of 0 V to 5.5 V vs. Li^+/Li (Quartarone & Mustarelli, 2011). This suggests a promising alternative. Unfortunately, the primary challenge in adopting solid-state electrolytes lies in the scarcity of materials that combine both sufficiently high Li-ion conductivity (> 10 mS/cm) and a sufficiently broad

electrochemical window (< 0.2 V and > 4.5 V). As an example, LiPON (Guo et al., 2022) exhibits an ionic conductivity ranging from 10^{-7} to 10^{-6} S/cm, limiting its application to all-solid-state thin-film micro batteries, where the sub-micron thickness of the electrolyte film mitigates cell resistance (Dudney, 2005). Encouragingly, recent advancements have been achieved in the field of solid-state electrolytes, particularly for high-capacity powder-based batteries.

1.1.2 Basic Principles Solid State lithium-based batteries

A general composition lithium-ion battery consists of three key elements, a cathode, an anode, and, in the case of solid-state batteries, a solid-state electrolyte (SSE), which is used to conduct ions between the cathode and the anode. The voltage of a battery arises from disparities in the electrochemical potentials at its two electrodes. In the discharge state, when the battery is connected to an external circuit, a reduction reaction occurs at the cathode (the positive electrode). In contrast, an oxidation reaction takes place at the anode (the negative electrode). These reactions yield the output voltage and current for the circuit. Conversely, in the charging state, the reactions undergo a reversal process.

The one-dimensional segment extending from the starting point at the negative current collector (x_{ac}) to the endpoint at the positive current collector (x_{cc}) is comprised of three distinct regions: the negative composite electrode, the separator, and the positive composite electrode. This configuration is visually represented in Figure 1, illustrating a schematic representation of an LFP half cell.

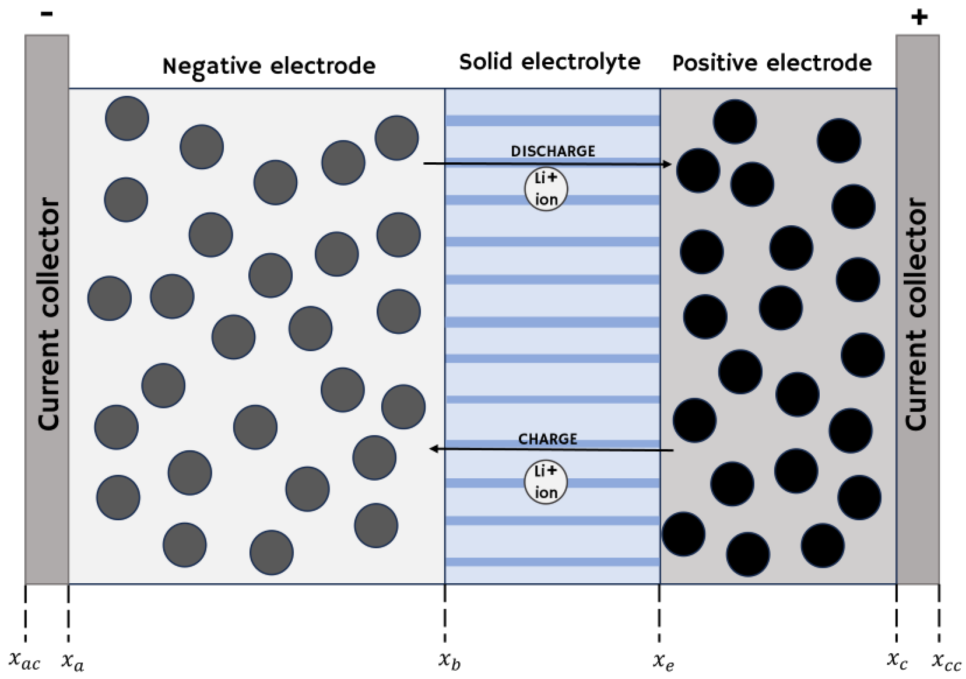

Figure 1: Illustration of a LFP half-cell with a solid-state electrolyte

Charging and discharging process

In a lithium-ion battery with a solid-state electrolyte, the charge and discharge processes involve the movement of lithium ions (Li^+) between the positive and negative electrodes, along with corresponding electron flow through the external circuit. During the charging process, an external voltage source is applied to the battery, creating an electric potential difference. The battery voltage is from the difference in the electrochemical potential of the two electrodes. At the negative electrode (anode), lithium ions are stored within a host material, lithium metal. As the battery charges, Li^+ ions are extracted from the cathode material.

The extracted Li^+ ions move through the solid-state electrolyte, which is typically a solid lithium-conductive material. The solid-state electrolyte allows the transport of Li^+ ions while preventing the passage of electrons, ensuring the electrical separation of the electrodes. The Li^+ ions migrate through the solid-state electrolyte towards the negative electrode (anode) under the influence of the applied voltage. At the negative electrode (anode), the Li^+ ions are inserted into a host material, often graphite. Simultaneously, electrons are released at the anode due to the electrochemical reactions, and they flow through the external circuit to the cathode, creating an electric current. The overall process during charging involves the migration of Li^+ ions from the cathode to the anode and the storage of energy in the form of chemical potential energy.

During the discharging process, when the battery is providing power to an external device, the reverse of the charging process occurs. Li^+ ions are extracted from the anode material and migrate through the solid-state electrolyte toward the cathode. Electrons are released at the anode and travel through the external circuit to the cathode, providing electrical power to the device. At the cathode, Li^+ ions are inserted into the host material, releasing the energy stored during charging as electrical energy to power the device. In the course of charging and discharging, an oxidation reaction occurs at the positive electrode, and simultaneously a reduction reaction takes place at the negative electrode, at the charge moment, and vice versa at the discharge mark. This can be characterized by the following equations (M.-K. Tran, DaCosta, Mevawalla, Panchal, & Fowler, 2021):

$$\textbf{Anode} \quad Li_nC_6 \rightleftharpoons C_6 + nLi^+ + ne^- \tag{1.1}$$

$$\textbf{Cathode} \quad Li_{m-n}FePO_4 + nLi^+ + ne^- \rightleftharpoons Li_mFePO_4 \tag{1.2}$$

$$\textbf{Overall} \quad Li_nC_6 + Li_{m-n}FePO_4 \rightleftharpoons Li_0C_6 + Li_mFePO_4 \tag{1.3}$$

Considering the reaction in this half-cell in the equations above, it is important to recognize the relation between mass and the amount of electrical charge. This is supported by Faraday's law of electrolysis. For instance in equation 1.1, for each mole of material of Li_nC_6, n moles of electrons are released. As a result, the quantity of electric charge matches the electric charge of n moles of electrons. Expressing it mathematically, we can determine

the electric charge of one mole of electrons as follows (Torabi & Ahmadi, 2020):

$$F = N_A \times q_e \tag{1.4}$$

Where N_A is the Avogadro's number, and q_e (C) is the charge of one electron (Torabi & Ahmadi, 2020). The electric charge carried by one mole of electrons is referred to as Faraday's Constant, represented by the symbol F. The Faraday constant is measured in Coulombs per mole ($Cmol^{-1}$). The primary benefit of Faraday's law lies in its ability to establish a connection between the mass-produced and the electrical charge generated (Torabi & Ahmadi, 2020).

Another important parameter in electrochemistry is the Butler-Volmer law. A brief explanation is as follows. In the state of equilibrium, an electrode reaches its maximum potential, which is referred to as the reversible potential. However, when an electrode experiences an electric current, its potential decreases due to its electrochemical properties. Basic chemical principles dictate that the rate at which reactants, denoted as j, are consumed is directly proportional to the concentration of active substances present at the reaction site. Therefore, for the forward (j_f) and backward (j_b) reactions in Equation (1.5), the reaction rates are determined as follows (Torabi & Ahmadi, 2020),

$$j_f = k_f C_{Ox}, \quad j_b = k_b C_{Red} \tag{1.5}$$

where k_f and k_b represent the forward and backward reaction rates, and C_{Ox} and C_{Red} are their corresponding concentrations of active materials. In an equilibrium state, where the net current rate is zero, $j_f = j_b$. However, when a net current flows through the cell, the forward reaction predominates at the cathode, while the backward reaction is more dominant at the anode (Torabi & Ahmadi, 2020).

According to Faraday's law, the current density is directly proportional to the rate of mass production. Consequently, the net current density produced by a single electrode can be defined as follows (Torabi & Ahmadi, 2020).

$$i = nF(j_f - j_b) \tag{1.6}$$

The equilibrium state, where the forward and backward current densities are equal, is termed the exchange current density and is denoted as i_0. The exchange current density is a crucial physical characteristic of each material. A material with a higher exchange current density is considered more active than one with a lower current density. In practical terms, a higher i_0 indicates a faster electrode, capable of producing more electrons in a shorter period (Torabi & Ahmadi, 2020).

Another formula for the total current density can be obtained by introducing the Gibbs free energy formula. The following formula is obtained through several steps of simplification (Torabi & Ahmadi, 2020):

$$i = i_0 \left(exp\left[-\frac{\alpha_{Red} nF(V - V_r)}{RT} \right] - exp\left[\frac{\alpha_{Ox} nF(V - V_r)}{RT} \right] \right) \tag{1.7}$$

This represents the Butler-Volmer equation, which provides the kinetic rate for each electrode. Analyzing the Butler-Volmer equation, we can infer that when the system reaches equilibrium with V equaling V_r, the rates of electron generation and consumption at a single electrode are in balance. In such a state, we can conclude that there is neither net current being produced nor consumed by the electrode. However, when the electrode undergoes charging or discharging, one of the forward or backward reactions takes precedence, causing V to deviate from its reversible value. The disparity between the actual potential and its reversible value ($\eta = V - V_r$) is termed the overpotential and serves as the primary driving force responsible for electrons entering or exiting the electrode. It's important to note that the Butler-Volmer equation is applied separately to each electrode, and in a battery cell comprising positive and negative electrodes, two distinct Butler-Volmer equations should be formulated for each (Torabi & Ahmadi, 2020). Additionally, the i_0 can differ in the anode and the cathode.

1.1.3 Components of a Solid-State Lithium Ion Battery

A battery is an electrochemical device whose chemical reactions create a flow of current in a circuit transforming chemical energy into electrical energy. A Solid-State battery is composed of three primary elements, a cathode, an anode (that constitutes the two electrodes), and a solid electrolyte. The anode is usually associated with a porous material by nature, for instance, graphite and metal oxide for the cathode (Cheruvally, 2008).

Anode

An anode in a lithium-ion battery should possess specific materials and characteristics to function effectively. Some fundamental characteristics that an anode material should bear are, a high capacity to store and release lithium ions during charge and discharge cycles, maintain structural stability over repeated cycling to prevent degradation and ensure long battery life, withstand the expansion and contraction that occurs during lithium insertion and extraction without breaking or deteriorating. Materials with minimal volume expansion during lithium intercalation are preferred to avoid mechanical stress and maintain electrode integrity, and an effective anode material should have good electrical conductivity to facilitate electron transfer during charge and discharge.

Different types of materials are considered, such as Carbon-Based Materials, Silicon and Silicon Alloys, or Metallic Anodes. Graphite is commonly used as an anode material in lithium-ion batteries due to its stability and ability to intercalate lithium ions. Other carbon-based materials like hard carbon and graphene are also explored for their high capacity and cycling stability (Cheruvally, 2008). Silicon has a high theoretical capacity for lithium storage, making it an attractive anode material. Silicon alloys (e.g., silicon-graphite composites) are used to mitigate volume expansion issues during cycling (Hirono et al., 2021). Some emerging technologies explore metallic anodes like lithium metal, which can provide high energy density. However, managing dendrite growth and ensuring safety are key challenges with metallic anodes (Hirono et al., 2021).

Cathode

Regarding the cathode material, there are also some characteristics that enable reliable and efficient battery performance, including, efficient electron and ion transport within the cathode material is essential for rapid charging and discharging, exhibits minimal voltage fade, meaning the voltage remains relatively stable during cycling, have a high capacity to store and release lithium ions during the charge and discharge cycles, contributing to the battery's energy density, high-rate capability, meaning the cathode should deliver high power output without significant degradation, and able to maintain their structural stability over multiple charge and discharge cycles to ensure the longevity of the battery.

A cathode in a lithium-ion battery should have specific materials, the most common are transition metal oxides like lithium cobalt oxide ($LiCoO_2$), lithium manganese oxide ($LiMn2O_4$), and lithium iron phosphate ($LiFePO_4$). These materials provide high energy density and stability (Doeff, 2012). Additionally, Layered Oxides, are another material option, as they can store and release lithium ions efficiently, contributing to high performance in lithium-ion batteries (Chakraborty, Dixit, Aurbach, & Major, 2018). Finally phosphates, like Lithium iron phosphate ($LiFePO_4$), are known for their safety and stability, making them a suitable cathode material for applications where safety is crucial, such as in electric vehicles (Doeff, 2012). Some of the most commonly used cathode materials are Lithium Nickel, Manganese Cobalt oxide, Manganese spinel, Cobalt Oxide, Titanate, and Iron phosphate (Cheruvally, 2008).

Solid electrolytes

Solid electrolytes, often used in advanced battery technologies like solid-state batteries, possess distinct characteristics that set them apart from traditional liquid electrolytes. Some key characteristics of solid electrolytes are, their safety as they are non-flammable and less prone to leakage compared to liquid electrolytes, enhancing the safety of battery systems, exhibit chemical stability, reduction of the risk of unwanted reactions with electrode materials, and extension of the lifespan of batteries, can operate efficiently over a broader temperature range, making them suitable for extreme conditions, including high-temperature and low-temperature environments and finally they have a high energy density, that is possible due to thinner separators and reduced risk of thermal runaway (Liang, 1973) (Choudhury & Patterson, 1971).

Solid electrolytes come in various chemistries, including ceramics, polymers, and composites, offering versatility for different applications. Some of the most common types of solid electrolytes are Oxide based-solid electrolytes (Garnet type, NASICON-Type, and Perovskite-Type), Sulfide-based Solid Electrolytes (LGPS and $Li_7P_3S_{11}$), and finally Polymer-based Solid electrolytes (Polyethylene Oxide (PEO)-Based and Polymer-Ceramic Composite). For this work, a blend with a PVDF co-polymer doped with ceramics and ionic liquid SSE was synthesized and characterized.

1.2 Motivation, objectives and thesis structure

Solid-state electrolytes (SSE) have shown considerable potential when it comes to the next-generation batteries. This area represents an exciting area of research and development with great prospects to revolutionize energy storage and various industries.

For this thesis coupling the experimental procedure with theoretical simulations was crucial in the development and understanding of the solid-state battery mechanism, as the solid-state batteries involve complex processes such as ion transport, interface reactions, and thermal management. Mathematical models help in breaking down these intricate mechanisms, enabling a deeper understanding of the physical and chemical processes within the battery.

Moreover, this work also characterizes the polymeric matrix doped with different fillers (ceramic nanoparticles), evaluating the SSE performance. The fillers have piezoelectric properties, this distinct characteristic will increase stability and enhance the battery's performance overall. The stability of a battery becomes a key parameter since it directly impacts the lifespan of a battery. Unstable batteries degrade more quickly, resulting in reduced capacity and overall longevity. Stable batteries retain their performance characteristics for a longer time. This is an essential characteristic of batteries in general.

The thesis is sectioned into eight chapters. This chapter narrates the background and fundamentals of solid-state Li-ion battery materials. Chapter 2 presents a comprehensive literature review of the major categories of solid electrolytes, and then an insight into which materials are being used in this thesis. It also includes a review of the theoretical models for solid-state batteries. Chapter 3 presents an overview of characterization techniques used in this work as well as the SSE synthesis method.

Chapter 4 includes the development process that was necessary in order to develop the model that was used to simulate the solid-state battery behavior. The formulated model is then presented in Chapter 5.

In Chapter 6, the results are discussed. Which includes a comparison of the different synthesized materials as promising solid electrolytes for Li-ion batteries. An evaluation of the model is also considered in the final section.

Chapter 7 gives a final summary of all the chapters, including major findings and achievements in this thesis study. An outlook for future research in this field is suggested based on the insights obtained from this work.

Chapter 2

Literature Survey

This chapter is divided into three main topics, a research overview and a compilation of the reviewed literature, on both the experimental and theoretical components that this work focuses on. The first section presented the different solid-electrolyte materials that have been in use through time. Additionally, in a separate section, there is the assessed characterization of the materials selected for this study, based on the literature. Finally, in a third segment, research work related to the theoretical models applied to the modulation of solid-state batteries is carried out, differentiating different models applied.

Literature Survey

2.1 State of the art - Solid-State Electrolytes

Solid-state electrolytes (SSE) have gained a lot of interest as they have been showing significant improvement and can become a reliable alternative for liquid electrolytes. SSE are commonly divided into two main groups: inorganic electrolytes and polymer electrolytes. The SSEs that receive the most frequent attention in research are the following (Figure 1):

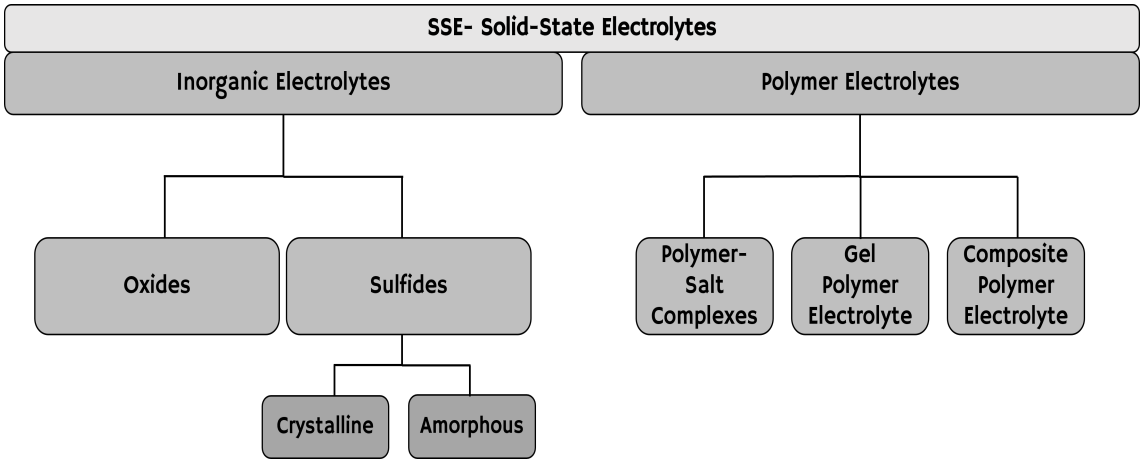

Figure 1: Most common Solid State Electrolytes (SSEs).

The inorganic SSE can be organized into two groups, oxides, and sulfides. The oxide-based SSEs exhibit favorable thermal and electrochemical stability but suffer from limited ionic conductivity and weak mechanical strength, impeding their utilization in energy storage systems. Sulfide-based SSEs have a lower electronegativity and larger atomic size of the S^{2-} ion within the sulfide solid-state electrolyte. This unique combination results in a loose binding of the S^{2-} ion with lithium ions, facilitating the easy transport of lithium ions within the electrolyte. Consequently, sulfide-type solid-state electrolytes exhibit higher lithium-ion conductivity compared to oxide-type solid-state electrolytes at room temperature (Lian et al., 2019).

Specifically, LISICON and NASICON, short for Lithium-Super-Ionic-Conductor and NAtrium SUper Ionic CONductor, respectively, are two distinct types of interesting Li-ion electrolytes. While they were expected to deliver high performance, they achieved conductivities of approximately 10^{-3} S/cm. However, newer thio-LISICON materials with a general composition of $Li_{10}(M_{1-x}N_x)P_2S_{12}$ (M, N=Ge, Si, Sn) exhibit conductivities nearing 10 mS/cm and can be further enhanced through doping, such as with Cl (Kato et al., 2016). On the other hand, inorganic glass electrolytes are typically mixtures of amorphous compounds, such as $Li_3PO_4^-Li_2S^-SiS_2$ (Tatsumisago, Mizuno, & Hayashi, 2006) and $Li_2S^-P_2S_5$ (Trevey, Jang, Jung, Stoldt, & Lee, 2009). In terms of room temperature conductivity, Li_3PO_4, and Li_2S only achieve 10^{-9}S/cm (S. Zhang, Xie, & Chen, 2005) and

10^{-13}S/cm (Bischoff, Schuller, Dunlap, & Martin, 2014), respectively, whereas the composite glasses mentioned earlier have conductivities of 1.5×10^{-6} S/cm and 8×10^{-8} S/cm, respectively (Bischoff et al., 2014).

Organic polymers and inorganic ceramics exhibit distinct chemical and mechanical properties, influencing the design of batteries. Organic electrolytes, characterized by their soft nature and outstanding electrochemical performance (Dias, Plomp, & Veldhuis, 2000), are suitable for flexible battery configurations. Nevertheless, they encounter challenges including low Li^+ conductivity (<10^{-5} S/cm at room temperature), significant ionic transfer resistance, and susceptibility to oxidation at high voltages (Kerman, Luntz, Viswanathan, Chiang, & Chen, 2017) (F. Strauss et al., 2018). Consequently, ceramic/polymer shows more promising properties that could offer a solution to the consistent improvement of ionic conductivity and interfacial contact. This approach leverages the strengths of both organic and inorganic electrolytes, merging them into a promising hybrid system. Despite extensive research efforts, the ionic conductivity and mechanical strength of solid polymeric electrolytes (SPEs) still require improvement, posing a significant challenge to their widespread adoption in various applications (R. Chen, Qu, Guo, Li, & Wu, 2016).

In order to improve the polymer electrolyte performance, several techniques were applied. Copolymerization, crosslinking, blending, and interpenetration are commonly used as polymer/polymer coordination techniques. However, these methods do not significantly improve the mechanical properties of the electrolyte. In contrast, composite polymer electrolytes incorporate a range of materials into polymers, including inert ceramic fillers (Agrawal & Pandey, 2008), fast-ion conductive ceramics (Aliahmad, Shrestha, Varahramyan, & Agarwal, 2016), lithium salts (Do, Chang, & Lee, 1996), and ionic liquids (Subianto, Mistry, Choudhury, Dutta, & Knott, 2009). The synergistic effect between the polymer and inorganic filler in composite polymer electrolytes leads to substantial improvements in room temperature conductivity, mechanical strength, and interface stability with the electrode. Overall, these approaches aim to optimize the properties of polymer electrolytes, enhancing their performance in various applications.

This thesis mainly focuses on polymeric electrolytes, specifically PVDF-copolymer with an enhancement with ionic liquids and nanocomposites, which are described in the following sections.

2.2 Material Characterization

2.2.1 Poli(vinylidene fluoride)(PVDF)

Poly(vinylidene fluoride)(PVDF) combines the characteristics of fluororesin and general-purpose resin. The polymer chain has alternating CH_2 and CF_2 groups as a repeating unit. Its structure is shown in Figure 2 (Saxena & Shukla, 2021). PVDF is a non-reactive thermoplastic fluoropolymer that yields from the polymerization of vinylidene difluoride. The structure of PVDF shows good thermal stability, high mechanical strength, high chemical resistance, electrical insulator, and dielectric properties. These characteristics are necessary for a good separator or solid electrolytes. Its molecular chain is closely arranged and there are strong bonds between the molecular chains (Boddula, Pothu, Asiri, et al., 2020).

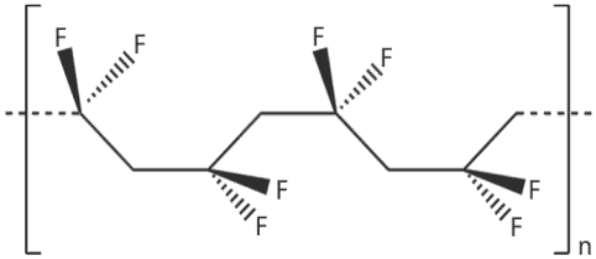

Figure 2: Schematic representation of the chain of PVDF.

PVDF has a semi-crystalline structure, translating into an amorphous structure. The fluoropolymer exhibits four different conformations named α, β, γ and δ-phases. PVDF can also be named poly(1,1-difluoroethylene) with (CH_2-CF_2) as a recurrent unit along the polymer chain. The C–F bonds present in the PVDF structure are polar. The highest dipole moment is obtained with the alignment of all dipoles of the polymer in the same direction (Saxena & Shukla, 2021). Usually, the bulk PVDF exhibits a mixture of β, α, and γ-phases and typically indicates semi-crystalline characteristics produced by melts or solutions. The α-phase out of the three is the one that is thermal stable with aligned polymer chains anti-parallel to each other (Dallaev et al., 2022). Furthermore, these individual dipoles' directions are randomly distributed at room temperature, resulting in a net-zero dipole moment for the entire system. PVDF with predominant β-phases has the best piezoelectric, ferroelectric, and pyroelectric properties. This phenomenon is due to the all-trans zig-zag conformation that translates to the highest dipole moment. The γ-phase' dipole moment is considerably lower than the β-phase, but also reveals certain piezo- and pyro-electric properties (Dallaev et al., 2022). In order to maximize energy harvesting, the randomly oriented dipoles in natural PVDF must be aligned, meaning that, the proportion of β-phase must be raised (J. Yang, Yao, & Meng, 2022). Accordingly,

β-phase is the desired phase for the piezoelectric characteristics of the polymer.

2.2.2 Poli(vinylidene fluoride co-hexafluoropropylene) (PVDF-HFP)

Recently, the copolymer of PVDF, hexafluoropropylene (PVDF-HFP), has attracted great attention as a desirable membrane material. The polymer chain has alternating CH_2 and CF_2 groups as a repeating unit, just like PVDF, and a second unit of CF_2 and CF_3. Its structure is shown in Figure3.

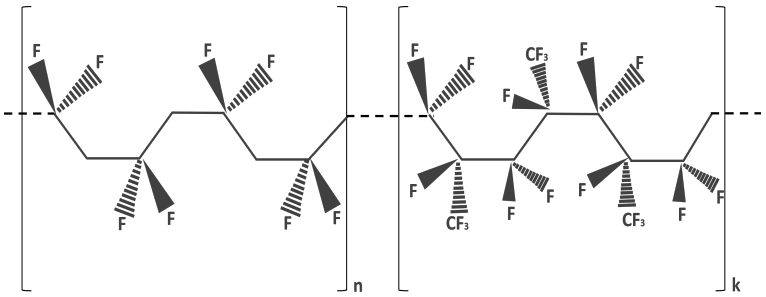

Figure 3: Schematic representation of the chain of PVDF-HFP

Poly(vinylidene fluoride-co-hexafluoropropylene) (PVDF-HFP) is a hydrophobic crystalline copolymer with excellent properties such as good thermal stability, high polarity, ionic conductivity, and good solvent resistance. Owing to its high polarity, wettability by organic solvents, and relatively high ionic conductivity, PVDF-HFP is widely used as a polymer matrix to prepare gel polymer electrolytes for energy storage applications. For example, it can enhance the performance of flexible solid-state supercapacitors. Compared with polyvinylidene fluoride (PVDF), PVDF-HFP has better properties, such as higher solubility, higher hydrophobicity (X. Wang, Xiao, Liu, Huang, & Fu, 2018), and better mechanical strength, owing to the combination of HFP (J. Yang et al., 2022). Compared with PVDF, the incorporation of HFP groups gives PVDF-HFP better properties, such as higher solubility, lower crystallinity, greater free volume, and better mechanical strength. Moreover, the incorporation of HFP groups enhances the fluorine content, which results in the higher hydrophobicity of PVDF-HFP (X. Wang et al., 2018). PVDF-HFP polymer is crystalline in nature and has chemical stability and HFP is amorphous in nature. The crystalline nature of PVDF and the amorphous nature of HFP may give mechanical stability in ionic conductivity. Moreover, strong electrons with functional groups (-C-F) in PVDF-HFP make the polymer highly anodically stable.

The choice of PVDF-HFP for this thesis relies upon its promising properties. Among the various polymers, PVDF-HFP stands out as a highly propitious polymer host due to its outstanding characteristics, including partial crystalline structure, extended electrochemical stability, and exceptional resistance to heat and mechanical stress. Furthermore, its notably low glass transition temperature (Tg = −62 °C) and high dielectric constant (ϵ = 8.4) facilitate increased dissociation of lithium ions, allowing multiple mobile ions to engage in the conduction process (Jayanthi & Sundaresan, 2015). The HFP unit in the PVDF-HFP compound plays a crucial role, because of is amorphous in nature, which means it lacks a well-defined, ordered structure. This amorphous character allows it

to accommodate various ions and molecules, making it essential for the complexation of different lithium salts in electrolytes, leading to enhanced ionic conductivity, that ranges from $10^{-7} - 10^{-4}$ S/cm (Stephan, Kumar, Renganathan, & Kulandainathan, 2005). Consequently, the presence of the HFP unit helps facilitate the movement of lithium ions, contributing to improved ionic conductivity in PVDF-HFP-based materials.

2.2.3 Ionic Liquid (IL)

Ionic liquids, often referred to as ILs, are substances composed entirely of ions and possess a melting point that falls within the range of 100 to 150 °C (Hayes, Warr, & Atkin, 2015). The excellent thermal, chemical, and electrochemical stability of ionic liquids (ILs) enables their utilization as reaction mediums in scenarios like aluminum plating, where traditional aqueous electrolytes and many organic solvents are not feasible.

The molecular arrangement of ionic liquids (ILs) is influenced by various intermolecular forces, including van der Waals forces, Coulombic interactions, dipole forces, and hydrogen bonding. IL molecules exhibit both polar and nonpolar regions (Hayes et al., 2015). For instance, the anion and positively charged atoms in the cation, like the nitrogen (N) in the imidazolium ring, possess polar characteristics, while the alkyl chains in the cation are nonpolar. When ILs transition into a solid state, they can organize into a crystalline structure where the polar and nonpolar segments segregate, forming a bilayer configuration (Hayes et al., 2015).

Piperidine-based ILs are typically composed of a piperidine cation and various anions. The specific choice of anion can significantly influence their properties. Typical anions are chloride, bromide, acetate, diethylphosphate, triflate, dicyanamide, tetrafluoroborate, hexafluorophosphate, and the very important bis(trifluoromethylsulfonyl)imide (i.e. bistriflimide) ion. Piperidinium ionic liquids attract considerable interest due to their superior performance in terms of high ionic conductivity, wide electrochemical window, low volatility, and low flammability. One of the most important applications of piperidinium ionic liquids is its application in electrolyte systems. The high thermal stability of ionic liquids increases the safety of applications in rechargeable lithium-ion batteries and other electrochemical devices (Baranchugov, Markevich, Pollak, Salitra, & Aurbach, 2007) (Salminen et al., 2007). From the literature, it was shown that the inclusion of 1-Methyl-1-propylpiperidinium bis(fluorosulfonyl)imide inhibits the formation of water clusters by utilizing the hydrophobic $PP13^{+}$ cations and lithium-attractive FSI^{-} anions, resulting in a significantly expanded electrochemical stability range of up to 4.9 V (C. Zhang et al., 2022).

For this work a piperidine-based IL was selected, 1-Methyl-1-propylpiperidinium bis(fluorosulfonyl)imide is a compound with the chemical formula $C_9H_{20}F_2N_2O_4S_2$. The compound consists of a piperidinium cation with a methyl and propyl substituent and a bis(fluorosulfonyl)imide anion. The molecular structure is represented in Figure 4.

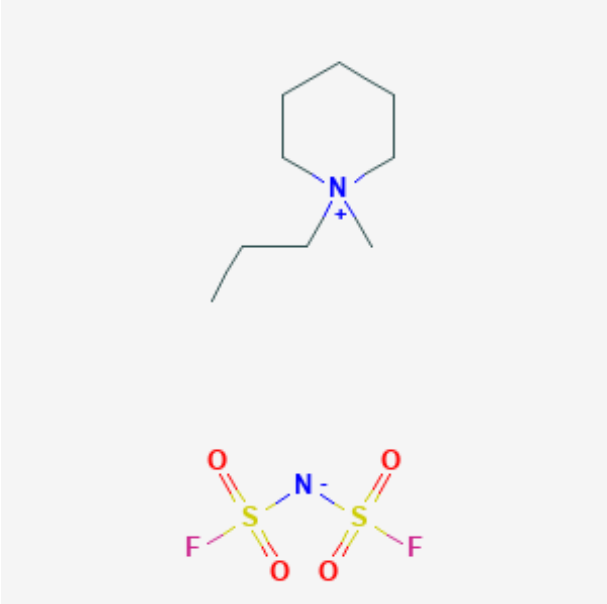

Figure 4: Schematic representation of the chain of IL

2.2.4 Piezoelectric ceramics

Barium Tinate Oxide (BTO)

Barium titanate (BTO) is an inorganic compound with the chemical formula $BaTiO_3$. It exhibits various important properties, making it a valuable material in different applications. The foremost properties are its high dielectric constant (Randall, Newnham, & Cross, 2004), which was caused by its ferroelectric characteristics (Buscaglia, Buscaglia, & Canu, 2021), it detains a good piezoelectric coefficient and favorable electromechanical coupling coefficient (Gao, Xue, Liu, Zhou, & Ren, 2017).

BTO exhibits different crystallite variants depending on the temperature and composition. The most notable structural phase is the cubic phase, which prescribes a cubic perovskite structure at high temperatures (above the Curie temperature, typically around 120°C). In this phase, the BTO crystals have a cubic symmetry. Below the Curie temperature, BTO undergoes a phase transition and becomes tetragonal. This phase is characterized by elongation along one crystallographic axis, resulting in a tetragonal crystal structure. This phase change is associated with the ferroelectric properties of BTO. At even lower temperatures, BTO can transition into an orthorhombic phase. In this phase, the crystal structure becomes more complex, with three unequal axes. Under specific conditions, BTO can also exhibit a rhombohedral crystal structure, which is a distorted cubic structure (Rached et al., 2021). At temperatures below 1460 °C, BTO shows a perovskite structure. In tetragonal BTO, there exist two types of domain boundaries that divide areas with polarization orientations: one type features antiparallel polarization (180° walls), while the other exhibits perpendicular polarization (90° walls). The domains are related to the structure stabilization and the process of changing the direction of polarization and the presence

of the ferroelectric hysteresis loop (Buscaglia et al., 2021).

From the literature, incorporating BTO into PVDF film has notably enhanced its mechanical durability. The stress levels achieved for PVDF films containing 5% BTO were substantially greater, with a 17% increase, compared to pure PVDF films (Ram et al., 2020). In another study, BaTiO3 (BTO) nanowires (NWs) at varying concentrations were introduced into PVDF to adjust the polar phase content, internal resistance, and optimize power generation. The increased values of the dielectric constant and dielectric loss in BTO-PVDF samples at lower frequencies indicate a substantial interfacial polarization within the composite system. Resulting in an elevated power output in the BTO (15 wt%)-PVDF composite (Hazra et al., 2022). The addition of BTO in polymeric matrixes also denoted an increase of the β-phase crystallinity and its piezoelectricity (Hu et al., 2019).

Barium Strontium Tinate (BST)

BST has a perovskite structure represented as ABO_3. Within this structure, barium and strontium are located at the A-sites, which correspond to the corners of the lattice, while titanium resides at the B-site, located at the center. Oxygen atoms occupy the face-center sites. Barium and strontium can smoothly replace each other within the lattice, forming a continuous solid solution (Knauss et al., 1996). Under normal room temperature conditions, the lattice structure of BST is cubic. However, when the material is cooled or the concentration of barium is increased, it undergoes a transition to a tetragonal phase. The cubic phase is characterized as paraelectric, meaning it lacks spontaneous electric polarization. In the tetragonal phase, the central titanium atom can shift, resulting in the development of ferroelectric properties (Knauss et al., 1996).

Several studies were conducted on how BST ceramics can improve the performance of polymeric films. PVDF films that were doped with BST, demonstrated a 3-4 times higher dielectric constant and flexoelectric response (Hu, Zhou, Liu, & Chu, 2018). Another study showed that the polarization field near the surfaces of BTO improved the electrocaloric effect of the samples (Jiang, Zheng, & Zheng, 2015).

Lead Zirconate Titanate (PZT)

The PZT piezoelectric ceramic, demonstrates exceptional characteristics, including a notably high dielectric constant and a strong piezoelectric coupling coefficient. It is widely acknowledged as an advanced smart material (Chaipanich, 2007). PZT exhibits a perovskite arrangement, characterized by the general formula ABO_3. In this structure, "A" represents a divalent cation like Pb^{2+} located at the corners of the cubic unit cell, "B" signifies a tetravalent cation such as Zr^{4+} or Ti^{4+} occupying the body-centered position within the unit cell, and "O" denotes oxygen atoms found at the face-centered positions of the cubic lattice. (Bhalla, Guo, & Alberta, 2002) The morphotropic phase boundary (MPB) acts as a dividing line within the ferroelectric phase, separating it into two segments: one characterized by a tetragonal phase, which is prevalent in the Ti-rich area, and another with a rhombohedral phase, primarily found in the Zr-rich region (Bhalla et al., 2002).

From the literature, PVDF-doped films with PZT were assembled into half cells (Li/PVDF-PZT CPE/Li) and had a stable performance for 500 cycles with a C-rate of 0.5C at room temperature (B.-H. Kang, Li, Yang, Li, & Huang, 2023). Another study demonstrated that PVDF-doped films showed maximum polarization and a high coercive field. Confirming that 4 mole% PZT doped PVDF composites can be used in high electric field applications (Pradhan et al., 2017).

In this particular section of the master's thesis, there is no mention in the literature related to the ionic liquid and PZT ceramic materials blend, incorporated in solid-state electrolytes.

2.3 State of the art - Modeling Work

Modeling lithium-ion batteries is a crucial area of research in various fields, including materials science, electrochemistry, and energy storage. Such research helps improve battery performance, lifespan, safety, and efficiency. There has been exhaustive research on this topic, which culminated in three different types of battery modeling methods: Electrochemical model, Equivalent circuit model, and Data-driven model. In this work, the first type of model will be discussed.

2.3.1 Modelling approaches for Lithium-Ion Batteries - recent work

The electrochemical model is grounded in the essential chemical principles within the battery and is composed of a set of partial differential equations accompanied by boundary conditions. These equations enable the accurate simulation of intricate reactions taking place within the battery, offering a high level of precision. In the literature, there are various mathematical models used to describe the behavior of solid-state electrolytes in the context of batteries and energy storage systems.

It was demonstrated by a 1-D geometry model (Becker-Steinberger, Funken, Landstorfer, & Urban, 2010) that takes into account detailed aspects of ion transport in solid solutions of crystalline metal oxides. The paper describes the transient lithium ion flux through a solid electrolyte, the solid-solid interfaces, and an intercalation electrode. The chemical domain, namely the diffusion and electromigration processes, were modeled through the transport equations (J_{Li^+}) and ($\frac{\partial C_{Li+}}{\partial t}$). The model provides a reasonable framework for understanding the discharge behavior of lithium-ion batteries.

A different approach, based on a simulation for thin-film solid-state batteries (Kazemi et al., 2019) overcomes the limitation of existing models by incorporating a new definition of the diffusion coefficient based on experimental measurements. It proposes a new formulation for the diffusion coefficient that is concentration-dependent, based on experimental data ($D_{Li}(c_{LiCoO_2}(y,t))$). The simulations accurately fit the experimental data at low and high discharge currents up to 5 mA cm$^{-}2$.

Furthermore, the modeling and simulation of a 2D lithium-ion solid-state battery (Bates et al., 2015) was studied. The simulations consider various parameters such as electrochemical reactions, heat transfer, and the diffusion of lithium ions and electrons. The simulations were carried out in COMSOL Multiphysics version 4.3 using three modules including Tertiary Current Distribution, Transport of Diluted Species, and Heat Transfer in Solids. The 2D model is used to simulate the battery's discharge curves, heat flux, and the concentration of lithium ions, electrons, and solid lithium at any given time in the discharge cycle. This study provides valuable insights into the behavior and performance of lithium-ion solid-state batteries and offers guidance for future design improvements.

2.3.2 Modelling using Partial Differential Equations - Physics-based models

Physics-based models utilize interconnected partial differential equations (PDEs) to depict electrochemical and chemical processes. These models offer insights into the intricate workings of electrochemical cells across various scales, as visualized in Figure 5 (He, Pecht, Flynn, & Dinmohammadi, 2018). They often incorporate the flow of lithium ions between the solid and electrolyte phases, coupled with maintaining charge and mass conservation in both phases. Achieving an accurate representation of a cell's performance necessitates the spatial and temporal discretisation of these physics-based models. Various methods for spatial discretisation, including finite element, finite difference, and finite volume techniques, are employed to solve the PDEs efficiently (He et al., 2018).

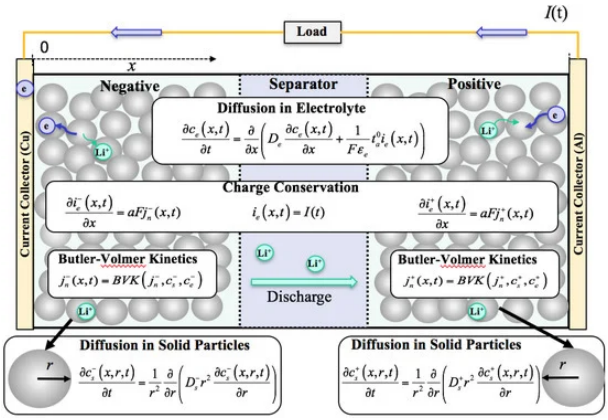

Figure 5: Doyle Fuller Newman model of Lithium-Ion batteries. Dual foil battery - electrochemical model.

The diffusion partial differential equation (PDE) in solid particles is a crucial component of a comprehensive electrochemical model. It provides essential information about the available lithium and the lithium concentration within the electrodes. Solid-phase diffusion PDEs involve more equations of state than the electrolyte-phase diffusion PDEs. This increased complexity is because solid-phase diffusion varies along both the electrode's thickness at the macro-scale and the particle's radius at the micro-scale (He et al., 2018). Due to the higher computational demands of solving solid-phase diffusion PDEs compared to other PDEs in the electrochemical model, simplifications are necessary to enable real-time simulations.

The Single Particle Model (SPM) is widely employed in electrochemical battery simulations due to its reduced complexity when compared to other electrochemical models. In Figure 6 (N. T. Tran, Vilathgamuwa, Farrell, et al., 2016), you can observe the geometry of the SPM model. Although this geometry bears similarity to the Doyle Fuller Newman (DFN) model, there's a key distinction: SPM features only one particle in each electrode, as opposed to DFN. The SPM was initially introduced and used in the modeling of Li-ion batteries. It simplifies both the negative and positive electrodes as two spherical particles and doesn't consider the concentration of Li^+ in the electrolyte phase. This approach offers reasonable accuracy, particularly at low current rates, while being computationally efficient. However, because it doesn't account for the distribution of lithium in the electrolyte phase, the SPM is best suited for low-current applications (Chakraborty et al., 2018).

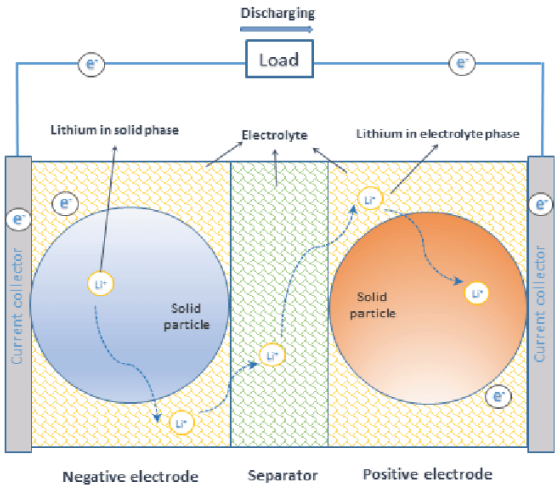

Figure 6: Single particle model (SPM). Representation of a Lithium-Ion battery

The Single Particle Model with Electrolyte (SPMe) enhances the accuracy of the SPM at high current rates by considering the impact of electrolyte phase potential on cell voltage (Chakraborty et al., 2018). In various operational scenarios, as evidenced, SPMe can demonstrate remarkable agreement with the Doyle-Fuller-Newman (DFN) model, making them valuable in numerous real-world applications (Marquis, Sulzer, Timms, Please, & Chapman, 2019). For battery state estimation, SPMe is preferred due to its superior predictive accuracy (Moura, Argomedo, Klein, Mirtabatabaei, & Krstic, 2016).

Chapter 3

Experimental Methodology

This chapter is divided into two sections. The first describes the materials and procedures used to synthesize the SSE samples, which is followed by a section that portrays the experimental techniques used to characterize the polymeric films. Firstly the polymeric SSEs were produced by a dry-casting technique. Hence, the polymeric electrolyte characterization was necessary. According to the different targets of study, morphological, electrochemical, and physical-chemical processes, different preparations of the samples were required.

Experimental Methodology

3.1 Primary Materials

To synthesize the SSE a vast compound selection was necessary. The composites selected were as follows: PVDF-HFP ($C_5H_2F_8$); DMF (C_3H_7NO); BTO ($BaTiO_3$); BST (BaO_4SrTi); PZT ($Pb[Zr_xTi_{1-x}]O_3$) and IL(1-Methyl-1-propylpiperidinium bis(fluorosulfonyl)imide) ($C_9H_20F_6N_2O_4S_2$), which can be classified as fluorinated polymer, solvent, ferroelectric inorganic compounds, and organic salt, respectively. Tables 3.1 to 3.3 (for Biotechnology Information, 2023a) (for Biotechnology Information, 2023e) (for Biotechnology Information, 2023c) (for Biotechnology Information, 2023b) (for Biotechnology Information, 2023d) summarize the relevant information regarding the materials' physical and chemical properties.

Table 3.1: Main physical and chemical properties of the materials used.

Compound	Density (g/mL) at 25°C	Molecular weight (g/mol)	Flash point (°F)	Properties
PVDF-HFP	1.77	214.06	NA (gas)	This thermoplastic polymer displays an elevated melting point and remarkable resistance to chemicals. It finds extensive utility in the fabrication of membranes.
DMF	0.95	73.09	136	DMF is a formamide derivative where the amino hydrogens of formamide are substituted with methyl groups. It functions as a polar aprotic solvent and exhibits hepatotoxic properties. This compound is categorized as a volatile organic compound (VOC).

Table 3.2: Main physical and chemical properties of the ceramics used.

Compound	Density (g/cm^3)	Molecular weight (g/mol)	Boiling point °C	Cristal structure	Properties
BTO	7.75/8.0	233.19	1640	Tetragonal	BTO is an inorganic substance and has interesting ferroelectric properties. This substance is a white powder. Its main employment is in the preparation of electronic ceramics.
PZT	7.75-8.0	426	170-360	Cubic	PZT is a ceramic perovskite substance that exhibits a significant piezoelectric effect. This material can undergo shape changes when subjected to an electric field.
BST	4.91	336.81	2060	Cubic	BST categorized as a ferroelectric material, possesses the standard traits intrinsic to ferroelectrics. The performance of BST is notably influenced by adjustments in the Ba/Sr ratio.

Table 3.3: Main physical and chemical properties of the ionic liquid (IL)

Compound	Molecular weight (g/mol)	Melting point (°C)	Conductivity mS/cm at 20°C	Properties
IL	322.4	7.95	13	The IL has great interest due to its low volatility, high thermal stability, and tunable properties, making them versatile in diverse fields.

3.1.1 SSE sample preparation

The procedure for the SSE synthesis is organized according to the following main steps: dissolution or dispersion, mechanical stirring, coating, and drying steps. This technique is called the solution casting method. Figure 1 shows a schematic representation of the synthesis process for the solid polymer electrolytes.

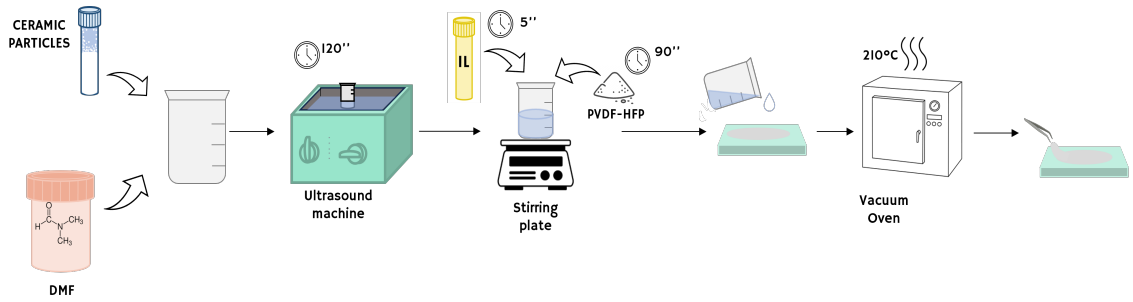

Figure 1: Schematic representation of the synthesis process for the solid polymeric electrolytes - a graphic description of the solution casting technique. Synthesis path that originates in a polymeric matrix enriched with ceramic and ionic liquid.

The procedure that was used to attain the polymeric electrolytes is named the solution casting technique. The casting solution is prepared with DMF (N,N-Dimethylformamide 99.8%) as the solvent, whilst the solid phase is composed of PVDF-HFP and ceramics (either BTO, BST, or PZT), and the addition of a liquid phase, the IL.

In order to obtain the different SSE samples the following steps were prescribed:

- Preparation of the casting solution by adding the ceramic particles powder (BTO, BST, PZT) to the DMF. 16wt% of ceramics was dispersed in 6mL of DMF in a glass vial.
- The solution was kept in the ultrasound bath for around 2 hours until the ceramic particles were completely dispersed and deagglomerated.
- Addition, dropwise, 40wt% of Ionic liquid (IL) - 1-Methyl-1-pentylpyrrolidinium bis(trifluoromethanesulfonyl)imide 99.9%. Followed by 5 minutes of stirring so that the IL is well incorporated into the solution.
- Addition of the PVDF-HFP in the solution. In this case, according to the film ratio of PVDF-HFP:DMF=15:85, 1g of PVDF-HFP was dissolved in the previous solution.
- Stir the solution with the aid of a mechanical stirrer (IKA^{TM} Magnetic Hot Plate Stirrer) at a stirring speed of 110 rpm, at room temperature until the PVDF-HFP is fully dissolved.
- The mixed solution (casting solution) was poured onto a flat glass substrate and thinly spread to attain the desired thickness of 50 μm. The spread solution was dried in the oven at 210°C for around 10 minutes. The drying time may vary, as the main goal is the complete removal of DMF.
- The resulting cast layer can be stripped from the carrier substrate (glass) and properly stored, so that after is prone to the characterization techniques and tests.

The end products resulting from the synthesis process above are PVDF-HFP IL BTO, PVDF-HFP IL BST, and PVDF-HFP IL PZT. To attain the remaining end products (reference sample and samples with ceramics or IL) similar steps needed to be pursued. For the synthesis of the PVDF-HFP sample, there was no addition of the ceramics nor of the IL. As for the synthesis of the samples PVDF-HFP IL, PVDF-HFP with ceramic fillers (PVDF-HFP BTO, PVDF-HFP BST, and PVDF-HFP PZT), either the addition of the ceramics was excluded either the of the incorporation of IL was kept out, respectively.

For the polymeric matrix mixture, a ratio of 85:15 (solvent and polymer, respectively) was considered. More details can be found in Table 3.4, where the SSE components used are listed and the main parameters involved, while Table 3.5 describes the parameters employed.

Table 3.4: SSE Components and synthesis parameters.

Solvent	Liquid phase	Solid phase
DMF	IL	Ceramics and PVDF-HFP
85wt%	40wt%	16wt% and 15wt%

Table 3.5: SSE Synthesis parameters.

Synthesis Temperature (°C)	Stirring speed (rpm)	Drying Temperature (°C)
Room Temperature (20°C)	110 rpm (1 hour)	210°C (10 minutes)

3.1.2 Cell assembly

In order to evaluate the electrochemical behavior, and to find the performance and behavior of the produced material, coin cells were fabricated. For this purpose, the electrolyte materials were assembled into battery test cells and the electrochemical performance was characterized. An illustrative scheme of the built-in process can be found in Figure2.

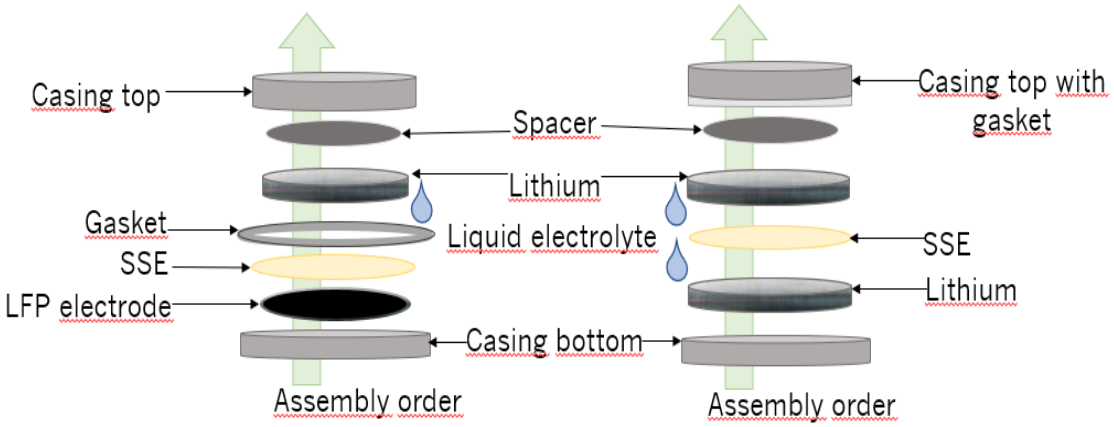

Figure 2: Schematic representation of the cell assembly. The 2016 cell is represented on the left side and on the right side is a 2032 coin cell.

In the scheme is possible to identify both cells used in this project, the 2016 half-cell is built with a positive electrode (LFP) and a negative electrode (Li-metal), and on the right side, is represented by a 2032 symmetrical cell, where both working electrodes are Li-metal. The assembly was carried out manually inside a controlled atmosphere - inside a glove box. The symmetrical cells are exclusively used for electrochemical impedance spectroscopy testing because it allows a focus on the behavior of the material itself rather than the interactions with different materials.

3.2 Testing and Characterization Techniques

The adopted techniques necessary to characterize not only the SSE but also the raw materials required for the SSE were: Scanning electron microscopy (SEM), Fourier transformed infrared spectroscopy (FTIR) with attenuated total reflectance (ATR) accessory, Thermogravimetric analysis (TGA), Differential scanning calorimetry (DSC), X-Ray diffraction (XRD), Electrochemical Impedance Spectroscopy (EIS) (including Chronoamperometry (CA)), and Galvanostatic Charge-Discharge.

3.2.1 Scanning electron microscopy (SEM)

Electron microscopy is employed to examine the structure of materials. Specifically, a significant type of electron microscope known as the scanning electron microscope (SEM) plays a crucial role in producing images of materials using a concentrated electron beam with a range of 0.4 to 5 nm. During this process, electrons interact with the atoms within the material being studied, leading to various scattering phenomena, including elastic and inelastic scattering for secondary electrons, as well as radiation emission. These interactions yield valuable insights into both the morphology and composition of the material under investigation.

The surface morphology and shape of the SSE were evaluated, and the samples were analyzed with JEOL JSM-7500FA analytical high-resolution scanning electron microscope (HR-SEM), with the only needed preparation being their placement onto a conductive stage.The samples did not contain Ionic liquid, as they were not made out of a conductive material, so they required a thin layer of 15nm Au/Pd, to be seen in the SEM microscope. This layer was deposited, through sputtering, using a sputtering machine (Emitech K350 sputtering head). Samples were measured as dried products and different regions were analyzed to ensure a representative image.

The microscope was fitted with Energy Dispersive analysis of X-rays (EDS Analysis), Oxford Instrument (LINK ISIS) to detect the overall chemical composition of the solid polymer electrolyte membrane. The characteristic X-rays are emitted by the inner electron shells of atoms when the high-energy electrons knock out inner shell electrons. The energy of these X-rays is specific to the elements from which they originate. Each element emits X-rays at unique energy levels, making it possible to identify and quantify the elements present in the sample. To prepare the samples for observation, the SSE films were attached to an aluminum holder using conductive tape and then coated with a thin layer of gold.

3.2.2 Fourier transformed infrared spectroscopy (FTIR-ATR)

The energy of the molecular vibration is quantized and the differences between the energy levels are of the same magnitude as a photon with a wavenumber in the infrared range(Siebert & Hildebrandt, 2008). This match in energy means that infrared light can induce vibration transitions between different energy levels. In other words, when a sample is illuminated with infrared light of different wavenumbers, light with the same energy as the difference between the vibration levels of the sample molecules is absorbed. A plot that records the absorbance or transmittance of the light as a function of the wavenumber of the light is called an infrared (IR) spectrum (Țucureanu, Matei, & Avram, 2016). On an IR spectrum, each absorption peak or band corresponds to a vibration of the bonds.

FTIR spectroscopy is commonly employed for examining molecular interactions because its spectra provide insights into molecular vibrations. Interactions between molecules can alter the strength of the bonds involved, leading to

shifts in vibration frequency and potential reductions in vibration intensity (Mizuno et al., 2000).

The FTIR spectra of the SSE were recorded using a PerkinElmer FTIR with ATR. FTIR spectra were obtained in the range of wavenumber from 4000 to 600 cm^{-1}, with 4 cm^{-1} resolution and 8 scans of data accumulation. The FTIR spectra were normalized and major vibration bands were associated with chemical groups.

3.2.3 X-Ray diffraction (XRD)

With the purpose of analyzing the crystalline structure of the studied samples XRD technique was used. The equipment used was PANalytical X'Pert Powder XRD (alpha-1) with automatic data acquisition (X' Pert Data Collector (v2.0b) software), using Cu Kα radiation (λ = 0.15406 nm) working at 45 kV/40 mA. The equipment was operated under ambient temperature, and the scan range was between 10° and 90°, with a scan rate of 20 °C/min. It was performed on all SSE samples. The crystallinity for each sample was obtained from the ratio between the area under the crystalline peaks and the total area under the diffraction curve. The separation of crystalline peaks from the amorphous halo was made by fitting a curve in the OriginPro®2023b software, where is possible to determine the full width at half minimum (FWHM). Therefore, the degree of crystallinity is an experimental error associated. The crystallite size can be calculated using Equation (3.1) the Scherrer Equation:

$$D = \frac{K\lambda}{\beta cos\theta} \Leftrightarrow D = \frac{0.94 \times 0.15406}{\beta cos\theta} \tag{3.1}$$

Where D is the average crystallite size (nm), K is the Scherrer constant (0.94 in this work), λ is the wavelength of the incident radiation (1.5406 $\ddot{A}$), λ is the full width at half maximum (radians) of the diffraction peak and β is the Bragg's angle (radians) that is also known as the line broadening at FWHM.

3.2.4 Differential scanning calorimetry (DSC)

In the realm of materials science, it is observed that materials have the ability to undergo transitions between the gaseous, liquid, and solid states in response to changes in temperature. Particularly, when a material undergoes a transition from the liquid to the solid state, there is a notable alteration in the arrangement of its constituent molecules or atoms. This rearrangement occurs as the kinetic motion of the molecules or atoms is gradually reduced and slowed down due to cooling.

During the liquid-to-solid transition, this rearrangement process can result in the creation of a crystalline lattice structure. Such a crystal lattice exhibits a remarkable degree of long-range order, spanning nanometer scales, equivalent to the dimensions of several atoms. Alternatively, the transition from a liquid to a solid can also yield a glassy state, characterized by the absence of long-range order. This transition, which leads to the formation of a glass, is referred to as the "glass transition." In the context of polymer science, it's important to note that the

term "glass transition" can also denote the transition between the glassy state and the rubbery state of a polymer material(S. Singh, Bononi, Andreussi, Karmodak, et al., 2023).

DSC is a thermo-analytical method used to quantify the heat released or absorbed during phase transitions. In DSC experiments, both a sample and a reference material undergo simultaneous heating or cooling while being kept at a constant temperature. The DSC technique involves measuring the variation in the heat needed to sustain an equivalent temperature for both the sample and reference material as a function of temperature. DSC measurements for all the SSE samples were performed using a DSC Q200 V24.4 Calorimeter, with the following parameters, a heating rate of 10 °C/min in a controlled atmosphere with a flow rate of 20 ml/min, with temperature ranges from 20 to 200 °C.

3.2.5 Thermal gravimetric analysis (TGA)

Thermogravimetric analysis (TGA) offers insights into physicochemical transformations leading to sample weight reduction, encompassing processes like desorption, decomposition, oxidation, and dehydration. TGA serves as a valuable tool for assessing the kinetics of thermal decomposition and the vapor pressure characteristics of substances within diverse environments, including ambient conditions, vacuum, inert gases (e.g. N_2), and oxidizing gases (e.g. N_2). When combined with mass spectrometry, TGA becomes a powerful instrument for investigating the intricate mechanisms underlying the decomposition of materials at a molecular level(Colomines, Decaen, Lourdin, & Leroy, 2016).

Thermal behavior and storage stability of the polymeric membranes were studied using TA Instruments TGA Q500. Small amounts of the SSE (2-5g) were heated under a controlled nitrogen atmosphere with a flow rate of 60 ml/min, at a temperature increase rate of 20 °C/min, in the range of 30-800 °C. TGA provided information on the temperature at which the polymeric SSE membranes begin to decompose, including the different weight loss profiles corresponding to the different components within the samples. This is critical for understanding the operational temperature range of the synthesized materials.

3.2.6 Electrochemical Impedance Spectroscopy (EIS)

Electrochemical Impedance Spectroscopy (EIS) is a scientific method used to non-destructively analyze and characterize electrochemical materials and devices, yet the association with a thermal process may have a destructive effect and compromise the samples' integrity. In a solid-state ion battery, lithium ions penetrate the solid electrolyte (ionic conduction) and intercalate into the electrodes. In the electrodes, the gain or loss of electrons occurs (charge transfer), and at the electrode/electrolyte interface, ions can accumulate and form a double layer. The different elements present in a battery can be characterized by electrochemical methods. The process is as follows, applying a small alternating potential (ΔV) with varying frequency to the electrochemical

system and collecting the electrical response (ΔI). The ratio of (ΔV) and (ΔI) gives impedance (Z) as:

$$Z = \frac{\Delta V}{\Delta I} \tag{3.2}$$

Note that Z contains all the electrical parameters of the components in an electrochemical system (Z'andZ''). Z' is the real part of the impedance representing the conductive contribution, and Z'' is the imaginary part representing the capacitive contribution or capacity-like behavior. The EIS measurement can be modeled with an equivalent circuit, and the results are demonstrated in a Nyquist plot, where, the y-axis represents the real part and the x-axis represents the real part.

The impedance measurements were performed with the Autolab PGSTAT302N equipped with an FRA2 module and for the temperature input, a G-cell oven was used. EIS measures impedance, spanning a vast frequency range, from millihertz (mHz) to gigahertz (MHz), allowing it to investigate various electrochemical systems' interfacial properties and dynamic behavior(Raijmakers, Büchel, & Notten, 2018). In this work, the frequency range was between 40MHz and 100mHz. This broad frequency output range of the analyzer enables impedance spectroscopy to characterize solid electrolytes with a wide range of conductivity.

In the conductivity measurement for SSE samples, the symmetrical cell was assembled (Figure 2), the cell was electrically connected to the potentiostat, and a ΔV with varying frequencies was applied. The conductivity is obtained from the measured resistance of the electrolyte as:

$$\sigma = \frac{l}{RA_s} \tag{3.3}$$

with l the thickness of the electrolyte, R the resistance of the electrolyte, and A_s the contact area between the electrodes and electrolyte. Impedance measurements were performed on all specimens, each sample was put through a cycle comprising a set of five temperatures (20, 30, 40, 50, 60, 70 °C). A constant current of 0.01 mA was applied for 4000 seconds.

With the output data, it was possible to calculate the different ionic conductivities (σ) and activation energies (E_a), operating with the OriginPro 2023b. Each E_a was determined using the following Arrhenius equation:

$$\sigma = \sigma_0 \exp \frac{-E_a}{RT} \tag{3.4}$$

where σ is the conductivity (S/cm), σ_0 is a pre-exponential factor, T represents temperature (K), R is the gas constant (8.314J/mol.K), and E_a corresponds to the activation energy (J/mol) that comprises of Coulumbic binding energy, the undetermined parameter.

The evaluation of the lithium transfer number was studied using the Ivium Vertex Potentiosta, through chronoamperometry measurements. For each sample a symmetrical cell was assembled with two lithium metal

discs sandwiched between a SSE, that is meant to be analyzed. By using a symmetrical cell for impedance spectroscopy, the focus is on measuring the electrical properties of the material, and the chemical reactions at the electrodes are typically minimal due to the constant composition on both electrodes. The technique allows for the characterization of the material's electrical behavior over a range of frequencies without significant interference from chemical reactions. This is a technique where a constant potential is applied in the function of time, for this work it was applied a potential of 0.01V to the working electrode of the cell. A current is measured that falls from an initial value I_0 to a steady-state value I_ss reached after around 2 hours.

3.2.7 Galvanostatic charge-discharge

Galvanostatic charge-discharge is an electrochemical method in which the cell is charged under constant currents between two potential limits, and the potential is recorded vs. capacities. With the purpose of evaluating the battery capacity or the amount of energy that can be held, charge and discharge cycles were performed. This also allows an experimental visualization of the impact of the use of different SSE on the cell performance.

All cells were cycled galvanostatically on a LAND Battery Testing System - Software V7.4. The electrical power produced by a battery can be expressed as the product of its voltage and current. When a battery undergoes high-current charging or discharging processes, there is a notable increase in voltage loss. This elevated voltage loss primarily stems from factors such as internal resistance (commonly referred to as IR loss), polarization, solid-state diffusion, and phase transformation phenomena within the battery. Consequently, batteries are subjected to testing under various current conditions, often referred to as C-rates. These tests are conducted to evaluate the battery's performance and behavior under different load scenarios, ensuring its functionality and efficiency under varying operating conditions.

The C-rate of a battery is expressed as C/n, where n is the number of hours needed to fully charge or discharge the battery's nominal capacity. Bearing that in mind, the batteries were tested at different conditions. The tests were divided into two cycling programs, testing the battery's long-term stability by applying a stable C-rate - Battery Cycle Life Testing. Also, testing the battery's charge and discharge stability under different C-rates measuring its capacity - Battery Capacity Testing. The half cells were all cycled up to a maximum capacity of 170mAh/g.

In the Battery Cycle Life Testing, it was applied the first charge and discharge rate of C/15, for the first cycle - the formation cycle, and then a C/10 C-rate for one hundred cycles. The cells were charged up to 4.2V and discharged to 2.5V at room temperature initially. In the Battery Capacity Testing, several C-rates were applied, starting with a lower C-rate for the formation cycle, and then increasing this value of charge and discharge. The applied current was as follows: C/20; C/10; C/5; C/2; C/1.25; 1C and 2C.

Chapter 4

Numerical Methods

This chapter's goal is to briefly introduce different numerical methods that were the target of the study and allow a better understanding and resolution of the different models for lithium-ion batteries. This chapter is divided into three sections, firstly an introduction to the advection-diffusion equation and the methods used to solve it. Then a presentation of the different methods that can be applied in order to get to a solution, and finally a comparison of the selected methods.

Numerical methods

4.1 Advection-Diffusion equation

The Advection-Diffusion equation is a combination of the diffusion and advection equations used to describe the time evolution of physical phenomena where particles or energy are transferred in a physical system. The diffusion equation models a response to a gradient of matter, momentum, and energy if the value of the quantity of interest at a particular point in space and time is described by a continuous function u. The advection equation is the process by which particles or energy are carried by the bulk motion of the flowing system. This equation governs the motion of a conserved scalar field u as it is advected by a known velocity c (Rezzolla, 2011).

Let us define $\Omega = [0, 1]$ and $T > 0$. We seek a solution $u = u(x, t)$ of the Partial Differential Equation given by

$$\partial_t u(x,t) + c\partial_x u(x,t) - k\partial_{xx} u(x,t) = f(x,t) \text{ in } [0,T] \times \Omega \tag{4.1}$$

where $c(\geq 0)$ is the velocity, $k(\geq 0)$ is the diffusion coefficient and f considered the source term.

- when $k = 0$ and $c \neq 0$, we have the particular case of the advection equation;
- when $c = 0$ and $k \neq 0$, we have the particular case of the diffusion equation, (Rezzolla, 2011).

The advection-diffusion equation allows researchers and engineers to model how lithium ions move within the battery, considering factors like convection due to fluid flow and diffusion in the solid and liquid phases. It is an essential tool for understanding the behavior of lithium-ion batteries and optimizing their performance.

This chapter's main goal is to study the different numerical methods that are associated with these types of equations, in order to understand which method should be applied in the Li-ion battery simulations since a partial diffusion equation (Equation 5.20 Chapter 5- 0D-model) is a key component of the developed model.

4.1.1 Partial Differential equations

The Advection-Difusion equation is a Partial Differential Equation (PDE). A PDE is an equation relating the partial derivatives of some unknown multivariable function. This function can be characterized by more than one independent variable $t, x, y, ...$ The dependent variable, u, is an unknown function of these variables $u(t, x, y, ...)$. It often denotes its partial derivatives by subscripts, for instance, $\partial u/\partial t = u_t = \partial_t u$. A PDE can be written as (W. A. Strauss, 2007),

$$F(x, t, u(x,t), u_t(x,t), u_x(x,t)) = F(x, t, u, u_t, u_x) = 0, \tag{4.2}$$

in the particular case that we only have two independent variables x, t (W. A. Strauss, 2007). When PDEs describe physical phenomena, usually, the variable t refers to time and x, y, z the space dimensions. In this work, we only consider one space dimension variable x.

Concerning the resolution of a PDE, an initial condition needs to be specified, meaning that the initial values of all variables must be stated. Usually, the initial condition is described for the beginning time, $t = 0$, and for the other variable x, we state what we call boundary conditions. These are typically used to specify variable values or gradients at the boundary interval (W. A. Strauss, 2007). So, the initial condition is given by $u(x, 0) = u_0(x)$ and we shall prescribe the following type of boundary conditions.

Boundary condition

Dirichlet boundary condition

The Dirichlet boundary condition is a condition, that when imposed on an ordinary or a partial differential equation, specifies the values that a solution has to take along the boundary of the domain.

For our spatial domain $\Omega = [0, 1]$, the boundary condition takes the form of two time-dependent functions $u_1(t)$ and $u_2(t)$ $x = 0$ and $x = 1$, respectively, so we are given the following:

$$u(0, t) = u_0(t), \text{ and } u(t, 1) = u_1(t). \tag{4.3}$$

The Dirichlet boundary equation is prescribed for all schemes that arise in the next sections.

4.1.2 Finite differences method

In most cases, it is difficult or even not possible to obtain an analytic solution for PDEs so we determine an approximate solution using numerical methods. The numerical methods are chosen regarding the PDE and the intended quality of the solution.

The finite differences method is a numerical technique used to solve differential equations by approximating derivatives. It is based on the concept of discretising the domain of a differential equation into a grid and then approximating the derivatives at each grid point. The fundamental idea is to replace derivatives with the difference between function values at neighboring grid points. Besides being a fast and easy-to-code method, some disadvantages can arise, such as the difficulty of generalizing this method in complex geometries, an issue that is common to face when the systems are dynamic, such as in the case of batteries. In this work, the finite difference method is used to convert partial differential equations, into a system of linear equations that can be solved by matrix algebra techniques.

Given the large spectrum of techniques we shall use in the next sections, it is relevant to mention the different methods' orders, to better understand the differences between the numerical methods in question. We say that we

have an error of order $p > 0$, if

$$|u(n\Delta t) - u^n| = C\Delta t^p \quad C \in \mathbb{R}, \tag{4.4}$$

considering that u depends only on t and u^n is an approximate solution of $u(n\Delta t)$. Generally, first-order schemes provide lower accuracy. They have a global truncation error of order Δt, where Δt is the step size used in the numerical approximation. First-order schemes are suitable for solving PDEs when the solutions are rough or exhibit discontinuities. Finally, first-order schemes are often computationally cheaper because they use simpler approximations.

On the other hand, second-order schemes offer higher accuracy. They have a global truncation error of order Δt^2, which means they are more accurate for the same step size. Second-order schemes are better suited for smoother solutions. They perform well when the solution is continuous and has no sharp transitions. Second-order schemes may be computationally more expensive due to the higher-order approximations, but they provide more accurate results. Another issue we have to address is stability, that is the numerical approximation remains bounded over time. On the contrary, instability results in a blow-up of the solution in finite time.

The current study is based on this type of numerical method, as it provides a practical way to obtain numerical solutions for a wide range of problems.

4.1.3 Discretisation

As our advection-diffusion equation depends on time t and space x, to apply a finite differences method we must start by discretising the domains of these variables.

- Discretisation in time

  We perform the discretisation in time with a uniform grid. Let N be a positive integer and t^n the discrete times. We set

  $$t^n = n\Delta t, \quad n = 0, \cdots, N, \tag{4.5}$$

  where $\Delta t = T/N$ is the time step.

- discretisation in space

  Additionally, in the $x-$direction, considering a positive integer I and $\Delta x = 1/I$ we discretize on the uniform grid

  $$x_i = i\Delta x, \quad i = 0, \cdots, I. \tag{4.6}$$

- We denote by $u_i^n \approx u(t^n, x_i)$ the approximation of the solution over the grid.

4.2 Explicit schemes - Advection Equation

We studied explicit and implicit schemes separately applied to the advection and the diffusion equation. Afterward, we applied some of these methods to the complete advection-diffusion equation.

4.2.1 The upwind scheme

Considering the upwind scheme, a first-order numerical scheme, applied to the advection equation ($k = 0$ in (4.1)) we have, with $c > 0$ (W. A. Strauss, 2007)

$$\frac{u_i^{n+1} - u_i^n}{\Delta t} + c\frac{u_i^n - u_{i-1}^n}{\Delta x} = 0. \tag{4.7}$$

Consequently, given the solution u_i^n at time t^n, we compute the solution at time t^{n+1} with

$$u_i^{n+1} = u_i^n - \frac{c\Delta t}{\Delta x}\left(u_i^n - u_{i-1}^n\right) \tag{4.8}$$

Note that the scheme is conditionally stable under the condition $\frac{c\Delta t}{\Delta x} < 1$, named Courant Friedrisch Levy (CFL) condition.

4.2.2 Lax-Friedrichs scheme

The upwind scheme instability can be counterbalanced by the Lax-Friedrichs scheme, which is also a first-order numerical scheme. When we replace u_i^n by the spatial average $\frac{u_{i+1}^n + u_{i-1}^n}{2}$ in the previous scheme, we obtain,(W. A. Strauss, 2007)

$$u_i^{n+1} = \frac{1}{2}(u_{i+1}^n + u_{i-1}^n) + \frac{c\Delta t}{2\Delta x}(u_{i+1}^n - u_{i-1}^n). \tag{4.9}$$

Stability is guaranteed under the same conditions as the upwind scheme.

4.2.3 Lax-Wendroff scheme

The Lax-Wendroff scheme is the second-order extension of the Lax-Friedrichs scheme. A Lax-Wendroff method can be outlined in the following. In a first step u is evaluated at half time steps $n + \frac{1}{2}$ and half grid points $i + \frac{1}{2}$. In a second step values at the next time step, $n + 1$ are calculated using the data from n and $n + \frac{1}{2}$ (W. A. Strauss, 2007).

$$u_{i+\frac{1}{2}}^{n+\frac{1}{2}} = \frac{1}{2}(u_i^n + u_{i+1}^n) - \frac{c\Delta t}{2\Delta x}(u_{i+1}^n - u_i^n), \tag{4.10}$$

$$u_i^{n+1} = u_i^n - \frac{c\Delta t}{\Delta x}\left(u_{i+\frac{1}{2}}^{n+\frac{1}{2}} - u_{i-\frac{1}{2}}^{n+\frac{1}{2}}\right). \tag{4.11}$$

Stability holds under the Courant Fredriesch Levy condition.

4.3 Implicit schemes - Advection equation

Implicit schemes in time differ from explicit schemes in that the solution at the next time point u^{n+1} depends on the values of the solution at the current time point u^n and the next time point u^{n+1}, whereas in explicit schemes, the solution at the next time step only depends on the solution at the current time step.

4.3.1 Implicit Euler scheme

In this section, we propose an implicit Euler scheme, which is a basic, first-order implicit method. Its advantage is the stability of the scheme, a significant time step can be used when necessary. So the implicit Euler differential scheme is more robust, it can be applied to a wide range of problems. Consider the following semi-discretized advection equation, with a forward difference in space:

$$\partial_t u_{x_i} = -c\frac{u_i(t) - u_{i-1}(t)}{\Delta x} + f(x_i, t) \tag{4.12}$$

discretisation using a forward difference also in time gives the scheme:

$$\frac{u_i^{n+1} - u_i^n}{\Delta t} = -c\frac{u_i^{n+1} - u_{i-1}^{n+1}}{\Delta x} + f_i^n \tag{4.13}$$

$$u_i^{n+1}\left(1 + \frac{c\Delta t}{\Delta x}\right) - \frac{c\Delta t}{\Delta x}u_{i-1}^{n+1} = u_i^n + \Delta t f_i^n \tag{4.14}$$

If we denote $C = \frac{c\Delta t}{\Delta x}$, the equation above can be written

$$u_i^{n+1}(1 + C) - Cu_{i-1}^{n+1} = u_i^n + \Delta t f_i^n \tag{4.15}$$

In a matrix form:

$$\begin{bmatrix} u_1^{n+1} \\ u_2^{n+1} \\ \vdots \\ u_{I-1}^{n+1} \\ u_I^{n+1} \end{bmatrix} = A^{-1}\left(\begin{bmatrix} u(t^n, x_1) \\ u_2^n \\ \vdots \\ u_{I-1}^n \\ u_I^n \end{bmatrix} + \Delta t \begin{bmatrix} f_1^n \\ f_2^n \\ \vdots \\ f_I^n \end{bmatrix}\right) \tag{4.16}$$

where

$$A = \begin{bmatrix} 1 & & \cdots & & & 0 \\ -C & 1+C & 0 & \cdots & & 0 \\ \vdots & & & \ddots & \ddots & \cdots \\ 0 & & \cdots & -C & 1+C & 0 \\ 0 & & \cdots & & & 1 \end{bmatrix}$$

and $u(t^n, x_1)$ is the Dirichlet boundary condition.

4.3.2 Crank-Nicolson scheme

The Crank-Nicolson scheme is a second-order numerical scheme and can be used in the numerical treatment of the advection equation. It consists of a time average-centered difference and is given by the following expressions. is(W. A. Strauss, 2007):

$$u_i^{n+1} = u_i^n - \frac{c\Delta t}{4\Delta x}\left[\left(u_{i+1}^n - u_{i-1}^n\right) + \left(u_{i+1}^{n+1} - u_{i-1}^{n+1}\right)\right] + f_i^n. \tag{4.17}$$

With $C = \frac{c\Delta t}{4\Delta x}$ gives,

$$-Cu_{i-1}^{n+1} + u_i^{n+1} + Cu_{i+1}^{n+1} = Cu_{i-1}^n + u_i^n - Cu_{i+1}^n + \Delta t f_i^n. \tag{4.18}$$

Let us solve this problem in a matrix form. We express this as a linear system problem, where $C = \frac{c\Delta t}{4\Delta x}$:

$$\begin{bmatrix} u_1^{n+1} \\ u_2^{n+1} \\ \vdots \\ u_{I-1}^{n+1} \\ u_I^{n+1} \end{bmatrix} = A_l^{-1}\left(\begin{bmatrix} u(t^n, x_1) \\ 0 \\ \vdots \\ 0 \\ u(t^n, x_I) \end{bmatrix} + A_r \begin{bmatrix} u_1^n \\ u_2^n \\ \vdots \\ u_{I-1}^n \\ u_I^n \end{bmatrix} + \begin{bmatrix} f_1^n \\ f_2^n \\ \vdots \\ f_{I-1}^n \\ f_I^n \end{bmatrix}\right) \tag{4.19}$$

Where $u(t^n, x_1) = u(t^n, x_I)$ for all n (if considering periodic boundary conditions),

$$A_l = \begin{bmatrix} 1 & & & & 0 \\ -C & 1 & C & & \\ & \ddots & \ddots & \ddots & \\ & & -C & 1 & C \\ 0 & & & & 1 \end{bmatrix} \quad \text{and} \quad A_r = \begin{bmatrix} 0 & & & & 0 \\ C & 1 & -C & & \\ & \ddots & \ddots & \ddots & \\ & & C & 1 & -C \\ 0 & & & & 0 \end{bmatrix}.$$

4.4 Explicit schemes - Diffusion Equation

The introduction of viscosity/diffusion into the description of a fluid introduces significant challenges when numerically solving hydrodynamic equations. Analytically, this results in a transformation from purely hyperbolic PDEs to mixed hyperbolic-parabolic PDEs. Consequently, the numerical methods employed to solve these equations must have the capability to handle the parabolic components effectively. Therefore, it is advisable to have a thorough grasp of the fundamental parabolic equation, such as the one-dimensional diffusion equation, both from analytical and numerical perspectives before tackling the solution of mixed hyperbolic-parabolic PDEs (Rezzolla, 2011). For this reason, different models were applied when studying the diffusion equation.

4.4.1 The Forward in Time Centered in Space (FTCS) method

FTCS method is the direct way to solve the pure diffusion equation, where($c = 0$ in (4.1)) we have, with $k > 0$ (W. A. Strauss, 2007)

$$\frac{u_i^{n+1} - u_i^n}{\Delta t} - k\frac{u_{i+1}^n - u_i^n + u_{i-1}^n}{\Delta x^2} = f_i^n, \tag{4.20}$$

with $f_i^n = f(t^n, x_i)$(Rezzolla, 2011) Consequently, given the solution u_i^n at time t^n, we compute the solution at time t^{n+1} with

$$u_i^{n+1} = u_i^n - \frac{k\Delta t}{\Delta x^2}\left(u_{i+1}^n - u_i^n + u_{i-1}^n\right) + \Delta t f_i^n. \tag{4.21}$$

The hyperbolic equation leads to an unstable FTCS method, consequently, it is necessary a von Newmann stability analysis that leads to the introduction of the stability criteria(Rezzolla, 2011):

$$\gamma := 2k\frac{\Delta t}{\Delta x^2} \leq 1 \tag{4.22}$$

The stability condition discussed here restricts the use of specific numerical methods in scientific calculations, particularly when dealing with complex multidimensional problems. These methods require many time steps to yield accurate results, and they are only first-order accurate in terms of time. Therefore, it is necessary to explore alternative methods to improve accuracy and computational efficiency in such scenarios(Rezzolla, 2011).

4.5 Implicit schemes - Diffusion equation

Explicit schemes are at most conditionally stable leading to a very strong restriction on the time step. On the other hand, implicit schemes are typically unconditionally stable.

4.5.1 Implicit Euler scheme - Backward-time-centered-space (BTCS)

In this section, we propose an implicit Euler scheme, which is a first-order and basic implicit method. Its advantage is the stability of the scheme, a significant time step can be used when necessary. So the implicit Euler differential scheme is more universal, it can be applied to a wide range of problems.

The BTCS scheme reads (W. A. Strauss, 2007):

$$\frac{u_i^{n+1} - u_i^n}{\Delta t} = k\frac{u_{i+1}^{n+1} - 2u_i^{n+1} + u_{i-1}^{n+1}}{\Delta x^2} + f_i^n$$

Rearranging the terms it is easy to obtain:

$$-Du_{i-1}^{n+1} + (1+2D)u_i^{n+1} - Du_{i+1}^{n+1} = u_i^n + \Delta t f_i^n, \tag{4.23}$$

where $D = \frac{k\Delta t}{\Delta x^2}$. The equation above can be written in a matrix form:

$$\begin{bmatrix} u_1^{n+1} \\ u_2^{n+1} \\ \vdots \\ u_{I-1}^{n+1} \\ u_I^{n+1} \end{bmatrix} = A^{-1} \left(\begin{bmatrix} u(t^n, x_1) \\ u_2^n \\ \vdots \\ u_{I-1}^n \\ u(t^n, x_I) \end{bmatrix} + \Delta t \begin{bmatrix} f_1^n \\ f_2^n \\ \vdots \\ f_{I-1}^n \\ f_I^n \end{bmatrix} \right) \tag{4.24}$$

where

$$A = \begin{bmatrix} 1 & 0 & 0 & \cdots & & 0 \\ -D & 1+2D & -D & \cdots & & \vdots \\ & \ddots & \ddots & & & \\ 0 & & \cdots & -D & 1+2D & -D \\ 0 & 0 & 0 & \cdots & & 1 \end{bmatrix}$$

always imposing the boundary conditions, $u(t^n, x_1)$, $u(t^n, x_I)$ for all $n = 1, \cdots, N$ if we have Dirichlet conditions.

4.5.2 Crank-Nicolson scheme

The Crank-Nicolson scheme can be used in the numerical treatment of the diffusion equation. It consists of an averaging of both the FTCS explicit scheme and the BTCS implicit scheme (W. A. Strauss, 2007):

$$\frac{u_i^{n+1} - u_i^n}{\Delta t} = \frac{k}{2} \frac{(u_{i+1}^{n+1} - 2u_i^{n+1} + u_{i-1}^{n+1}) + (u_{i+1}^n - 2u_i^n + u_{i-1}^n)}{\Delta x^2} + f_i^n. \tag{4.25}$$

Simplifying,

$$-Du_{i-1}^{n+1} + (1+2D)u_i^{n+1} - Du_{i+1}^{n+1} = Du_{i-1}^n + (1-2D)u_i^n + Du_{i+1}^n + \Delta t f_i^n \tag{4.26}$$

where $D = \frac{k\Delta t}{2\Delta x^2}$. Let us solve this problem in a matrix form. We express this as a linear system problem:

$$\begin{bmatrix} u_1^{n+1} \\ u_2^{n+1} \\ \\ \vdots \\ \\ u_{I-1}^{n+1} \\ u_I^{n+1} \end{bmatrix} = A_l^{-1} \left(\begin{bmatrix} u(t^n, x_1) \\ 0 \\ \\ \vdots \\ \\ 0 \\ u(t^n, x_I) \end{bmatrix} + A_r \begin{bmatrix} u_1^n \\ u_2^n \\ \\ \vdots \\ \\ u_{I-1}^n \\ u_I^n \end{bmatrix} + \begin{bmatrix} f_1^n \\ f_2^n \\ \\ \vdots \\ \\ f_{I-1}^n \\ f_I^n \end{bmatrix} \right) \tag{4.27}$$

with

$$A_l = \begin{bmatrix} 1 & & & & & 0 \\ -D & 1+2D & -D & & & \\ & \ddots & \ddots & \ddots & & \\ & & & -D & 1+2D & -D \\ 0 & & & & & 1 \end{bmatrix} \text{ and } A_r = \begin{bmatrix} 0 & & & \cdots & & 0 \\ D & 1-2D & D & 0 & \cdots & 0 \\ 0 & D & 1-2D & D & \cdots & \\ & \ddots & \ddots & \ddots & & \\ 0 & & \cdots & D & 1-2D & D \\ 0 & & & \cdots & & 0 \end{bmatrix}.$$

4.6 Explicit schemes - Advection-Diffusion Equation

In this study, the explicit method forward time and centered space (FTCS) scheme will be used to obtain the numerical solutions for the advection–diffusion equation.

4.6.1 Forward in Time Centered in Space (FTCS) method

Bearing in mind equations (4.7) and (4.20) which were discretized previously, using the forward difference formula for the temporal step, centered difference formula for the first derivative, and the second derivative in space, it is given, with $k > 0$, and $c > 0$(Ara, Rahaman, & Alam, 2021),

$$\frac{u_i^{n+1} - u_i^n}{\Delta t} = -c\frac{u_{i+1}^n - u_{i-1}^n}{2\Delta x} + k\frac{u_{i-1}^n - 2u_i^n + u_{i+1}^n}{\Delta x^2} + f_i^n$$

which can written in the form

$$u_i^{n+1} = (\frac{k\Delta t}{\Delta x^2} - \frac{c\Delta t}{2\Delta x})u_{i+1}^n + (1 - \frac{2k\Delta t}{\Delta x^2})u_i^n + (\frac{k\Delta t}{\Delta x^2} + \frac{c\Delta t}{2\Delta x})u_{i-1}^n + \Delta t f_i^n. \quad (4.28)$$

The von Newmann stability analysis leads to the introduction of the stability condition:

$$(\frac{c\Delta t}{\Delta x})^2 \leq 2K\frac{\Delta t}{\Delta x^2} \leq 1 \quad (4.29)$$

Notice that the condition (4.29) also preserves the positivity of the solution which is a crucial issue when dealing with concentrations.

4.7 Implicit schemes - Advection-diffusion equation

Explicit schemes usually require conditions to demonstrate stability. On the other hand, implicit schemes are typically unconditionally stable.

4.7.1 Implicit Euler scheme

This approach involves the use of a forward difference, a first-order scheme, to approximate the first derivative of functions and a central difference scheme for the second derivative, each applied as appropriate. The resulting numerical scheme considering equations (4.15) and (4.23), is(Ara et al., 2021)

$$u_i^n + \Delta t f_i^n = (-C - D)u_{i-1}^{n+1} + (1 + C + 2D)u_i^{n+1} - Du_{i+1}^{n+1}, \tag{4.30}$$

where $D = \frac{k\Delta t}{\Delta x^2}$, and $C = \frac{c\Delta t}{\Delta x}$. The equation above can be written in a matrix form:

$$\begin{bmatrix} u_1^{n+1} \\ u_2^{n+1} \\ \vdots \\ u_{I-1}^{n+1} \\ u_I^{n+1} \end{bmatrix} = A^{-1} \left(\begin{bmatrix} u(t^n, x_1) \\ u_2^n \\ \vdots \\ u_{I-1}^n \\ u(t^n, x_I) \end{bmatrix} + \Delta t \begin{bmatrix} f_1^n \\ f_2^n \\ \vdots \\ f_{I-1}^n \\ f_I^n \end{bmatrix} \right) \tag{4.31}$$

where

$$A = \begin{bmatrix} 1 & 0 & \cdots & & 0 \\ -C - D & (1 + C + 2D) & -D & \cdots & \\ & \ddots & \ddots & & \\ 0 & & \cdots & -C - D & (1 + C + 2D) & -D \\ 0 & & & \cdots & & 1 \end{bmatrix}.$$

4.7.2 Crank-Nicolson scheme

In the implicit Crank–Nicholson type technique we replace all spatial derivatives with the average of their values at the n and $n + 1$ time levels and then substitute centered-difference forms for all derivatives, combining equations (4.18) and (4.26), we have

$$(-C-D)u_{i-1}^{n+1}+(1+2D)u_i^{n+1}+(C-D)u_{i+1}^{n+1} = (C+D)u_{i-1}^n+(1-2D)u_i^n+(-C+D)u_{i+1}^n+\Delta t f_i^n \tag{4.32}$$

Where $D = \frac{k\Delta t}{(2\Delta x)^2}$ and $C = \frac{c\Delta t}{\Delta x}$. The resulting linear system is

$$\begin{bmatrix} u_1^{n+1} \\ u_2^{n+1} \\ \\ \vdots \\ \\ u_{I-1}^{n+1} \\ u_I^{n+1} \end{bmatrix} = A_l^{-1} \left(\begin{bmatrix} u(t^n, x_1) \\ 0 \\ \\ \vdots \\ \\ 0 \\ u(t^n, x_I) \end{bmatrix} + A_r \begin{bmatrix} u_1^n \\ u_2^n \\ \\ \vdots \\ \\ u_{I-1}^n \\ u_I^n \end{bmatrix} + \Delta t \begin{bmatrix} f_1^n \\ f_2^n \\ \\ \vdots \\ \\ f_{I-1}^n \\ f_I^n \end{bmatrix} \right) \tag{4.33}$$

with

$$A_l = \begin{bmatrix} 1 & & & & & 0 \\ -C-D & 1+2D & C-D & & & \\ & \ddots & \ddots & \ddots & & \\ & & & -C-D & 1+2D & C-D \\ 0 & & & & & 1 \end{bmatrix}$$

$$A_r = \begin{bmatrix} 0 & & & \cdots & & 0 \\ C+D & 1-2D & -C+D & 0 & \cdots & 0 \\ 0 & C+D & 1-2D & -C+D & \cdots & \\ & \ddots & \ddots & \ddots & & \\ 0 & & \cdots & C+D & 1-2D & -C+D \\ 0 & & & \cdots & & 0 \end{bmatrix}.$$

Note that, even being implicit, the scheme may suffer from instability when we are dealing with strong velocity versus the diffusive process (Peclét number $>> 1$).

4.8 Benchmarks for explicit schemes

- Advection equation

A solution for the advection equation (equation (4.1) with $k = 0$)

$$\partial_t u(x,t) + c\partial_x u(x,t) = f(x,t), \quad t \in [0,1],\, x \in [0,1]$$

with $c > 0$, the initial condition $u(x,0) = \sin(2\mathbf{k}\pi x),\ (\mathbf{k} \in \mathbb{Z})$ and boundary Dirichlet condition

$$u(0,t) = \sin(-2\mathbf{k}\pi ct), \qquad u(1,t) = sin(2\mathbf{k}\pi(1-ct)) = sin(-2\mathbf{k}\phi ct)$$

has an analytic expression given by,

$$u(x,t) = \sin(2\mathbf{k}\pi(x-ct)),$$

where the source term is $f(x,t) = 0$. The sine function is commonly used to model periodic phenomena.

In order to study the different explicit methods, we used different frequencies:

- $\mathbf{k} = 1; \mathbf{k} = 4; \mathbf{k} = 10$ and
- different pairs of numbers of time and space points (N and I):
  - $N = 150, I = 100$;
  - $N = 300, I = 200$;

- $N = 600, I = 400$;
- $N = 2400, I = 1600$.

The study was obtained by analyzing the exact solution (red curve) with the approximated solution obtained from the different numerical schemes (black curve). The various simulations were tested through different methods in order to evaluate their stability. In the context of this thesis, the inclusion of specific representative examples is a deliberate choice aimed at enhancing clarity and comprehension. Selecting only a subset of examples that are representative of the broader dataset or topic serve the purpose of reducing information overload.

The Upwind scheme showed that, as the values of time and space increase, the precision and accuracy improve, as Figure 1 (a) and (b) illustrates. On the other hand, as the frequency increases the approximation decreases its precision, see Figure 1 (b) and (c).

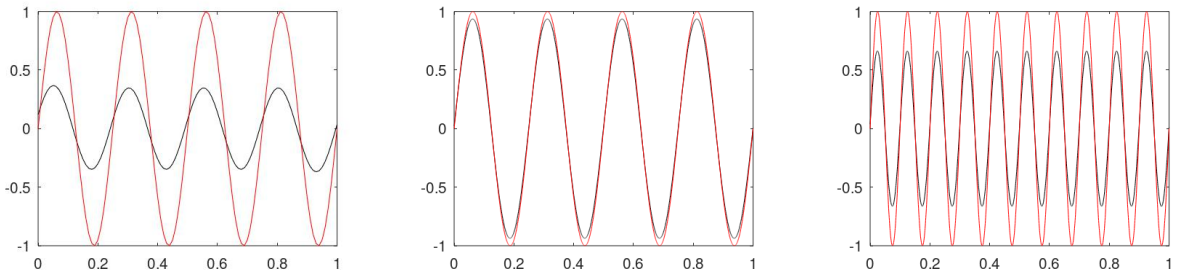

(a) k $= 4$ and $N = 150; I = 200$. **(b) k** $= 4$ and $N = 2400; I = 1600$. **(c) k** $= 10$ and $N = 2400; I = 1600$.

Figure 1: Simulation diagrams of the Upwind scheme.

This demonstrates that the Upwind scheme is less accurate when the frequency is higher. Concluding that this scheme is not a good scheme at higher frequencies, losing its studying interest. The same results were found in the other explicit schemes (Lax-Friedrichs and Lax-Wendroff).

Even though all schemes showed similar behaviors towards the different variations in time, space, and frequency, the Lax-Wendroff has a very accurate precision and approximation of the solution even at lower values of time and frequency, managing to attain greater precision even when the frequency is higher.

Figure 2 shows a side-by-side comparison of the three numerical schemes, for $k = 4$ and $N = 600; I = 400$. We can deduce that the Lax-Wendroff scheme gives a better approximation to the exact solution, while the Lax-Freidrich presents a lower degree of precision when comparing the exact solution with the approximation.

A statistical evaluation was made by calculating the error

$$err = \sum_{n=1}^{N} \sum_{i=1}^{I} |u_i^n - u(t^n, x_i)|$$

associated with each scheme, at the time, space, and frequency of the representative example. It is clear that the lowest error is associated with the Lax-Wendroff scheme ($err = 2.05e - 03$ at N=2400 and I=1600), and the

highest error is correlated with the Lax-Freidrich scheme ($err = 1.52e-02$ at N=2400 and I=1600), the upwind scheme showed an intermediate value ($err = 6.54e-02$ at N=2400 and I=1600), as we can see in Table 4.1.

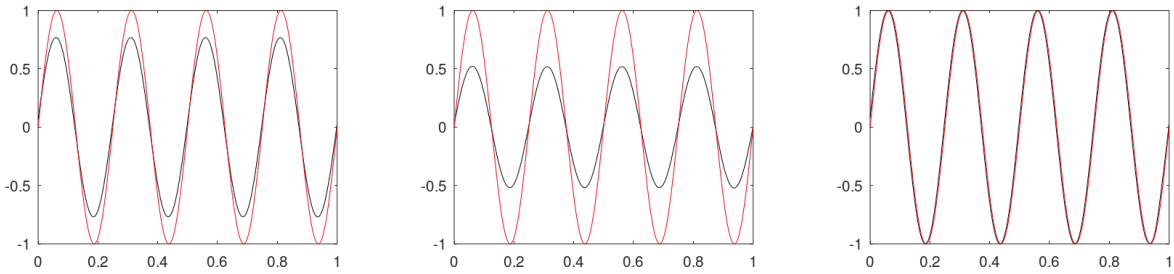

(a) Upwind scheme **(b)** Lax-Freidrich scheme **(c)** Lax-Wendroff scheme

Figure 2: Simulation diagrams with frequency **k** $= 4$ and $N = 600; I = 400$.

Table 4.1: Error for each scheme.

	k	Upwind	Lax-Freidrich	Lax-Wendroff
$N = 150; I = 100$	4	$1.51e-1$	$9.26e-1$	$4.19e-1$
$N = 300; I = 200$	4	$2.38e-1$	$7.29e-1$	$1.86e-1$
$N = 600; I = 400$	4	$4.21e-1$	$4.81e-1$	$8.65e-2$
$N = 2400; I = 1600$	4	$6.54e-2$	$1.52e-1$	$2.05e-2$

- Diffusion equation

A solution for the diffusion equation (equation (4.1) with $c = 0$)

$$\partial_t u(x,t) - k\partial_{xx} u(x,t) = f(x,t), \quad t \in [0,1],\, x \in [0,1]$$

with $k > 0$, initial condition $u(x,0) = \sin(2\mathbf{k}\pi x)$, ($\mathbf{k} \in \mathbb{Z}$) and boundary Dirichlet conditions $u(0,t) = u(t,1) = 0$, (in this case are even periodic) is

$$u(x,t) = \sin(2\mathbf{k}\pi x)\exp(-at) \tag{4.34}$$

with $a = k(2\pi\mathbf{k})^2$ and the source term $f(x,t) = 0$.

Similar to the advection equation, the same methods of analysis were established for the diffusion equation. Figure 3 illustrates the output with the FTCS method, it showed great results under different conditions, with a very low error ($err = 4.93e^{-7}$). When the time and space varied the scheme remained stable and no significant difference in the error was noticed, demonstrating good precision and good stability. Yet, this method must respect a stability condition (condition (4.22)). When this inequality is not satisfied, the method becomes very unstable (such is displayed in Figure 3(b)). This reveals a limitation of this method, the time step must be small enough such that the condition is satisfied, leading to a great computational effort. Instabilities take place leading to a blow-up of the numerical solution.

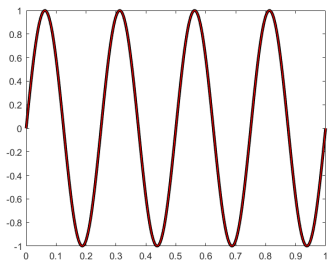

(a) FTCS explicit method.**k** =4 e N=600, I=400

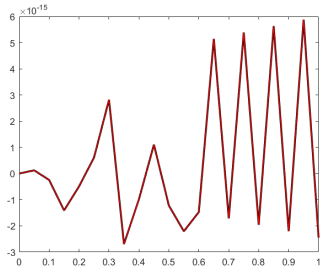

(b) FTCS explicit method. Instability moment. **k** =4 e N=500, I=400

Figure 3: Simulation diagrams with frequency $\mathbf{k} = 4$ and different N and I.

- Advection-diffusion equation

A solution for the advection-diffusion equation (equation (4.1))

$$\partial_t u(x,t) + c\partial_x u(x,t) - k\partial_{xx} u(x,t) = f(x,t), \quad t \in [0,1],\, x \in [0,1]$$

with $c > 0,\ k > 0$, the initial condition $u(x,0) = \sin(2\mathbf{k}\pi x),\ (\mathbf{k} \in \mathbb{Z})$ and boundary Dirichlet conditions

$$u(0,t) = \sin(-2\mathbf{k}\pi ct) \text{ and } u(t,1) = \sin(2\mathbf{k}\pi(1-ct)),$$

can be written as

$$u(x,t) = \sin(2\mathbf{k}\pi(x-ct)),$$

where the source term is $f(x,t) = k(2\mathbf{k}\pi)^2 u(x,t)$.

For the advection-diffusion equation, the same conditions of time and space (N and I), for instance, N=600, I=400, were not possible to apply. The von Newman stability analysis showed that the scheme FTCS is highly unstable, so the equation 4.29, needs to be addressed. In order to satisfy this condition, the time needs to increase or the space to decrease in value. The conditions used to test this scheme are represented in Figure 4. Figure 4 (b) reveals that when $N = 700, I = 200$ the scheme is not stable, hence it requires either increasing the time or decreasing the space. For this experiment's purpose N was increased up to $N = 900$. In this case, the scheme showed higher stability (when compared to the previous case), yet low precision with an error of $err = 5.2854e-01$. In conclusion, this scheme is neither stable nor precise, representing a poor choice for studying the advection-diffusion equation. Consequently, this is not a suitable scheme for the resolution of this equation.

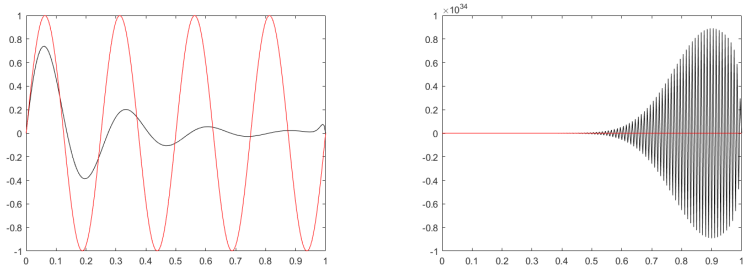

(a) FTCS explicit method. **k** =4 e N=900, I=200.

(b) FTCS explicit method. Instability moment. **k**=4 e N=600, I=400

Figure 4: Simulation diagrams of the explicit FCTS scheme for the advection-diffusion equation.

4.9 Benchmarks for implicit schemes

We used the same benchmarks as for explicit schemes.

- Advection equation

Similar to the used explicit benchmark for the advection equation, we choose $u(x,t) = \sin(2\mathbf{k}\pi(x-ct))$, with the same conditions. When analyzing the implicit schemes (implicit Euler scheme and Crank-Nicolson), the same situations (for the **k**, N and I that were given in the explicit scheme) were evaluated in order to understand them.

The values of N and I were gradually increased from 200 and 100 to 2400 and to 1600, respectively. Different ranges of frequencies were also studied (**k** $= 1$, **k** $= 4$, **k** $= 10$). In the implicit Euler scheme, when the time and space parameters N and I increase we report an improvement in precision, illustrated in Figure 5 (a) and (b), but the higher the frequencies more unstable the Euler scheme is, in Figure 5 (b) and (c).

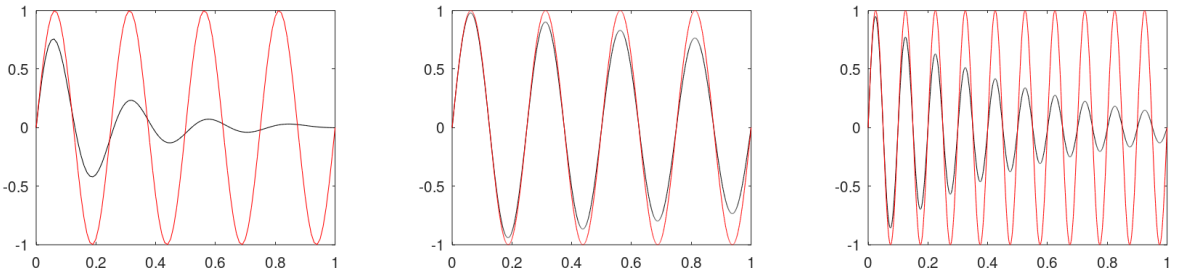

(a) **k** $= 4$ and $N = 150; I = 200$. **(b)** **k** $= 4$ and $N = 2400; I = 1600$. **(c)** **k** $= 10$ and $N = 2400; I = 1600$.

Figure 5: Implicit scheme Euler implicit method- Advection equation. Simulation diagrams.

The Crank-Nicolson implicit scheme exhibits the following behavior, as frequency increases in value the stability diminishes, represented in Figure 6 (c). The scheme becomes more unstable, less precise but still accurate. When the time and space parameters increase the scheme becomes more precise and less unstable and recovers stability.

Both schemes are represented in Figure 6 for **k** $= 4$ and $N = 600; I = 400$. By studying the same condition in both schemes it is evident that the implicit Euler scheme is less precise (see table 4.2) because the associated error is higher ($err = 2.66e-01$ at N=2400 and I=1600). Crank-Nicolson shows a better approximation to the solution, overall. The error ($err = 1.78e-03$ at N=2400 and I=1600), corroborates these findings.

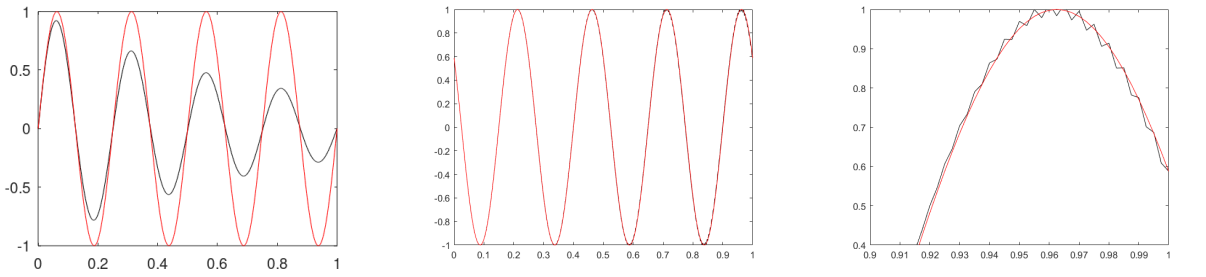

(a) Euler implicit scheme **(b)** Crank-Nicolson scheme **(c)** Crank-Nicolson scheme. Close-Up View.

Figure 6: Implicit schemes comparison - Advection equation. Simulation diagrams with frequency **k** $= 4$ and $N = 600; I = 400$.

Table 4.2: Maximum error for each scheme.

	Implicit Euler	Crank-Nicolson
$N = 150; I = 100$	1.01	$4.72e-1$
$N = 300; I = 200$	$7.13e-1$	$2.85e-2$
$N = 600; I = 400$	$7.13e-1$	$2.05e-2$
$N = 2400; I = 1600$	$2.66e-1$	$1.78e-3$

- Diffusion equation

The same method of analysis for the implicit methods was applied to the diffusion equation. We consider the same solution $u(x,t) = \sin(2\mathbf{k}\pi x)\exp(-at)$.

The FTCS and Crank-Nicolson implicit schemes were tested for the diffusion equation under the same conditions, a graphic comparison is illustrated in Figure 7. From the reported data, it is possible to conclude that both schemes have high precision, accuracy, and high stability as both curves are overlapped. From the error it is possible to compare both schemes from a statistical viewpoint, indicating that the Crank-Nicolson scheme is more precise ($err = 5.34e-05$). Yet, the computational cost does not justify the use of the Crank-Nicolson scheme, as the FCTS scheme is easier to implement and has shown as good results as the other scheme.

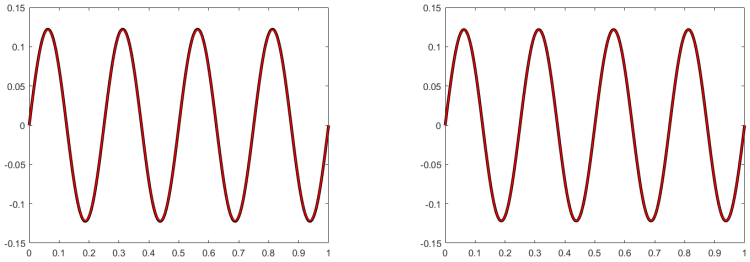

(a) Euler implicit scheme **(b)** Crank-Nicolson scheme

Figure 7: Implicit schemes - diffusion equation. Simulation diagrams with frequency **k** $= 4$ and $N = 600; I = 400$.

- Advection-diffusion equation

In this case, the solution is the same as in the explicit schemes analysis, $u(x,t) = \sin(2\mathbf{k}\pi(x-ct))$. Two implicit methods, the Euler implicit scheme, and the Crank-Nicolson were also tested for the advection-diffusion equation, illustrated in Figure 8. The data shows that both schemes are similar in precision and accuracy while demonstrating good stability. The error calculation revealed a better precision in the Crank-Nicolson case ($err = 9.249e-7$).

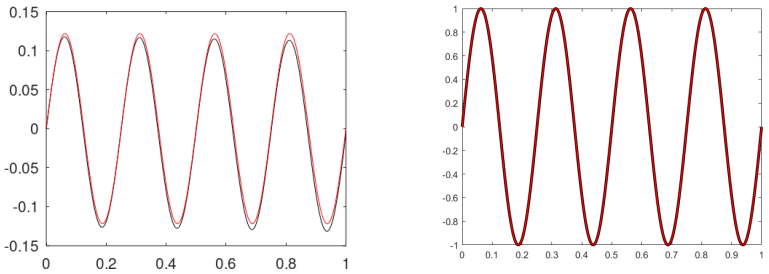

(a) Euler implicit scheme **(b)** Crank-Nicolson scheme

Figure 8: Implicit schemes - diffusion equation. Simulation diagrams with frequency $\mathbf{k} = 4$ and $N = 600; I = 400$.

4.10 Comparison between the different methods

For practical applications, the choice of a numerical method can significantly impact the quality of the solution. The Lax-Wendroff method, an explicit second-order scheme, has proven to be highly effective in solving advection equations, showcasing excellent stability, precision, and accuracy when compared to other methods. When dealing with the diffusion equation, the Euler implicit scheme, a first-order scheme, provides the best-approximated solution, demonstrating both precision and accuracy. Similarly, in the case of advection-diffusion equations, the use of implicit methods offers the most accurate approximations.

It's important to emphasize that the suitability of a specific numerical method depends on the unique conditions of the model and the nature of the equations being solved. Different methods may yield varying degrees of accuracy based on these factors.

Chapter 5

Model Formulation

The following chapter conveys the details of the formulated model, a 1D model, and a simplified version, the 0D model. The latter model will be the one of use for the numerical experiments, and so it will be accompanied by its discretisation.

Model Formulation

5.1 Model formulation - 1D model

In spite of significant advancements achieved over recent decades, the attempts to model the intricate architecture of batteries remain an ongoing challenge. The diverse spectrum of interrelated phenomena, mechanical, electrical, electrochemical, and thermal aspects, necessitates the development of a mathematical framework entailing a substantial quantity of variables, including displacements, electric potential, concentration, and temperature. Further complicating this task are the concurrent influences of multiphysics, which require non-linear relationships between variables, and multiscale effects, where varying observation scales are at play (Franco, 2013).

5.1.1 One Dimension Model - 1D Model

For this work, the battery geometry is reduced to a one-dimensional domain with the anode on the left side and then the electrolyte while the cathode is set on the right side. The physical processes involved in the functioning of the cell are explained through the equations present in the theoretical model, which is based on charge and discharge and mass conservation laws (Bhatt, 2011).

For the purpose of enhancing the comprehension of the model's dimensions, an image previously featured in a preceding chapter (chapter 1) will be included here (Figure 1).

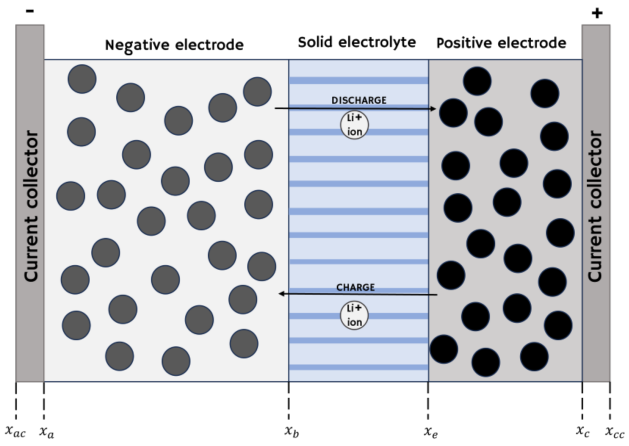

Figure 1: Illustration of an LFP half-cell with a solid-state electrolyte with associated dimensions.

5.1.2 Governing equations

The main quantities we aim to determine are:

- the bulk concentration of the Lithium ions c_{i}, that is governed by Fick's law.
- the bulk electronic potential ϕ_{i}, determined by Kirchhoff's law.
- the anode potential (solid) ϕ_{a}, determined by Ohm's law.
- cathode potential (solid) ϕ_{c}. determined by Ohm's law.

From these quantities, we deduce the bulk current density i_{i}, the anode current density i_{a}, and the cathode current density i_{c}. At last, we obtain the macroscopic quantities, namely the intensity I and the anode and cathode potential we shall couple with the external circuit.

5.1.3 Butler-Volmer equation - Reaction rate

The electrochemical kinetics of the charge transfer reactions are modeled according to the Butler-Volmer equation. This equation describes the relation between the potential at the electrode and the rate of the electrochemical reaction, making it a crucial tool in electrochemical research and applications. The current flow results from the process of lithium insertion or extraction at the electrode-electrolyte interface, which either consumes or produces Li^+ ions. This phenomenon is commonly named as the **reaction rate**, which is dictated by the Butler-Volmer equation (J. Wu & Xu, 2002).

The major difficulty begins with the Butler-Volmer equation since there are two possible formulations: as a charge rate transfer $[C/m^2s] = [A/m^2]$ or as a mole rate transfer $[mol/m^2s]$. Faraday constant F,$([C/mol])$ provides the correspondence between the two formulations. Note that, in this thesis, the mole rate transfer seems to be more relevant. Indeed, for multi-charge problems (an ion has $\aleph$ positive charges), the conversion uses coefficient $\aleph F$.

The **Butler-Volmer equation** in the **anode** provides the ion rate transfer in $[mol/m^2s]$ given by $G_{\mathrm{a}} = G_{\mathrm{a}0}(C_{\mathrm{Li}}) \cdot \chi_{\mathrm{a}}(\eta_{\mathrm{a}})$, (J. Wu & Xu, 2002) where

$$\chi_{\mathrm{a}}(\eta_{\mathrm{a}}) = \exp\left(\alpha_{\mathrm{a}}\frac{F\eta_{\mathrm{a}}}{2RT}\right) - \exp\left((\alpha_{\mathrm{a}}-1)\frac{F\eta_{\mathrm{a}}}{2RT}\right), \quad \eta_{\mathrm{a}} = \phi_{\mathrm{a}} - \phi_{\mathrm{i}} - U_{\mathrm{a}}, \tag{5.1}$$

with α_{a} the kinetic transfer power, F the Faraday constant ($[C/mol]$), $T([K])$ is the temperature, $R([J/molK])$ the gas constant, $\eta_{\mathrm{a}}([V])$ the overpotential in the anode, and $\eta_{\mathrm{a}} = \phi_{\mathrm{a}} - \phi_{\mathrm{i}} - U_{\mathrm{a}}$ where $\phi_{\mathrm{a}}([V])$ is the anode's potential, $\phi_{\mathrm{i}}([V])$ is the bulk potential and $U_{\mathrm{a}}([V])$ is the open circuit potential in the anode. The quantity $G_{\mathrm{a}0}([mol/m^2s])$ is the exchange ion density as a function of concentration, which is influenced by both, lithium maximum density and the lithium density in the anode.

$$G_{\mathrm{a}0}(C_{\mathrm{Li}}) = k_{\mathrm{a}0}(C_{\mathrm{Li}max} - C_{\mathrm{Li}})^{\alpha_{\mathrm{a}}} {C_{\mathrm{Li}}}_{max}^{1-\alpha_{\mathrm{a}}} {C_{\mathrm{Li}}}^{\alpha_{\mathrm{a}}} = k_{\mathrm{a}0} C_{\mathrm{Li}max}\left(\frac{(C_{\mathrm{Li}max} - C_{\mathrm{Li}})C_{\mathrm{Li}}}{C_{\mathrm{Li}max}}\right)^{\alpha_{\mathrm{a}}} \tag{5.2}$$

with $C_{\mathrm{Li}max}([mol/m^3])$ the maximum density of Lithium, $C_{\mathrm{Li}}(x,t)([mol/m^3])$ the density of lithium in the anode, α_{a} the kinetic transfer power and $k_{\mathrm{a}0}([m/s])$ the kinetic rate constant.

The **Butler-Volmer equation** in the **cathode** is given by $G_{\text{c}} = G_{\text{c}0}(C_{0\text{x}}) \cdot \chi_{\text{c}}(\eta_{\text{c}})$, where

$$\chi_{\text{c}}(\eta_{\text{c}}) = \exp\left(\alpha_{\text{c}}\frac{F\eta_{\text{c}}}{2RT}\right) - \exp\left((\alpha_{\text{c}}-1)\frac{F\eta_{\text{c}}}{2RT}\right) \qquad \eta_{\text{c}} = \phi_{\text{c}} - \phi_{\text{i}} - U_{\text{c}} \tag{5.3}$$

with α_{c} the kinetic transfer power and $\eta_{\text{c}}([V])$ the overpotential in the anode. The quantity $G_{\text{c}0}([mol/m^2s])$ is the exchange ion density,

$$G_{\text{c}0}(C_{0\text{x}}) = k_{\text{c}0}(C_{0\text{x}max} - C_{0\text{x}})^{\alpha_{\text{c}}} C_{0\text{x}_{max}}^{1-\alpha_{\text{c}}} C_{0\text{x}}{}^{\alpha_{\text{c}}} = k_{\text{c}0} C_{0\text{x}max}\left(\frac{(C_{0\text{x}max} - C_{0\text{x}})C_{0\text{x}}}{C_{0\text{x}max}}\right)^{\alpha_{\text{c}}} \tag{5.4}$$

with $C_{0\text{x}max}([mol/m^3]])$ the maximum density of oxide, $C_{0\text{x}}(x,t)([mol/m^3]])$ the density of oxide in the cathode, α_{c} the kinetic transfer power and $k_{\text{c}0}([m/s])$ the kinetic rate constant.

5.1.4 Electronic potential

We have to compute two distinct electrode potentials. Equations (5.5) and (5.6) respect Ohm's law, which states the principle that in an electrical circuit, the voltage, current, and resistance are related, (Castle, 2023).

• In the anode, for $x \in [x_{\text{a}}, x_{\text{b}}]$, we have, (Castle, 2023),

$$\partial_x(i_{\text{a}}) = -F\frac{G_{\text{a}}}{L_{\text{a}}}, \qquad i_{\text{a}} = -\sigma_{\text{a}}\partial_x\phi_{\text{a}}, \tag{5.5}$$

where ϕ_{a} is the electronic potential, $i_{\text{a}}([A/m^2])$ is the electric current density in the solid anode, σ_{a} the electric conductivity ($[S/m]$), $G_{\text{a}}([mol/m^3s])$ the charge transfer current in the cathode and L_{a} $([m^3/m^2])$ the specific active length. The boundary conditions are $A_{\text{a}}\sigma_{\text{a}}\partial_x\phi_{\text{a}}(x_{\text{a}},t) = -\text{I}_{\text{tot}}(t)$ with I_{tot} the total current in the external circuit, whereas $A_{\text{a}}\sigma_{\text{a}}\partial_x\phi_{\text{a}}(x_{\text{b}},t) = 0$, since no electron flows in the solid electrolyte. Constant $A_{\text{a}}([m^2])$ corresponds to the cross-sectional area of the anode, orthogonal to the Ox axis.

• In the cathode, for $x \in [x_{\text{e}}, x_{\text{c}}]$, we have

$$\partial_x(i_{\text{c}}) = -F\frac{G_{\text{c}}}{L_{\text{c}}}, \qquad i_{\text{c}} = -\sigma_{\text{c}}\partial_x\phi_{\text{c}}, \tag{5.6}$$

where ϕ_{c} is the electronic potential, $i_{\text{c}}([A/m^2])$ is the electric current density in the cathode, σ_{c} the electric conductivity $G_{\text{c}}([mol/m^3s])$ the charge transfer current in the cathode and L_{c} $([m^3/m^2])$ is the specific active length. The boundary conditions are $A_{\text{c}}\sigma_{\text{c}}\partial_x\phi_{\text{c}}(x_{\text{c}},t) = -\text{I}_{\text{tot}}(t)$ for the sake of conservation whereas $\sigma_{\text{c}}\partial_x\phi_{\text{c}}(x_{\text{e}},t) = 0$ since no electron flows in the solid electrolyte. Constant A_{c} corresponds to the cross-sectional area of the cathode, orthogonal to the Ox axis.

5.1.5 Species conservation equations (Li^+ conservation)

The lithium ion (Li^+) conservation, measured by $c_{\text{i}}([mol/m^2])$, the ion concentration in bulk, is given by the following equations:

• in the anode, for $x \in [x_{\mathrm{a}}, x_{\mathrm{b}}]$ (see Figure 1), is given by, (J. Wu & Xu, 2002),

$$\partial_t(\varepsilon_{\mathrm{a}}\, c_{\mathrm{i}}) + \partial_x(\mathcal{F}_{\mathrm{i}}) = (1 - \ t^+)\frac{G_{\mathrm{a}}}{L_{\mathrm{a}}}, \qquad \mathcal{F}_{\mathrm{i}} = -D_{\mathrm{a}}\, \partial_x c_{\mathrm{i}}, \tag{5.7}$$

where $\mathcal{F}_{\mathrm{i}}([mol/m^2 s])$ is the ionic flux in the bulk, ε_{a} $([m^3/m^3])$ the porosity of the anode, D_{a} $([m^2/s])$ the diffusion coefficient in the anode, L_{a} $([m^3/m^2])$ the specific active length, t^+ is the lithium transfer number and $G_{\mathrm{a}}([mol/m^2 s])$ the ion rate transfer in the anode;

• in the solid electrolyte, for $x \in [x_{\mathrm{b}}, x_{\mathrm{e}}]$, reads

$$\partial_t(\varepsilon_{\mathrm{s}}\, c_{\mathrm{i}}) + \partial_x \mathcal{F}_{\mathrm{i}} = 0, \qquad \mathcal{F}_{\mathrm{i}} = -D_{\mathrm{s}}\, \partial_x c_{\mathrm{i}}, \tag{5.8}$$

with ε_{s} $([m^3/m^3])$ the solid electrolyte porosity, $\mathcal{F}_{\mathrm{i}}([mol/m^2 s])$ the ionic flux in the bulk, and D_{s} $([m^2/s])$ the diffusion coefficient in the solid electrolyte;

• in the cathode, for $x \in [x_{\mathrm{e}}, x_{\mathrm{c}}]$, is given by

$$\partial_t(\varepsilon_{\mathrm{c}}\, c_{\mathrm{i}}) + \partial_x(\mathcal{F}_{\mathrm{i}}) = (1 - \ t^+)\frac{G_{\mathrm{c}}}{L_{\mathrm{c}}}, \qquad \mathcal{F}_{\mathrm{i}} = -D_{\mathrm{c}}\, \partial_x c_{\mathrm{i}}, \tag{5.9}$$

with ε_{c} $([m^3/m^3])$ the porosity of the cathode, D_{c} $([m^2/s])$ the diffusion coefficient in the cathode, L_{c} $([m^3/m^2])$ the specific active length, $\mathcal{F}_{\mathrm{i}}([mol/m^2 s])$ the ionic flux in the bulk, and $G_{\mathrm{c}}([mol/m^3 s])$ the charge transfer current in the cathode. For all species conservation equations, the boundary conditions are: $D_{\mathrm{a}}\, \partial_x c_{\mathrm{i}}(x_{\mathrm{a}}, t) = 0$ and $D_{\mathrm{c}}\, \partial_x c_{\mathrm{i}}(x_{\mathrm{c}}, t) = 0$, since the Li^+ ions do not leave the cell.

5.1.6 Charge conservation equations (Li^+ electric potential)

The charge conservation equation is used to determine the electrical potential.

• In the anode, $x \in [x_{\mathrm{a}}, x_{\mathrm{b}}]$, the electric potential equation takes the form (J. Wu & Xu, 2002):

$$\partial_x i_{\mathrm{i}} = F\frac{G_{\mathrm{a}}}{L_{\mathrm{a}}}, \quad i_{\mathrm{i}} = -\kappa_{\mathrm{a}}\partial_x \phi_{\mathrm{i}} - \kappa_{\mathrm{a}}\frac{2RT}{F}(1 - t^+)k_{\mathrm{a}}\partial_x(\ln(c_{\mathrm{i}})) \tag{5.10}$$

with $\kappa_{\mathrm{a}}([S/m])$ the ionic mobility in the anode, $i_{\mathrm{i}}([A/m^2])$ the current intensity, $\phi_{\mathrm{i}}([V])$ the bulk ionic potential and $k_{\mathrm{a}} = (1 + \frac{\partial f}{\partial \ln(c)})$ the activity of the anode. We can rewrite the previous equations as

$$-\partial_x(\kappa_{\mathrm{a}}\partial_x \phi_{\mathrm{i}}) = F\frac{G_{\mathrm{a}}}{L_{\mathrm{a}}} + \partial_x m_{\mathrm{i_a}}, \qquad m_{\mathrm{i_a}} = \kappa_{\mathrm{a}}\frac{2RT}{F}(1 - t^+)k_{\mathrm{a}}\left(\frac{\partial_x c_{\mathrm{i}}}{c_{\mathrm{i}}}\right). \tag{5.11}$$

• In the solid electrolyte, $x \in [x_{\mathrm{b}}, x_{\mathrm{e}}]$, we have

$$\partial_x i_{\mathrm{i}} = 0, \quad i_{\mathrm{i}} = -\kappa_{\mathrm{s}}\partial_x \phi_{\mathrm{i}} - \kappa_{\mathrm{s}}\frac{2RT}{F}(1 - t^+)k_{\mathrm{s}}\partial_x(\ln(c_{\mathrm{i}})) \tag{5.12}$$

with κ_{s} the ionic mobility in the solid electrolyte and k_{s} the activity of the solid electrolyte. Analogously, we can rewrite the previous equations as

$$-\partial_x(\kappa_{\mathrm{s}}\partial_x\phi_{\mathrm{i}}) = \partial_x m_{\mathrm{i_s}}, \qquad m_{\mathrm{i_s}} = \kappa_{\mathrm{s}}\frac{2RT}{F}(1-t^+)k_{\mathrm{s}}\left(\frac{\partial_x c_{\mathrm{i}}}{c_{\mathrm{i}}}\right) \tag{5.13}$$

• In the cathode $[x_{\mathrm{e}}, x_{\mathrm{c}}]$,

$$\partial_x i_{\mathrm{i}} = F\frac{G_{\mathrm{c}}}{L_{\mathrm{c}}}, \quad i_{\mathrm{i}} = -\kappa_{\mathrm{c}}\partial_x\phi_{\mathrm{i}} - \kappa_{\mathrm{c}}\frac{2RT}{F}(1-t^+)k_{\mathrm{c}}\partial_x(\ln(c_{\mathrm{i}})) \tag{5.14}$$

with κ_{c} the ionic mobility in the cathode and k_{c} the activity of the cathode. We can rewrite the problem as

$$-\partial_x(\kappa_{\mathrm{c}}\partial_x\phi_{\mathrm{i}}) = F\frac{G_{\mathrm{c}}}{L_{\mathrm{c}}} + \partial_x m_{\mathrm{i_c}}, \qquad m_{\mathrm{i_c}} = \kappa_{\mathrm{c}}\frac{2RT}{F}(1-t^+)k_{\mathrm{c}}\left(\frac{\partial_x c_{\mathrm{i}}}{c_{\mathrm{i}}}\right) \tag{5.15}$$

Boundary conditions are $\phi_{\mathrm{i}}(x_{\mathrm{a}}, t) = 0$ (null reference potential) and $\partial_x\phi_{\mathrm{i}}(x_{\mathrm{c}}, t) = 0$ (no ionic flux).

5.1.7 Molar flux of the two species - Lithium and oxide density

During the charge and discharge, we have variations of Lithium mass in the anode and Lithium Oxide in the cathode, leading to the lithiation/delithiation process. Basically, the material density (Lithium or Oxide) cannot reach up to a maximum $C_{\mathrm{Li}max}$ or $C_{\mathrm{0x}max}$, respectively. It is why there exists an expression for $G_{\mathrm{a_0}}$ that depends on the state of the electrodes. Several models attempt to model the mass variation (axisymmetric microscopic model), (Esfahanian, Dalakeh, & Aghamirzaie, 2019).

- Solid Lithium concentration in the porous anode is represented by $C_{\mathrm{Li}}([mol/m^3])$, and
- Solid Lithium Oxide concentration in the porous anode by $C_{\mathrm{0x}}([mol/m^3])$.

We propose the simple model:

- For the anode, $C_{\mathrm{Li}}([mol/m])$ represents the Lithium concentration, and the Lithium concentration is given in $([mol/m])$, because we assume it only depends on x. This means that we have a unidimensional system, and the volume $(/m^3)$ is no longer a relevant parameter. This equation computes the varying concentrations of lithium,

  $$\frac{\partial C_{\mathrm{Li}}}{\partial t} = -(1-\ t^+)\frac{G_{\mathrm{a}}}{L_{\mathrm{a}}} \tag{5.16}$$

  with $C_{\mathrm{Li}}(x, 0)$ given at the initial time $t = 0$.

- For the cathode C_{0x} represents the oxide, this equation computes the varying concentrations of oxide,

  $$\frac{\partial C_{\mathrm{0x}}}{\partial t} = -(1-\ t^+)\frac{G_{\mathrm{c}}}{L_{\mathrm{c}}} \tag{5.17}$$

  with $C_{\mathrm{0x}}(x, 0)$ given at the initial time $t = 0$.

Note that both C_{Li} and C_{0x} also depend on the space variable since G_{a} and G_{c} depend on x.

5.1.8 External Circuit

The external circuit is modeled depending on the charge or discharge

- Charge: The circuit is characterized by a voltage source $e(t)$ with an external resistance R_{ext} or by a prescribed current source $i(t)$.
- Discharge: The circuit is characterized by an external resistance R_{ext} (close circuit) or, by the null intensity (open circuit).

5.1.9 Boundary conditions revisited

Equations on the electronic potentials ϕ_{a} and ϕ_{c} (equations (5.5) and (5.6), respectively) provide a solution up to a constant (one constant for each domain). However, the constants are fundamental since the overpotentials η_{a} and η_{c} are the difference between electronic and ionic potential ϕ_{i} (see the second equation in (5.1) and (5.3)), leading to the definition of G_{a} and G_{c}. Therefore, the constants have to be adjusted such that the creation of G_{a} and G_{c} corresponds to the same total current $\mathrm{I}_{\mathrm{tot}}$ (see boundary conditions of equations (5.5) and (5.6)). To this end, we introduce an additional unknown ϕ_{a_+} and prescribe the boundary condition $\phi_{\mathrm{a}}(x_{\mathrm{a}}, t) = \phi_{\mathrm{a}_+}$. In the same way, we introduce the additional unknown ϕ_{c_+} and prescribe the boundary condition $\phi_{\mathrm{c}}(x_{\mathrm{c}}, t) = \phi_{\mathrm{c}_+}$. Notice that values ϕ_{a_+} and ϕ_{c_+} are part of the problem.

• If the total current is given, we fix the constants with the relation (see boundary conditions of equations (5.5) and (5.6)),

$$\sigma_{\mathrm{a}} \partial_x \phi_{\mathrm{a}}(x_{\mathrm{a}}, t) = \sigma_{\mathrm{c}} \partial_x \phi_{\mathrm{c}}(x_{\mathrm{c}}, t) = \mathrm{I}_{\mathrm{tot}}(t). \tag{5.18}$$

• If the total current is not given, but we know the resistance R_{ext} of the external circuit, one must have

$$\sigma_{\mathrm{a}} \partial_x \phi_{\mathrm{a}}(x_{\mathrm{a}}, t) = \sigma_{\mathrm{c}} \partial_x \phi_{\mathrm{c}}(x_{\mathrm{c}}, t) = \mathrm{I}_{\mathrm{tot}}(t), \quad \phi_{\mathrm{a}}(x_{\mathrm{a}}, t) - \phi_{\mathrm{c}}(x_{\mathrm{c}}, t) + R_{ext} \mathrm{I}_{\mathrm{tot}}(t) = 0. \tag{5.19}$$

5.2 Simplified Model - 0D Model

The one-dimensional (1D) model revealed a highly intricate and challenging nature. In pursuit of a more accessible and easier modeling framework for simulating battery behavior, substantial modifications were introduced to the original model. These adjustments facilitated the development of a zero-dimensional (0D) model, which offers a streamlined and comprehensible representation applicable to a battery. This model is simpler because it is a time-dependent model and a spatially constant model, so we call it the 0D Model.

5.2.1 Principles and assumptions - 0D model

General models of Li-ion batteries are based on three types of variables: the chemical concentrations, the electric potentials, together with the ionic and electric currents. We propose a simplification of the original 1D model by considering the following assumptions:

- Potential is almost constant in the anode, solid electrolyte, and cathode;
- Hence G_{a} and G_{c} do not depend on x;
- Intensities are linear piecewise functions in each subdomain;
- Ionic density j_{a} and j_{c} ($[A/m^3]$) are constant in space and only depend on time.

Always bear in mind the 1D model, as it was the starting point for the formulation of this more accessible 0D model. We simplified the name of some functions in the 0D model as they now only depend on time.

Assuming that G_{a} and G_{c} do not depend on x, the Lithium ion (Li-ion) concentration c_{ia} and Li-metal concentration C_{Li} in the anode, the Li-ion concentration c_{ic} and oxide concentration C_{0x} in the cathode only depend on time. In the 0D model, we consider $c_{\text{ia}}(t)$ the Lithium ion concentration in the anode and $c_{\text{ic}}(t)$ the ion concentration in the cathode instead of the bulk concentration of Lithium ions c_{i}.

Charge evolution is basically controlled by a non-stationary diffusion equation of type

$$\partial_t c - D\partial_{xx} c = f(c) \tag{5.20}$$

with c representing a species concentration and D the effective diffusion coefficient, see equations (5.7), (5.8) and (5.9). The characteristic time, Δt_{dif}, for ion diffusion in the cell is given by $\Delta t_{dif} = L^2/D$ with L the characteristic size of the cell, and D the diffusion coefficient. For illustrative purposes, taking $L = 10^{-5}m$ and $D = 10^{-13}$ (m^2/s) we get $\Delta t_{dif} = 1000 \leq 3600$. Hence, as a first approximation, we consider that the concentrations are almost constant in space in each subdomain (anode, cathode, interface) and only depend on time. Nevertheless, a diffusion process is necessary at the macroscopic level to transfer the Li-ion between the electrodes. We then add a source term that represents the diffusion between anode and cathode term $(c_{\text{ia}} - c_{\text{ic}})$ that

takes into account the conservation, with D_s ($[m^2\ s^{-1}]$) the effective diffusion and L_s ($[m^3/m^2]$) the characteristic length of the solid electrolyte.

5.2.2 Butler-Volmer equation - Reaction rate

The generation and depletion of lithium ions in an electrochemical process can be described using the Butler-Volmer equation, which is a fundamental equation in electrochemistry. This equation relates the rate of an electrochemical reaction to the overpotential and various kinetic parameters. The Butler-Volmer equation is typically used to describe the kinetics of electrode reactions in batteries.

Production and destruction of Li-ion is governed by the Butler-Volmer relation, from the 1D model (see equation (5.2)) reads $G_a(t) = F_a(t)S_a(t)$ with

$$F_a(t) = k_{a0}\ F\ C_{Limax}\left(\frac{(C_{Limax} - C_{Li}(t))C_{Li}(t)}{C_{Limax}}\right)^{\alpha_a} \tag{5.21}$$

where k_{a0} ($[m\ s^{-1}]$) is the kinetic rate in the anode in, C_{Li} ($[mol/m^3]$) the solid lithium concentration, C_{Limax} ($[mol/m^3]$) the maximum solid Lithium concentration, α_a the anode kinetic transfer power and F ($[C/mol]$) the Faraday constant.

We also have (see equation (5.1))

$$S_a(t) = \exp\left(\alpha_a\frac{F\eta_a(t)}{2RT}\right) - \exp\left((\alpha_a - 1)\frac{F\eta_a(t)}{2RT}\right), \tag{5.22}$$

where $\eta_a(t) = \phi_a(t) - U_a$, ($[V]$) is the overpotential in the anode, $\phi_a([V])$ is the potential in the anode, $U_a([V])$ is the open circuit potential, α_a the kinetic transfer power, F the Faraday constant, $T([K])$ the temperature and $R([J/molK])$ is the gas constant.

Notice that we are using a very simplified model where we assume that the ion concentrations are supposed to be in the same range, hence do not modify the kinetic of the chemical process.

On the other hand, we also use the Butler-Volmer equation associated with the cathode, from equation (5.4) we have $G_c(t) = F_c(t)S_c(t)$ with

$$F_c(t) = k_{c0}FC_{0xmax}\left(\frac{(C_{0xmax} - C_{0x}(t))C_{0x}(t)}{C_{0xmax}}\right)^{\alpha_c} \tag{5.23}$$

where k_{c0} ($[m\ \ s^{-1}]$) is the kinetic rate in the cathode, C_{0x} ($[mol/m^3]$) the Oxide concentration, C_{0xmax} ($[mol/m^3]$) the maximum solid Lithium concentration, α_c the anode charge transfer coefficient and F the Faraday constant.

We also have (see equation (5.3))

$$S_c(t) = \left[\exp\left(\alpha_c\frac{F\eta_c(t)}{2RT}\right) - \exp\left((\alpha_c - 1)\frac{F\eta_c(t)}{2RT}\right)\right], \tag{5.24}$$

where $\eta_c(t) = \phi_c(t) - U_c$, ($[V]$) is the overpotential in the cathode, $\phi_a([V])$ is the potential in the anode, $U_a([V])$ is the open circuit potential, α_c the kinetic transfer power, F the Faraday constant, $T([K])$ is the temperature and $R([J/molK])$ the gas constant.

Remark 5.2.1: Since U_a is the open circuit potential of the anode (negative electrode) and U_c for the cathode (positive electrode), one has $U_a < U_c$.

Advanced kinetic reaction laws

Charge and discharge processes in batteries are closely related to changes in the concentration of reactants and products within the electrochemical cell. The concentration of these species, typically ions in the electrolyte and active materials within the electrodes, change as a battery undergoes its charge and discharge cycles. The generation or consumption of Li-ions depends on the working mode of the battery (charge or discharge). The reaction rate expression changes with the signs of S_a and S_c (see equations (5.22) and (5.24), respectively) that characterize the mode. We assume that $C_{Li} \in [C_{Limin}, C_{Limax}]$ and $C_{0x} \in [C_{0xmin}, C_{0xmax}]$.

- Charge mode ($S_a < 0$ and $S_c > 0$): we have F_a depending on $C_{Limax} - C_{Li}$ and c_{ia} ($F_a = F_a(C_{Limax} - C_{Li}, c_{ia})$) and F_c as a function of $C_{0x} - C_{0xmin}$, ($F_c = F_c(C_{0x} - C_{0xmin})$). We then propose the relations

$$\begin{aligned} F_a &= k_{a0}^{-} c_{ia} \left(\frac{C_{Limax} - C_{Li}(t)}{C_{Limax}} \right)^{\alpha_a} \\ F_c &= k_{c0}^{+} C_{0xmax} \left(\frac{C_{0x}(t) - C_{0xmin}}{C_{0xmax}} \right)^{\alpha_c}. \end{aligned}$$

- Discharge mode ($S_a > 0$ and $S_c < 0$): in this case, we have F_a depending on $C_{Li} - C_{Limin}$, ($F_a = F_a(C_{Li} - C_{Limin})$), and F_c on $C_{0xmax} - C_{0x}$ and c_{ic} ($F_c = F_c(C_{0xmax} - C_{0x}, c_{ic})$). We then propose the relations

$$\begin{aligned} F_a &= k_{a0}^{+} F C_{Limax} \left(\frac{C_{Li} - C_{Limin}}{C_{Limax}} \right)^{\alpha_a} \\ F_c &= k_{c0}^{-} F c_{ic} \left(\frac{C_{0xmax} - C_{0x}}{C_{0xmax}} \right)^{\alpha_c}. \end{aligned}$$

The reaction rates brutally switch from one regime to the other when the polarity between the electrodes is switched. They are revealing the need to use different kinetic rates for the different reactions.

Remark 5.2.2: We assume a linear dependency between c_{ia} or c_{ic} concentration. Of course, more complex power laws could be experimented with.

5.2.3 Electronic potential

The term electrode potential typically refers to the electrochemical potential difference between the two electrodes (the anode and the cathode) within the battery. This potential difference, also known as the cell potential or electromotive force, arises from the electrochemical reactions at the two electrodes. The electrode potential in a battery is a fundamental concept used to understand the driving forces for electrochemical reactions and the resulting voltage that powers electronic devices. In this model, due to the high value of the electronic conductivity, we have assumed that the electric potentials ϕ_{a} and ϕ_{c} are almost constant in space and only depend on time. On the other hand, (electronic) intensity density in the solid electrolyte is zero since no electron crosses the interfaces (anode-solid electrolyte and cathode-solid electrolyte). Moreover, in the model construction, and since the potential is defined up to an arbitrary constant, we assume that there is no electric potential within the solid electrolyte.

Let i_{a} ($[A\ m^{-2}]$) be the electric current in the anode, t^+ the lithium transfer number, ε_{a} the porosity in the anode. Assuming that G_{a} is given in $[A\ m^{-2}]$ and s_{a} ($[m^2 m^{-3}]$) the specific active area, from equations (5.5), (5.10) one has,

$$\partial_x(i_{\text{a}}) = -\frac{1-\ t^+}{\varepsilon_{\text{a}}}\, s_{\text{a}} G_{\text{a}}(t) \tag{5.25}$$

Integration on space gives

$$i_{\text{a}}(x_{\text{b}}) - i_{\text{a}}(x_{\text{a}}) = -\frac{1-t^+}{\varepsilon_{\text{a}}} s_{\text{a}} L_{\text{a}}\, G_{\text{a}}(t) \tag{5.26}$$

where L_{a} ($[m^3 m^{-2}]$) is the specific active length in the anode. By using that the electronic intensity between the anode and the solid electrolyte is zero, we have $i_{\text{a}}(x_{\text{b}}) = 0$. We deduce that

$$i_{anode} = i_{\text{a}}(x_{\text{a}}) = \frac{1-t^+}{\varepsilon_{\text{a}}} s_{\text{a}} L_{\text{a}}\, G_{\text{a}}(t) \tag{5.27}$$

By introducing the effective area of the anode A_{a} ($[m^2]$), we obtain the intensity at the anode collector $I_{\text{a}}(t)$ in $[A]$ at the anode, from the boundary condition of equation (5.5)

$$I_{\text{a}}(t) = A_{\text{a}} s_{\text{a}} L_{\text{a}}\, G_{\text{a}}(t). \tag{5.28}$$

Using similar arguments (see equations (5.6) (5.14)) in the cathode, we integrate

$$\partial_x(i_{\text{c}}) = -\frac{1-t^+}{\varepsilon_{\text{c}}} s_{\text{c}} G_{\text{c}}(t) \tag{5.29}$$

on $[x_{\text{e}}, x_{\text{c}}]$ and get

$$i_{\text{c}}(x_{\text{c}}) - i_{\text{c}}(x_{\text{e}}) = -\frac{1-t^+}{\varepsilon_{\text{c}}} s_{\text{c}} L_{\text{c}}\, G_{\text{c}}(t) \tag{5.30}$$

with i_{c} ($[A\ m^{-2}]$) be the electronic current in the cathode, t^+ the lithium transfer number, ε_{c} the porosity in the cathode, L_{a} ($[m^3 m^{-2}]$) is the specific active length in the anode and s_{c} ($[m^2 m^{-3}]$) the specific active

area. Assuming that G_c is given in $[A\ m^{-2}]$ and s_c in $[m^2 m^{-3}]$, since no current crosses the interface solid electrolyte/cathode, we have $i_c(x_e) = 0$ and deduce

$$i_{cathode} = i_c(x_c) = -\frac{1-t^+}{\varepsilon_c} s_c L_c G_c(t) \tag{5.31}$$

Using the effective surface $A_c([m^2])$ of the cathode, we deduce from the boundary condition of equation (5.6) that the intensity (I_c) at the cathode collector is

$$I_c(t) = -A_c s_c L_c G_c(t). \tag{5.32}$$

5.2.4 Molar Flux of the two species - Lithium and oxide density

The molar flux of species in a battery, specifically lithium ions and oxide ions, is a measure of the flow rate of these ions through the various components of the battery, including the electrolyte and electrodes. Understanding molar flux is important for analyzing the transport of ions within the battery, which plays a crucial role in its operation.

Remark 5.2.3: At that stage, there exist many variations for the following reasons:

- A large part of the literature does not indicate the dimensions.
- j_a is in $[Am^{-3}]$, then j_a/F is in $[mol\ s^{-1}m^{-3}]$ while the concentration c_{ia} is given in $[mol\ m^{-3}]$.
- In some papers, the creation term G_a is given in current density $[Am^{-2}]$, and, in other papers, it is given as a flux of moles per surface $[mol\ s^{-1}m^{-2}]$ (the term $1/F$ has to be canceled in the ODE).
- Whatever the version, mole or charge, G_a is an expression per surface, while c_{ia} is an expression per volume. Hence, a characteristic length factor (labelled s_a in $[m^2\, m^{-3}]$) is mandatory, usually given by

  $$j_a = s_a G_a \tag{5.33}$$

  where s_a is in $[m^2 m^{-3}]$ called the specific active area/active interfacial area to volume ratio.
- In the literature s_a may have different expressions such as $s_a = 3\varepsilon_a/R_s$ where R_s is the radius of the grain structure.

Consequently, we have

$$j_a = s_a G_a(t), \qquad j_c = s_c G_c(t) \tag{5.34}$$

if G_a and G_c are given in $[Am^{-2}]$.

Evaluation of the diffusion term under conservation principle. Considering the previous remark, integration of the concentration on the volume of the anode ($L_a\, A_a$) gives (from equation (5.7) and the respective boundary condition)

$$\frac{dc_{ia}}{dt} L_a\, A_a - A_a D_a \frac{dc_{ia}}{dx}(x_b) = (1 - t^+)\frac{s_a G_a}{F\varepsilon_a} + st_a \tag{5.35}$$

where st_a is the source term, L_a ($[m^3m^{-2}]$) the specific active length in the anode, A_a ($[m^2]$) is the effective area of the anode, s_a($[m^2m^{-3}]$) the specific active area and D_a ($[m^2/s]$) is the diffusion coefficient in the anode. Notice that $\frac{dc_{ia}}{dt}$ represents the average value over the anode, hence it is a function that only depends on time, but we keep the same notation.

Similarly, integration of the concentration on the volume of the cathode ($L_c\,A_c$) gives (equation (5.9) and the respective boundary condition)

$$\frac{dc_{ic}}{dt}L_c\,A_c - A_cD_c\,\frac{dc_{ic}}{dx}(x_e) = (1-\ t^+)\frac{s_cG_c}{F\varepsilon_c} + st_c \tag{5.36}$$

with st_c the source term, L_c ($[m^3m^{-2}]$) the specific active length in the cathode, A_c($[m^2]$) is the effective area of the cathode, s_c($[m^2m^{-3}]$) the specific active area and D_c ($[m^2/s]$) is the diffusion coefficient in the cathode.
By the first law of thermodynamics, (conservation of energy), we get

$$A_aD_a\,\frac{dc_{ia}}{dx}(x_b) = A_cD_c\,\frac{dc_{ic}}{dx}(x_e)$$

where the derivatives are different. To compute the flux we have to estimate the flux with respect to the concentrations. We propose

$$D_a\,A_a\frac{dc_{ia}}{dx}(x_b) = D_c\,A_c\frac{dc_{ic}}{dx}(x_e) = D_s\,(A_sL_s)\,\frac{c_{ia}-c_{ic}}{{L_s}^2}. \tag{5.37}$$

where L_s the specific active length in the solid electrolyte, A_s is the effective area of the solid electrolyte, and D_s is the diffusion coefficient in the cathode. Substituting this proposal in the previous equations, we have for the anode

$$\frac{dc_{ia}}{dt} = (1-\ t^+)\frac{s_aG_a}{F\varepsilon_a} + D_s\,\frac{A_sL_s}{A_aL_a}\,\frac{c_{ia}-c_{ic}}{{L_s}^2} \tag{5.38}$$

and for the cathode

$$\frac{dc_{ic}}{dt} = (1-\ t^+)\frac{s_cG_c}{F\varepsilon_c} + D_s\,\frac{A_sL_s}{A_cL_c}\,\frac{c_{ia}-c_{ic}}{{L_s}^2}. \tag{5.39}$$

Observing that $A_s = (A_a + A_c)/2$, we get by eliminating the volumes

$$\frac{dc_{ia}}{dt} = (1-\ t^+)\frac{s_aG_a}{F\varepsilon_a} + \frac{A_a+A_c}{2A_a}\,\frac{D_s}{L_a\,L_s}(c_{ia}-c_{ic}) \tag{5.40}$$

and

$$\frac{dc_{ic}}{dt} = (1-\ t^+)\frac{s_cG_c}{F\varepsilon_c} + \frac{A_a+A_c}{2A_c}\,\frac{D_s}{L_c\,L_s}(c_{ia}-c_{ic}). \tag{5.41}$$

Also from the 1D model, we get the time rate of Lithium concentration in the anode (see equation (5.16))

$$\frac{dC_{Li}}{dt} = -\frac{1-\ t^+}{F}\,\frac{j_a(t)}{\varepsilon_a}, \tag{5.42}$$

where $j_a(t) = s_aG_a(t)$, with s_a($[m^2m^{-3}]$) the specific active area, G_a($[Am^{-2}$) the current density and j_a($[Am^{-3}]$) the flux in the anode. The time rate of Oxide concentration in the cathode (see equation (5.17)) is

$$\frac{dC_{Ox}}{dt} = -\frac{1-\ t^+}{F}\,\frac{j_c(t)}{\varepsilon_c}. \tag{5.43}$$

where $j_c(t) = s_cG_c(t)$, with s_c($[m^2m^{-3}]$) the specific active area, G_c($[Am^{-2}]$) the current density and j_c($[Am^{-3}]$) the flux in the cathode.

5.2.5 Exterior conditions

Two conditions have to be prescribed,

- Conservation of the intensity (Kirchhoff law)

$$I(t) = I_{\mathrm{a}}(t) = I_{\mathrm{c}}(t)$$

.

- Case of discharge characterized by an external resistance

$$\phi_{\mathrm{c}}(t) - \phi_{\mathrm{a}}(t) = R_{\mathrm{ext}}\, I(t)$$

- Case of charge characterized by an external resistance and an electromotive force $e(t)$. We get

$$\phi_{\mathrm{c}}(t) - \phi_{\mathrm{a}}(t) = R_{\mathrm{ext}}\, I(t) + e(t).$$

5.2.6 Some characteristic values

The battery geometry is represented in Figure 2.

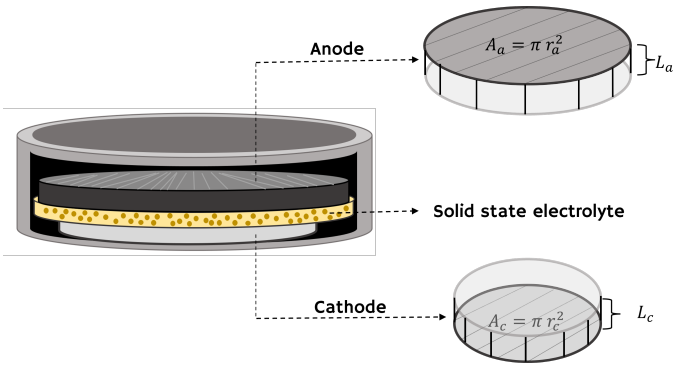

Figure 2: Geometry representation of a coin cell and associated are the characteristic values.

The characteristic values associated with the cell are as follows. For the geometry

$$L_{\mathrm{a}}, \approx 500\mu m,\ L_{\mathrm{c}} \approx 40\mu m,\ L_{\mathrm{s}} \approx 50\mu m, \quad \varepsilon_{\mathrm{a}}, \varepsilon_{\mathrm{c}} \approx 0.4, \qquad s_{\mathrm{a}}, s_{\mathrm{c}} \approx 10^7 m^{-1}, \quad A_{\mathrm{a}}, A_{\mathrm{c}} \approx 10^{-4} m^2.$$

For the concentrations

$$C_{\mathrm{Li}max} \approx 50000\ mol\, m^{-3}, \qquad C_{\mathrm{Ox}max} \approx 25000\ mol\, m^{-3}, \quad c_{\mathrm{ia}}, c_{\mathrm{ic}} \approx\ 1000.$$

For the kinetic

$$j_{0\mathrm{a}}, j_{0\mathrm{c}} \in [10^{-5}, 10^{-4}] A\, m^{-2}.$$

5.3 Discretisation

Approximations' computation requires two main stages. An update in time of the concentrations, and a fixed-point method to determine the potentials and intensity for the given concentrations. For a given final time t_{end}, we consider a uniform subdivision

$$t^n = n\Delta t,\ n = 0, \cdots, N,$$

with $\Delta t = t_{end}/N$. In each time step the variables then are

$$W^n = \left(c_{\mathrm{ia}}{}^n, G_{\mathrm{a}}{}^n, C_{\mathrm{Li}}{}^n, c_{\mathrm{ic}}{}^n, G_{\mathrm{c}}{}^n, C_{0\mathrm{x}}{}^n, \phi_a^n, \phi_c^n, I_{\mathrm{a}}{}^n, I_{\mathrm{c}}{}^n\right).$$

5.3.1 ordinary differential equations discretisation

On the anode side, the ordinary differential equations (ODEs) read (see equations (5.40), (5.42))

$$\begin{aligned}
\frac{dc_{\mathrm{ia}}}{dt} &= +\frac{1-t^+}{\varepsilon_{\mathrm{a}}\, F} s_{\mathrm{a}} F_{\mathrm{a}}(c_{\mathrm{ia}}, C_{\mathrm{Li}}) S_{\mathrm{a}}(\phi_{\mathrm{a}}) - \frac{A_{\mathrm{a}} + A_{\mathrm{c}}}{2A_{\mathrm{a}}} \frac{D_{\mathrm{s}}}{L_{\mathrm{a}}\, L_{\mathrm{s}}} (c_{\mathrm{ia}} - c_{\mathrm{ic}}) \\
\frac{dC_{\mathrm{Li}}}{dt} &= -\frac{1-t^+}{\varepsilon_{\mathrm{a}}\, F} s_{\mathrm{a}} F_{\mathrm{a}}(c_{\mathrm{ia}}, C_{\mathrm{Li}}) S_{\mathrm{a}}(\phi_{\mathrm{a}})
\end{aligned}$$

We take advantage of the variable separation of $G_{\mathrm{a}}(C_{\mathrm{Li}}, c_{\mathrm{ia}}, \phi_{\mathrm{a}}) = F_{\mathrm{a}}(C_{\mathrm{Li}}, c_{\mathrm{ia}}) S_{\mathrm{a}}(\phi_{\mathrm{a}})$ by freezing S_{a} at the time t^n to compute ${c_{\mathrm{ia}}}^{n+1}$ and ${C_{\mathrm{Li}}}^{n+1}$ of the modified differential equations.

$$\frac{dc_{\mathrm{ia}}}{dt} = +{R_{\mathrm{a}}}^n\, C_{\mathrm{Li}max} \left(\frac{(C_{\mathrm{Li}max} - C_{\mathrm{Li}}) C_{\mathrm{Li}}}{C_{\mathrm{Li}max}^2} \right)^{\alpha_{\mathrm{a}}} - \frac{A_{\mathrm{a}} + A_{\mathrm{c}}}{2A_{\mathrm{a}}} \frac{D_{\mathrm{s}}}{L_{\mathrm{a}}\, L_{\mathrm{s}}} (c_{\mathrm{ia}} - c_{\mathrm{ic}}) \tag{5.44}$$

$$\frac{dC_{\mathrm{Li}}}{dt} = -{R_{\mathrm{a}}}^n\, C_{\mathrm{Li}max} \left(\frac{(C_{\mathrm{Li}max} - C_{\mathrm{Li}}) C_{\mathrm{Li}}}{C_{\mathrm{Li}max}^2} \right)^{\alpha_{\mathrm{a}}} \tag{5.45}$$

with ${R_{\mathrm{a}}}^n = S_{\mathrm{a}}({\phi_{\mathrm{a}}}^n) \dfrac{s_{\mathrm{a}} k_{\mathrm{a}0} (1 - t^+)}{\varepsilon_{\mathrm{a}}}$.

The same mathematical framework and approach was used for $C_{0\mathrm{x}}$ and c_{ic}.

One first draw of the numerical approximation was, given ${c_{\mathrm{ia}}}^n, {G_{\mathrm{a}}}^n, {C_{\mathrm{Li}}}^n, {c_{\mathrm{ic}}}^n, {G_{\mathrm{c}}}^n, {C_{0\mathrm{x}}}^n, \phi_a^n, \phi_c^n, {I_{\mathrm{a}}}^n, {I_{\mathrm{c}}}^n$, we determine for $t = t^{n+1}$:

1. electromotive force e^{n+1} and R_{ext} to decide the charge and discharge cycles,
2. ${C_{\mathrm{Li}}}^{n+1}$, ${C_{0\mathrm{x}}}^{n+1}$, and ${c_{\mathrm{ia}}}^{n+1}, {c_{\mathrm{ic}}}^{n+1}$,
3. ${F_{\mathrm{a}}}^{n+1}({c_{\mathrm{ia}}}^{n+1}, {C_{\mathrm{Li}}}^{n+1})$, ${F_{\mathrm{c}}}^{n+1}({c_{\mathrm{ic}}}^{n+1}, {C_{0\mathrm{x}}}^{n+1})$
4. a fixed-point iteration, while $err < Tol$, calculate
   (a) η_{a}, η_{c}
   (b) ${S_{\mathrm{a}}}^{n+1}$, ${S_{\mathrm{c}}}^{n+1}$

(c) $G_{\mathrm{a}}{}^{n+1}$, $G_{\mathrm{c}}{}^{n+1}$

(d) I_{a}, I_{c}

(e) $\phi_{\mathrm{a}}{}^{n+1}$, $\phi_{\mathrm{c}}{}^{n+1}$

(f) $y_a = (R_{\mathrm{ext}} I_{\mathrm{a}} + e) + (\phi_{\mathrm{a}} - \phi_{\mathrm{c}})$, $y_c = (R_{\mathrm{ext}} I_{\mathrm{a}} + e^{n+1}) + (\phi_{\mathrm{a}} - \phi_{\mathrm{c}})$;

(g) $err = |y_a| + |y_c|$

$I_{\mathrm{tot}}{}^{n+1} = (I_{\mathrm{a}} + I_{\mathrm{c}})/2$;

Analysis of the critical situations

Since $C_{\mathrm{Li}} \in [0, C_{\mathrm{Li}max}]$, the critical situations arise when $C_{\mathrm{Li}}(t) \to 0$ or $C_{\mathrm{Li}}(t) \to C_{\mathrm{Li}max}$. Let us rewrite the C_{Li} differential equation as

$$\frac{d\tau}{dt} = -R_{\mathrm{a}}{}^{n} \, (1-\tau)^{\alpha_{\mathrm{a}}} \tau^{\alpha_{\mathrm{a}}}, \qquad \tau = \frac{C_{\mathrm{Li}}}{C_{\mathrm{Li}max}} \tag{5.46}$$

We consider the discharge situation ($R_{\mathrm{a}}{}^{n} > 0$) where the anode is almost depleted, that is $\tau \approx 0$ while $1 - \tau \approx 1$. Hence, the solution behaves following the simplified problem

$$\frac{d\tau}{dt} = -R_{\mathrm{a}}{}^{n} \, \tau^{\alpha_{\mathrm{a}}}. \tag{5.47}$$

Assume that the initial state at $t = t^n$ is τ^n, then one has by a simple integration using the variables separation technique:

$$\tau^{1-\alpha_{\mathrm{a}}} - (\tau^n)^{1-\alpha_{\mathrm{a}}} = -(1-\alpha_{\mathrm{a}}) R_{\mathrm{a}}{}^{n} (t - t^n). \tag{5.48}$$

We then get the analytic solution

$$\tau(t) = \left((\tau^n)^{1-\alpha_{\mathrm{a}}} - (1-\alpha_{\mathrm{a}}) R_{\mathrm{a}}{}^{n} (t - t^n) \right)^{\frac{1}{1-\alpha_{\mathrm{a}}}}. \tag{5.49}$$

Consequently for $t > t^n$, there exists a critical time $\bar{t}$ such that

$$(\tau^n)^{1-\alpha_{\mathrm{a}}} = (1-\alpha_{\mathrm{a}}) R_{\mathrm{a}}{}^{n} (\bar{t} - t^n), \tag{5.50}$$

that is, **the depletion process stops at a finite time and not asymptotically with** $t \to +\infty$. From a numerical point of view, it means that the time marching procedure has to stop when reaching $C_{\mathrm{Li}} = 0$ and $R_{\mathrm{a}} \geq 0$. The numerical procedure has to start again if $R_{\mathrm{a}} < 0$, that is when charging the battery. At the numerical level, one has to implement a mechanism that stops and restarts the numerical procedure to guarantee the physical limits of the concentrations.

Discretisation of the concentrations

To deal with this critical situation, We propose an explicit scheme with a predictor to calculate the first term of the right-hand side of (5.44) in point 2. of each time step. To this end, we define the predicted source term $P_{\mathrm{a}}{}^{\star}$ and a predicted solution $C_{\mathrm{Li}}{}^{\star}$ with

$$P_{\mathrm{a}}{}^{\star} = R_{\mathrm{a}}{}^{n}\, C_{\mathrm{Li}max}\left(\frac{(C_{\mathrm{Li}max} - C_{\mathrm{Li}}{}^{n})C_{\mathrm{Li}}{}^{n}}{C_{\mathrm{Li}max}^{2}}\right)^{\alpha_{\mathrm{a}}}, \qquad C_{\mathrm{Li}}{}^{\star} = C_{\mathrm{Li}}{}^{n} - \Delta t P_{\mathrm{a}}{}^{\star} \tag{5.51}$$

- If $C_{\mathrm{Li}}{}^{\star} \in [0, C_{\mathrm{Li}max}]$, then $P_{\mathrm{a}}{}^{n+1} = P_{\mathrm{a}}{}^{\star}$, $C_{\mathrm{Li}}{}^{n+1} = C_{\mathrm{Li}}{}^{\star}$;
- If $C_{\mathrm{Li}}{}^{\star} < 0$, then $P_{\mathrm{a}}{}^{n+1} = C_{\mathrm{Li}}{}^{n}/\Delta t$, $C_{\mathrm{Li}}{}^{n+1} = 0$;
- If $C_{\mathrm{Li}}{}^{\star} > C_{\mathrm{Li}max}$, then $P_{\mathrm{a}}{}^{n+1} = (C_{\mathrm{Li}}{}^{n} - C_{\mathrm{Li}max})/\Delta t$, $C_{\mathrm{Li}}{}^{n+1} = C_{\mathrm{Li}max}$.

From the evaluation of $P_{\mathrm{a}}{}^{n+1}$, we use the implicit scheme to evaluate $c_{\mathrm{ia}}{}^{n+1}$

$$c_{\mathrm{ia}}{}^{n+1} = \frac{c_{\mathrm{ia}}{}^{n} + \Delta t \frac{A_{\mathrm{a}}+A_{\mathrm{c}}}{2A_{\mathrm{a}}} \frac{D_{\mathrm{s}}}{L_{\mathrm{a}} L_{\mathrm{s}}} c_{\mathrm{ic}}{}^{n} + \Delta t P_{\mathrm{a}}{}^{n+1}}{1 + \Delta t \frac{A_{\mathrm{a}}+A_{\mathrm{c}}}{2A_{\mathrm{a}}} \frac{D_{\mathrm{s}}}{L_{\mathrm{a}} L_{\mathrm{s}}}}. \tag{5.52}$$

We proceed in the same way to compute $P_{\mathrm{c}}{}^{\star}$, $C_{0\mathrm{x}}{}^{\star}$ and deduce $P_{\mathrm{c}}{}^{n+1}$ and $C_{0\mathrm{x}}{}^{n+1}$ by satisfying the physical condition. Hence, we deduce $c_{\mathrm{ic}}{}^{n+1}$.

5.3.2 Reformulation of the model

The model involves a lot of stages and formulas. We propose a reformulation (that is, we are dealing with the same model) in order to highlight the different parameters involved in the model.

Discharge case

In case of a discharge,

$P_{\mathrm{a}} \geq 0$ is the reaction term (production of Li-ion in the anode) in $[mol/s]$.

$$P_{\mathrm{a}} = \frac{1 - t^{+}}{\varepsilon_{\mathrm{a}}} s_{\mathrm{a}}\, k_{\mathrm{a}0}^{+}\, C_{\mathrm{Li}max}\left(\frac{C_{\mathrm{Li}} - C_{\mathrm{Li}min}}{C_{\mathrm{Li}max}}\right)^{\alpha_{\mathrm{a}}}\left[\exp\left(\alpha_{\mathrm{a}}\frac{F\eta_{\mathrm{a}}}{2RT}\right) - \exp\left((\alpha_{\mathrm{a}} - 1)\frac{F\eta_{\mathrm{a}}}{2RT}\right)\right] \tag{5.53}$$

$$\frac{dC_{\mathrm{Li}}}{dt} = -P_{\mathrm{a}}, \qquad \frac{dc_{\mathrm{ia}}}{dt} = P_{\mathrm{a}} - \frac{A_{\mathrm{a}} + A_{\mathrm{c}}}{2A_{\mathrm{a}}}\frac{D_{\mathrm{s}}}{L_{\mathrm{a}} L_{\mathrm{s}}}(c_{\mathrm{ia}} - c_{\mathrm{ic}}) \tag{5.54}$$

Charge case

In the case of charge,

$P_{\mathrm{c}} \leq 0$ is the reaction term (production of Li-ion in the cathode) in $[mol/s]$.

$$P_{\mathrm{c}} = \frac{1 - t^{+}}{\varepsilon_{\mathrm{c}}} s_{\mathrm{c}}\, k_{\mathrm{c}0}^{-}\, c_{\mathrm{ic}}\left(\frac{C_{0\mathrm{x}max} - C_{0\mathrm{x}}}{C_{0\mathrm{x}max}}\right)^{\alpha_{\mathrm{c}}}\left[\exp\left(\alpha_{\mathrm{c}}\frac{F\eta_{\mathrm{c}}}{2RT}\right) - \exp\left((\alpha_{\mathrm{c}} - 1)\frac{F\eta_{\mathrm{c}}}{2RT}\right)\right] \tag{5.55}$$

$$\frac{dC_{0x}}{dt} = -P_c\,, \qquad \frac{dc_{ic}}{dt} = P_c + \frac{A_a + A_c}{2A_c}\frac{D_s}{L_c\,L_s}(c_{ia} - c_{ic}) \tag{5.56}$$

5.3.3 The fixed-point procedure

A problem of stability was detected for this set of equations. This required the need for a fixed point. A fixed point for a function is a numerical value at which the function's output remains constant when the function is applied. Fixed points help in determining the stability and behavior of dynamic systems. Batteries have various operating states, including charging, discharging, and resting. Fixed points help identify the equilibrium states where certain battery parameters, such as voltage and current, stabilize. These fixed points are crucial for understanding the battery's behavior under different conditions.

The introduction of a fixed point in the model for more accurate results is as follows. Given ${F_a}^n$, we define the function

$$\phi_a \to \eta_a \to G_a \to I_a = I_a(\phi_a; {F_a}^n). \tag{5.57}$$

Similarly, given F_c, we have the operator $\phi_c \to I_c(\phi_c; {F_c}^n)$.

Using the conditions $I_a = I_c = \dfrac{\phi_c - \phi_a}{R_{ext}}$, we deduce the fixed-point problem

$$\begin{pmatrix} \phi_a \\ \phi_c \end{pmatrix} = \begin{pmatrix} \phi_c \\ \phi_a \end{pmatrix} + R_{ext} \begin{pmatrix} -I_a(\phi_a; {F_a}^n) \\ +I_c(\phi_c; {F_c}^n) \end{pmatrix}, \tag{5.58}$$

we can rewrite under the form $(\phi_a, \phi_c)^t = \mathcal{F}(\phi_a, \phi_c; {F_a}^n, {F_c}^n)$.

Simple solver

We consider the sequence $({\phi_a}^{n,r}, {\phi_c}^{n,r})_r$ given by the iterative procedure,

$$({\phi_a}^{n,r+1}, {\phi_c}^{n,r+1})^t = \mathcal{F}({\phi_a}^{n,r}, {\phi_c}^{n,r}; {F_a}^n, {F_c}^n). \tag{5.59}$$

where the initial values $({\phi_a}^{n,0}, {\phi_c}^{n,0})$ are given.

Let $\nabla\mathcal{F}$ the 2×2 Jacobian matrix and λ the eigenvalues. If all $|\lambda| < 1$, the iterative procedure converges.

Remark 5.3.1: An additional fixed point was necessary in order to fixate intensity (I_{tot}) while varying resistance(R_{ext}). Thus, the intensity value was set at a target number.

Chapter 6

Results and discussion

The following chapter analyses and discusses the results obtained from the characterization techniques described in the previous chapter. The main goal was to produce thin films doped with different ceramic particles that could be employed as solid-state electrolytes, aiming for an improved interface with the electrodes and enhancing the battery performance. In the last section, the developed numerical method is tested, and submitted to different parameters. Which allowed a greater comprehension of the battery.

Results and discussion

6.1 Physical Characterization

Scanning Electron Microscopy analysis

The **surface morphology and compound distribution** of the SSE were assessed by SEM. The photomicrograph is shown in Figure 1. The main aim was to compare the membranes with and without the ceramic particles while also evaluating the ceramic distribution along the surface.

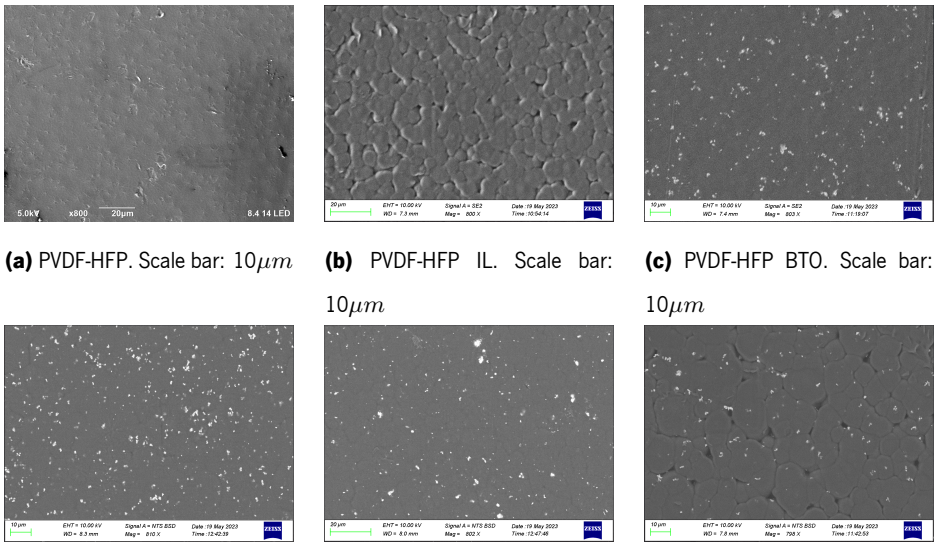

(a) PVDF-HFP. Scale bar: $10\mu m$ **(b)** PVDF-HFP IL. Scale bar: $10\mu m$ **(c)** PVDF-HFP BTO. Scale bar: $10\mu m$

(d) PVDF-HFP BST. Scale bar: $10\mu m$ **(e)** PVDF-HFP PZT. Scale bar: $10\mu m$ **(f)** PVDF-HFP IL BST. Scale bar: $10\mu m$

Figure 1: Top-view SEM images several samples (Scale bar: 10 μm). (a) PVDF-HFP. (b) PVDF-HFP IL. (c) PVDF-HFP BTO. (d) PVDF-HFP BST. (e) PVDF-HFP PZT. (f) PVDF-HFP IL BST.

We conducted the SEM analyses following conventional procedures and several images were taken at different locations of the section of the sample to get an accurate representation of the surface area that is undergoing the analysis. The reference sample in Figure 1 (a) shows a compact structure. This is due to the semicrystalline structure, the lower crystallinity is associated with a low porosity, therefore, a compact structure (X. Wang et al., 2018). The content of the β-phase in the PVDF-HFP is characterized by a more ordered and tightly packed arrangement of polymer chains, contributing to the overall compactness of the structure. Furthermore, the presence of fluorine atoms in the HFP units enhances the packing efficiency of the polymer chains, leading to a more compact arrangement.

The samples that contained ionic liquid (IL) are easier to observe with SEM, in fact, the samples without IL, were rapidly damaged by the SEM beam, which did not allow a good visualization of the specimens. The addition of IL

increased the ionic conductivity which increases the interactions between the electrons and the sample generating various signals and revealing an increased detail in images. The inclusion of IL resulted in considerable changes in the morphology of the film, derived from a chemical change in the polymeric structures, resulting from the polymer-ion interactions. This molecular interaction caused a less compact structure of the polymeric matrix, which can facilitate the impregnation of the liquid electrolyte and consequently enhance the ion mobility through the membrane.

Figure 1 (c), (d), and (e) show representative SEM images, where is observed a general dispersion of the ceramic. A good overall distribution shows that the ceramics were nicely incorporated into the polymeric matrix. After blending the different ceramics with the polymer there was no noticeable change in morphology, as the membrane maintained a compact structure. Additionally, we noticed the new presence of ceramic fillers. It appears that the membrane is well connected, and the size of the film pores was low or nonexistent (X. Wang et al., 2018).

The **complementary use of SEM-EDS** is an attempt to understand the structural and compositional complexity of the samples. The morphology and surface composition of the SSE membranes were characterized by scanning electron microscopy (SEM) and energy dispersive analysis of X-rays (EDX) to combine the structure-property relationship between electrical and structural properties. EDS mapping is shown in Figure 2.

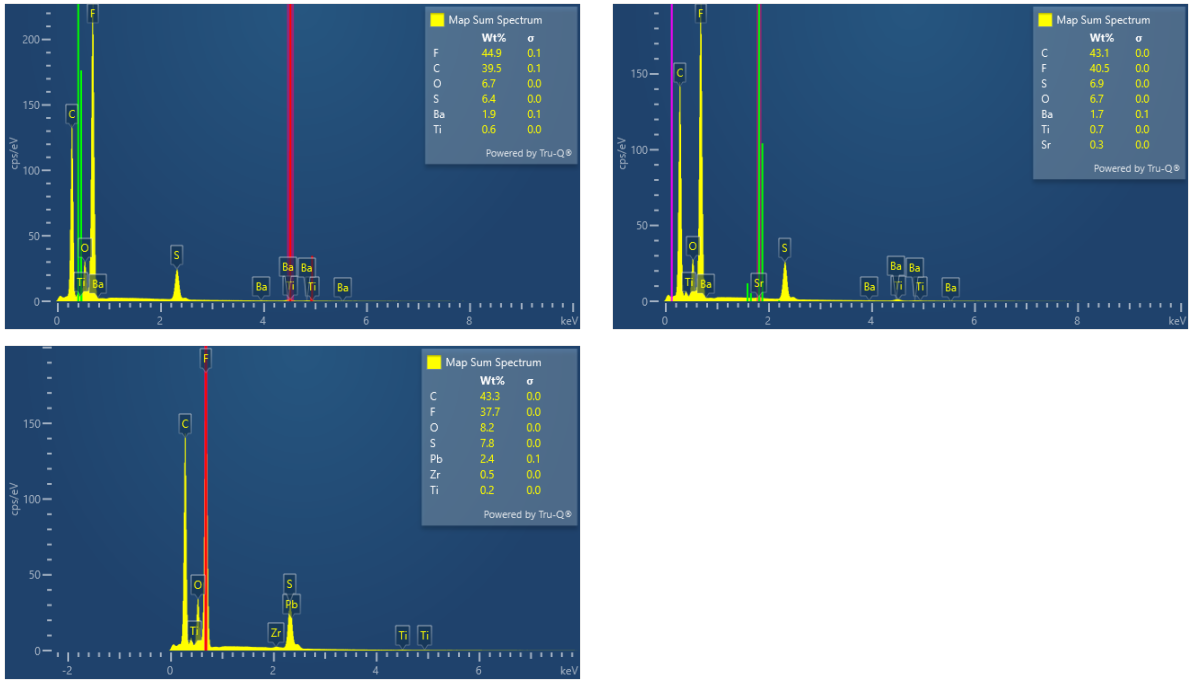

Figure 2: Typical EDS spectra of (a) PVDF-HFP IL BTO film; (b) PVDF-HFP IL BST film; (c) PVDF-HFP IL PZT film

The EDS results revealed the presence of the ceramic particles in the polymeric matrix, shown by the different elements signal, as clear peaks of the different composites are seen in the spectrum over a large area.

Fourier Transform Infrared Spectroscopy with Attenuated Total Reflection

In order to understand the different **organic polymeric or inorganic components**, we employed the FTIR analysis to observe the corresponding chemical properties. FTIR is a technique that relies on the absorption of electromagnetic radiation in the IR region by the covalent bonds present in the different compounds in question for analysis. For the determination of the functional groups in the SSE samples the IR is active on molecules with dipole moments. Figure 3 illustrates the results from the FTIR analysis on the PVDF-HFP and PVDF-HFP IL samples.

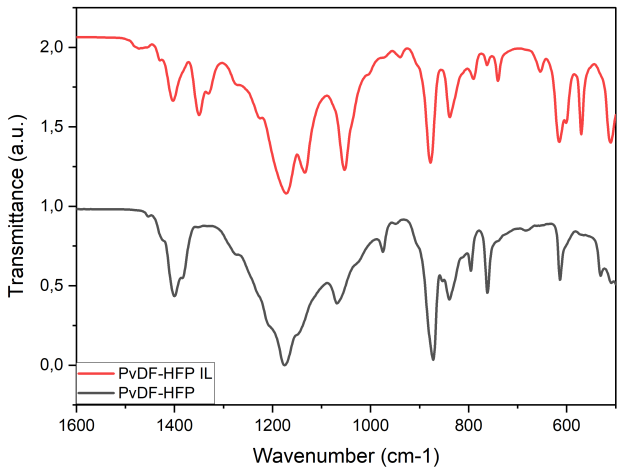

Figure 3: FTIR-ATR spectra of PVDF-HFP (black) vs PVDF-HFP IL (red).

For the SSE samples and their components, we expected to observe a spectrum that is characteristic of the polymeric matrix, since it is the only component that absorbs energy. PVDF-HFP spectra will differentiate different crystalline phases that correspond to different peaks of transmittance. Phase I (or β phase)has a zig-zag (all trans) conformation and it results when the polymer is strained, stretched, or quenched. Phase II, also known as α-phase, adopts a non-polar trans-gauche-trans-gauche' (TGTG') conformation and is the most prevalent phase under typical conditions. Phase III, referred to as γ-phase, features an intermediate polar TTTGTTTG' conformation and emerges when the polymer undergoes moderate stress. Lastly, Phase IV, denoted as δ-phase, is only observed under specific crystallization conditions involving particular temperatures and pressures(Aravindan, Vickraman, & Kumar, 2008).

Phase I is present, as the two peaks around 530 and 614 cm^{-1}. Peaks in the region of 840 and 880 cm^{-1} are a trace of phase III. The region between 700–1000 cm^{-1} implies the presence of both phases II and III in the neat copolymer. Phase IV is not present since the tests were performed at room temperature, inhibiting its formation(Abbrent et al., 2001). The vibrational waves at 761, 795, and 614 cm^{-1} correspond to the crystalline nature of PVDF-HFP. The bending vibrations of CF2 groups can be observed around 810-850 cm^{-1}. The band at 1069, and 1175 cm^{-1} corresponds to the symmetrical stretching mode of CF_2. PVDF-HFP contains CF2 groups,

which exhibit stretching vibrations around 1200-1230 cm^{-1}. The band at 1400 cm^{-1} is associated with the C-F stretching(Cai, Lei, Sun, & Lin, 2017)(Hasegawa, Takahashi, Chatani, & Tadokoro, 1972).

Upon the incorporation of IL, there were no noted changes in the PVDF-HFP chemical structure. The main differences are the vibrational waves at 1347, 1132, 739, 652, and 570 cm^{-1}. The absorption bands of the IL anion $[TFSI]^-$ are identified as the absorption band at 739 cm^{-1} derivative of the cis $[TFSI]^-$ conformation and the asymmetric and symmetric stretching vibration modes characteristic of the SO_2 group at 1132 and 1347 cm^{-1} (Barbosa et al., 2021). When the ceramic particles were added and no significant change in the spectra was registered, the peaks were represented in the same region, illustrated in Figure 4.

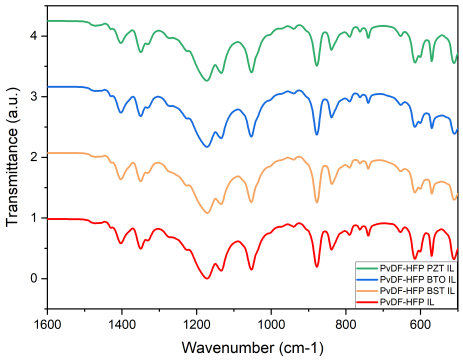

(a) Comparison PVDF-HFP with and without ceramics.

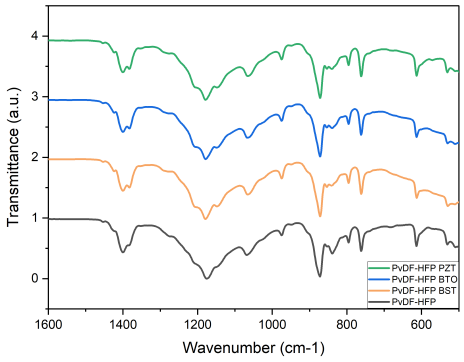

(b) Comparison PVDF-HFP/IL with and without ceramics.

Figure 4: FTIR-ATR spectra of PVDF-HFP/ceramics composite films.

X-ray Diffraction

We adopted XRD as the technique to investigate the **crystal structure** of the studied samples. Figures 5 and 6 represent the XRD patterns of the samples, in a range of 10-85° of 2θ. Two diffractogram panels are employed to visualize the database values and the corresponding peaks of the studied samples.

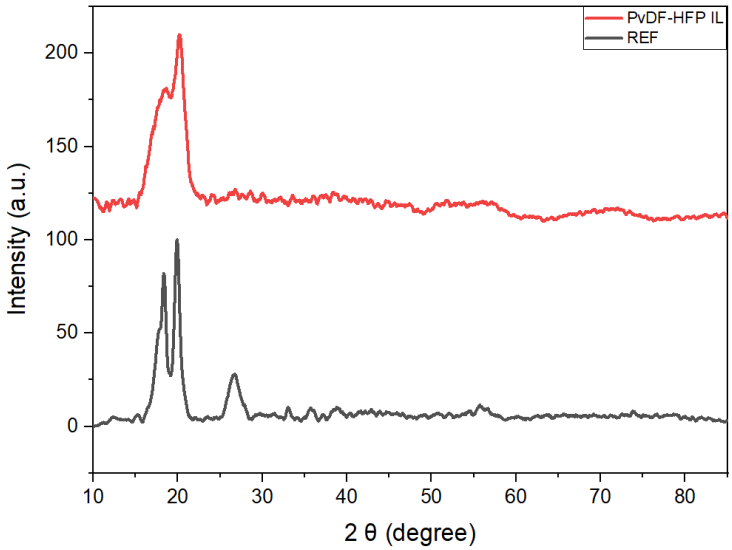

Figure 5: XRD spectra of PVDF-HFP and PVDF-HFP IL samples (black and red line, respectively).

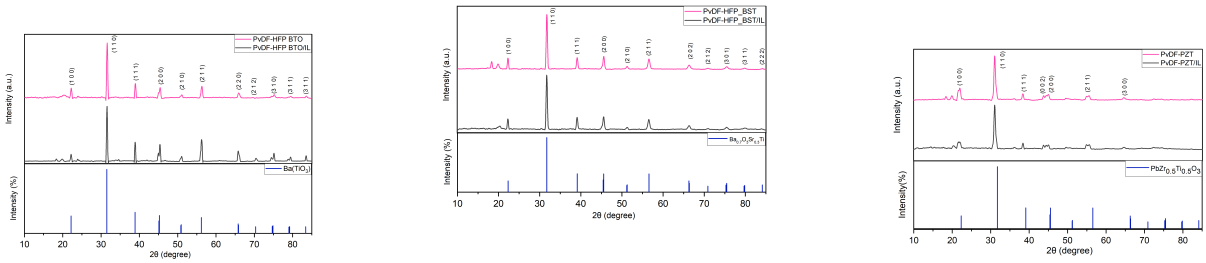

(a) Comparison between PVDF-HFP BTO and HFP-HFP BTO IL.

(b) Comparison between PVDF-HFP BST and HFP-HFP BST IL.

(c) Comparison between PVDF-HFP PZT and HFP-HFP PZT IL.

Figure 6: XRD spectra of PVDF-HFP/ceramics samples with the comparison with reviewed literature.

In Figure 5 no crystalline peak is shown for the pure PVDF-HFP and PVDF-HFP/IL films, but wide peak-like intensity outlines in the 2 ranges of 10°–20° and 20°–30° may be seen, indicating the film's amorphous structure. Partial crystallization of PVDF units present in the complexes, giving an overall semi-crystalline nature of the polymeric matrix, and the presence of broad hump in the complexes confirms the partial amorphous nature of these samples(Tafur, Santos, & Fernández Romero, 2015). On the other hand, the properties of the different samples containing ceramic particles (BTO, BST, and PZT) are dominant in the XRD spectra.

Concerning Figure 6 (a) the sample is composed of the BTO. The XRD phase identification shows that it matches a tetragonal cristal, spacegroup P4mm. In the context of nanostructured BTO, it becomes challenging to confidently identify its properties. This uncertainty arises from the broadening of characteristic tetragonal line patterns due to the small size of crystallites. As a consequence, the distinctive tetragonal line splittings that would typically be observed in larger samples may not be readily discernible in nano-BTO specimens. This phenomenon is a result of the diminutive crystallite dimensions, making it difficult to ascertain the material's structural characteristics using traditional analytical techniques (Pasuk et al., 2021).

The symmetry of the crystal lattice is tetragonal; therefore, even if the peaks are not split, the peak profiles could be modified due to the overlapping of several lines of different intensities. This can be corroborated by the diffractogram, which exhibited high-intensity diffraction peaks at $2\theta = 22.17°$, $31.51°$, $38.87°$, $45.22°$, $50.92°$, $56.16°$, $65.88°$, $70.35°$, $74.86°$, $79.21°$, $83.43°$, that are ascribed to the following crystalline planes (100), (110), (111), (200), (210), (211), (220), (212), (310), (311) and (222), respectively.

In Figure 6 (b) the presence of BST demonstrates the crystalline structure of the sample and validates the presence of a perovskite tetragonal structure of the P4mm space group, suggesting an efficient dispersion of Sr and Sn into BT lattice to form a solid solution(Khardazi et al., 2022). All the peaks are represented in Figure 6 (b), which can be identified with the succeeding 2θ values $2\theta = 22.31°$, $31.73°$, $39.14°$, $45.54°$, $51.26°$, $56.57°$, $66.28°$, $70.89°$, $75.47°$, $79.84°$, $84.11°$, that were attributed to the crystalline planes listed as follows (100), (110), (111), (200), (210), (211), (202), (212), (301), (311), and (222), respectively. The diagram demonstrates that the (200) peak is more broad when compared to the (111) peak. This can be an indication of the existence of a polar structure (Mao et al., 2014).

Figure 6 (c) reveals triplet peaks around $2\theta = 45°$ indicating that the PZT piezoelectric particles consist of a mixture of tetragonal and rhombohedral phases(Boutarfaia, 2000). The diffractogram displays the different intensity diffraction peaks at $2\theta = 22.12°$, $31.35°$, $38.31°$, $43.74°$, $44.47°$, $44.92°$, $55.°$, and $67.94°$. The crystal planes that correspond to the measured angles are as follows (100), (110), (111), (002), (200), (200), (211), and (003), respectively. The peaks at (100), (110), (200) and (002) planes correspond to the crystallization in the tetragonal phase. On the other hand, the rhombohedral phase is present in the (111) plane (Z. J. Wang, Aoki, Yan, Kokawa, & Maeda, 2004). The angles that correspond to the planes (003) and several minor peaks that are not

identified in the $2\theta = 70°$ - $80°$ range, are characteristic of very small nanocrystallines, as these produce very weak signals.

By analyzing the shape of XRD peaks, we determined the average crystallite size of the different ceramic powders using Debye Scherrer's formula. The summations presented in 6.1 are the calculations of the crystallinity for each sample that was obtained from the width of the diffraction peak, in radians, at a height halfway between the background and the peak maximum. The different values of crystalline peaks from the several samples were made by fitting in the software OriginPro2023b. Therefore, the degree of crystallinity has an experimental error associated.

Table 6.1: XRD parameters for the different samples. FWHM and crystallite size.

Samples	FWHM (degree)	Average crystallite size (nm)
BTO	0.476	24.28
BST	0.623	18.25
PZT	0.770	14.98

The crystallite size of all samples falls into the range dictated by the literature. Where BTO has a crystallite size of around $18 - 24nm$ (Pasuk et al., 2021), BST around $18nm$ (Yustanti, Hafizah, & Manaf, 2018) and PZT between $10 - 15nm$ (Banerjee & Bose, 2004).

Differential Scanning Calorimetry

DSC analysis was performed, between 0 and 200 °C, to characterize the melting behavior of the materials study. Only the endothermal process was studied. The endothermic peaks, ascribed to the melting points, are shown in Figure 7 and Figure 8. Table 6.2 summarizes the melting points, that were attained from the DSC thermograms. These parameters are due to the melting of the crystalline phases present in each analyzed sample.

It should be noted that the glass transition temperature (T_g) of PVDF-HFP is around –35 °C, as mentioned in the literature (Malmonge, Malmonge, & Sakamoto, 2003). However, because the tests were performed under temperature conditions above that, it is not noticeable on the thermograms (V. K. Singh, Singh, et al., 2015). There is a clear connection between the broad peaks and the sample structural characteristics. The sample has an amorphous structure when the peak is broader, such as in the case in question (TIP, n.d.). This peak is a result of the absorption of heat, and the lower the crystallization the broader the peak will be.(TIP, n.d.) All the samples demonstrate an endothermic peak or melting temperature (T_m) between 130 and 150 °C, which is attributed to the melting process. In table 6.2 below it is possible to discretize the different peak values for each sample. Noticeably there is a significant change in the T_m peak when the polymeric matrix contains IL. The melting point shifts towards a lower temperature, which may be attributed to the crystallinity change and local influence of the polymer conformation, that is due to the IL complexation with the polymer backbone, the addition of the

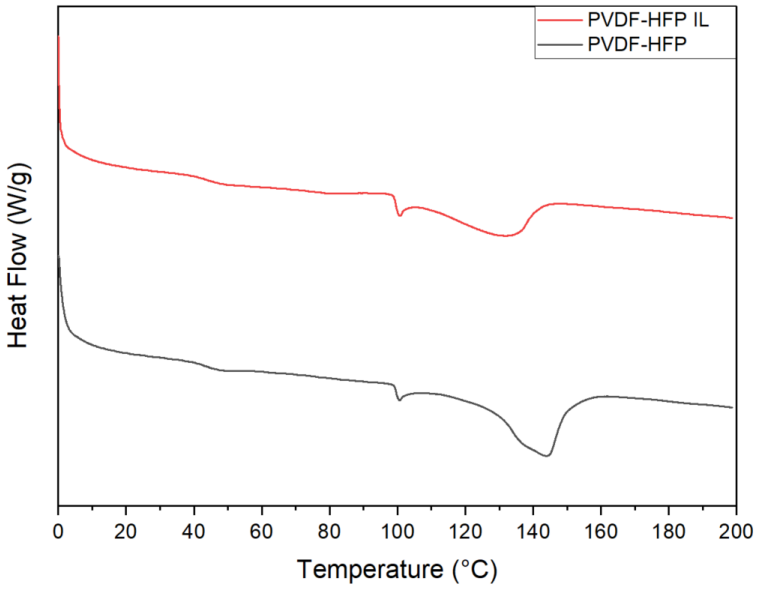

Figure 7: DSC thermograms of the film samples without ceramics. DSC curves of PVDF-HFP and PVDF-HFP/IL.

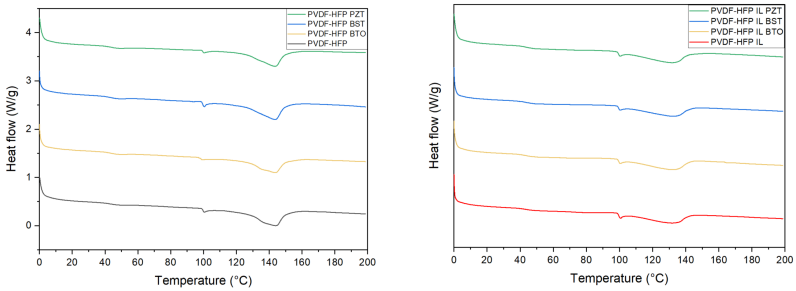

(a) Thermograms of PVDF-HFP, PVDF-HFP/BTO, PVDF-HFP/BST, and PVDF-HFP/PZT.

(b) Thermograms of PVDF-HFP IL, PVDF-HFP/BTO IL, PVDF-HFP/BST IL, and PVDF-HFP/PZT IL.

Figure 8: DSC thermograms of the composite samples.

IL also endures a plasticization effect. This indicates that there is a decreasing number of tie molecules in the amorphous phase, and the decreased melting temperature results in a decrease in crystallinity (Laxmayyaguddi et al., 2018)(L. Wu et al., 2014). The addition of ceramic did not input any significant change in the results.

Employing the DSC software it was possible to attain the integration of the melting peak of all samples. The unit of the integrated area is J/g and represents the enthalpy of fusion (ΔH_m). This parameter is also shown in Table 6.2. Bearing in mind the calculated value, the percentage of crystallinity (χ_c%) can be easily computed by the following equation

$$\chi(\%) = \frac{\Delta H_m}{\Delta H_m^0} \times 100 \tag{6.1}$$

Where ΔH_m represents the alteration in enthalpy during the process of melting, and ΔH_m^0 signifies the heat of fusion of pure (PVDF), with a specific value of 104.7 J/g under the assumption that the material is entirely

Table 6.2: Estimated values of T_m, ΔH_m and χ_c% for the peaks of the crystalline fusion of studied samples for the first heating

Samples	T_m (°C)	ΔH_m (J/g)	$\chi_c(\%)$
PVDF-HFP	143.93	17.232	16.45
PVDF-HFP BTO	143.90	14.080	13.45
PVDF-HFP BST	143.98	13.991	13.36
PVDF-HFP PZT	14.64	14.173	13.54
PVDF-HFP IL	132.08	9.3326	8.908
PVDF-HFP IL BTO	132.54	8.5031	8.121
PVDF-HFP IL BST	133.15	7.3352	7.961
PVDF-HFP IL PZT	131.88	7.4690	7.134

crystalline.

Additionally, on all thermograms, it is visible a small peak (with ΔH_m between 0.2 and 1 J/g) around 100 °C. This is not characteristic of a pure sample, so this is associated with an impurity. This peak occurs at 100 °C, the same characteristic temperature as the ebullition point of water. These peaks can be identified as a distinct weight loss and, a typical curve of drying (the desorption of adsorbed moisture).

Thermogravimetric Analysis

We **monitored the mass** of the various substances as a **function of temperature** as they were subjected to a temperature program between 20-800 °C in a controlled nitrogen atmosphere. Figure 9 depicts the TGA results of the PVDF-HFP and PVDF-HFP/IL SSE samples while Figure 10 portrays the comparison between the samples that contain ceramic powders.

On the PVDF-HFP thermogram, the pure polymer SSE starts to decompose at about 460°C, which is congruent with good thermal stability. The decomposition products are gaseous, as no weight was recorded after the decomposition. With the high temperature chemical bonds within the polymer backbone start to break. This results in chain scission, where the long polymer chains are cleaved into shorter fragments. During degradation, various gaseous byproducts are released. These can include hydrogen fluoride (HF), carbon fluoride compounds, and other volatile products. The release of HF is a notable characteristic of PVDF-based materials and can contribute to the thermal degradation process (Han et al., 2016)(GSaiz, Lopes, Barker, de Luis, & Arriortua, 2018). There is no end product because all product was degraded in this procedure.

PVDF-HFP/IL composite is only stable up to around 445°C. The single-step decomposition behavior in the curves indicates that the PVDF-HFP and the ionic liquid decompose at a similar temperature. Nevertheless, IL starts to

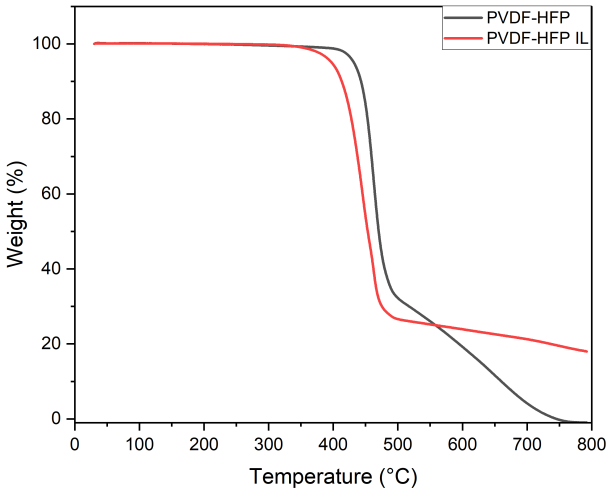

Figure 9: TGA thermograms of the film samples without ceramics. TGA curves of PVDF-HFP and PVDF-HFP/IL.

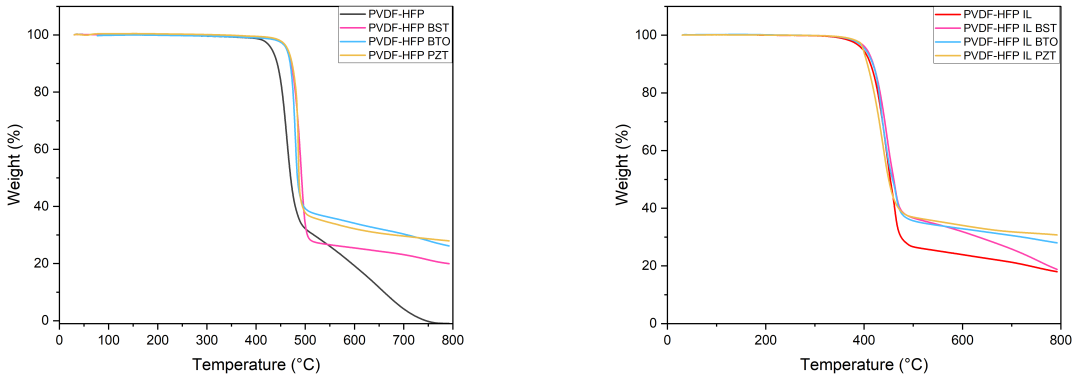

(a) PVDF-HFP ceramics SSE samples and PVDF-HFP.

(b) PVDF-HFP IL ceramics and PVDF-HFP IL.

Figure 10: TGA thermograms of the film samples with ceramics compared with the plain PVDF-HFP and PVDF-HFP IL.

degrade at a lower temperature, undergoing a decomposition stage, leading to the release of volatile components(GSaiz et al., 2018). At the end of the procedure, the remaining wt% is around 20% and can be a combination of carbonaceous material, fluorine-containing compounds, and some other organic residues. But overall the thermal stability of the SSE is also satisfactory.

The results of PVDF-HFP/ceramics showed that the SSE membrane thermal degradation temperature increased slightly to around 480 °C, which leads to the conclusion that it has enhanced thermal stability. The additional wt% at the end temperature is related to both, the ceramic powders and possibly includes partially decomposed polymer fragments, because the ceramics wt% in the membrane was around 16% and the end product is somewhat higher. This also indicates that the doping of the SSE membranes encourages greater stability of the polymeric matrix (PVDF-HFP), as the end residue can be partially preserved PVDF-HFP backbone, that could be conserved by

the ceramic content.

On the other hand samples with PVDF-HFP/IL/ceramics show similar behavior to the PVDF-HFP/IL SSE membrane, only the end product varies with different residual masses that possibly include partially decomposed polymer fragments, inorganic components from the IL, and the ceramic fillers that do not suffer decomposition. Additionally, note that the BST ceramic filler does not appear to have such an effective stabilize effect on the polymeric matrix when compared with the BTO and PZT, due to a mass shift to lower values when compared to the other fillers.

6.2 Electrochemical Characterization

6.2.1 Electrochemical impedance spectroscopy (EIS)

High ionic conductivity is a crucial property to the proper functioning of a solid-state battery. In order to understand the different conductivity value changes between cells with and without IL and ceramics, we measured the **EIS at room temperature**. The output is a Nyquist plot. It typically displays the impedance data in a complex plane, with the real component (resistance) on the horizontal axis and the imaginary component (reactance) on the vertical axis. The resulting plot often forms a curve, which can have various shapes and features. Figure 11 shows the results from all synthesized SSE samples.

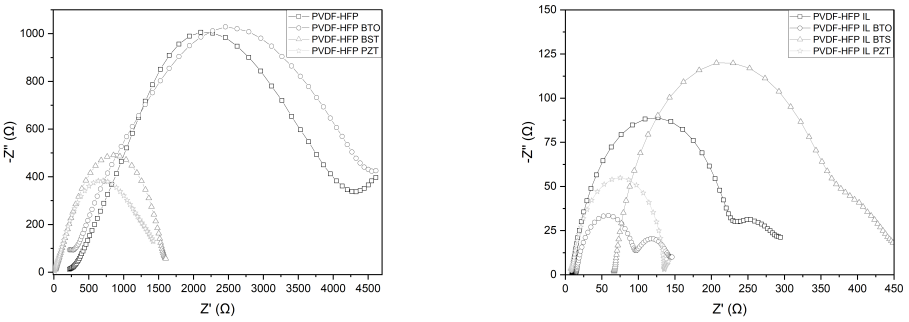

(a) PVDF-HFP Ceramics SSE samples. Impedance measurements at room temperature.

(b) PVDF-HFP Ceramics IL SSE samples. Impedance measurements at room temperature

Figure 11: Impedance measurements at room temperature. (a) PVDF-HFP Ceramics SSE samples. (b) PVDF-HFP Ceramics IL SSE samples. Impedance measurements at room temperature.

When comparing the impedance results (see table 6.3) with the literature, the values that we obtained (from $10^{-7} - 10^{-5}$S/cm) are inserted into the expected range of $10^{-8} - 10^{-5}$S/cm(H. Yang & Wu, 2022). The cells that contain IL, namely PVDF-HFP/IL, demonstrate an enhancement in the gross ionic conductivity of the material (increased from (4.60×10^{-7} to 6.68×10^{-6}S/cm). This improvement helps to reduce resistance, which can translate into better charge and discharge rates in solid-state batteries (Yusuf, Yahya, & Arof, 2017). The enhanced conductivity properties in SSE samples containing IL can be explained by the ionic composition of IL with large organic cations

and small inorganic or organic anions. These ions can introduce charge carriers into the material, increasing its ionic conductivity (Tian et al., 2019). Another interesting characteristic is the IL's ability to create additional ion transport pathways within the solid electrolyte material. This is because ILs can form interconnected channels or domains within the solid matrix, allowing ions to move more freely (Yao et al., 2019). Additionally, the higher ionic conductivity ameliorated electrochemical performance and lower impedance means reduced internal resistance, which, in turn, can result in higher energy efficiency and better overall performance. Concerning the addition of ceramics to the plain PVDF-HFP polymeric sample (4.60×10^{-7}S/cm), there was a slight increase in ionic conductivity in the samples PVDF-HFP doped with BST and PZT (1.23×10^{-6} and 1.38×10^{-6}S/cm, respectively), this can be attributed to the effect of the ceramic in the polymeric matrix. Overall, higher cell impedance was found on the cells that did not contain IL in their composition, the calculated parameters can be found in Table 6.3.

Once again the addition of the ceramics to the PVDF-HFP/IL, namely the samples PVDF-HFP doped with BTO and PZT (1.34×10^{-5} and 1.45×10^{-5}S/cm, respectively), this can be attributed to the effect of the ceramic interactions within the polymeric matrix.

Electrochemical impedance spectroscopy with temperature was a technique that allowed the understanding of the variation of conductivity as a function of temperature associated with all samples targeted in this study. The temperature dependency of the conductivity of the SSE samples is shown in Figure 12. From the Arrhenius plots the activation energy was calculated. The parameters can be found in Table 6.3.

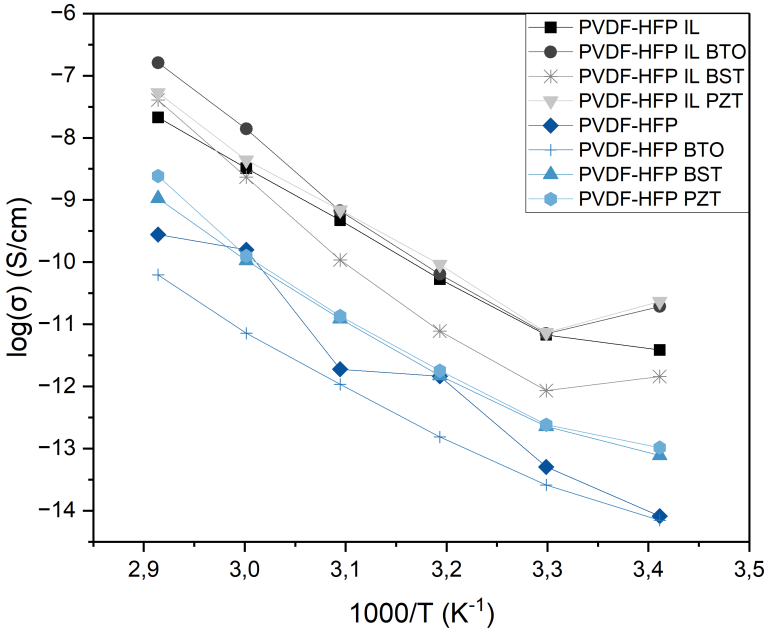

Figure 12: temperature dependence of the SSE samples. PVDF-HFP IL (black square), PVDF-HFP IL BTO (grey circle), PVDF-HFP IL BST (grey star), PVDF-HFP IL PZT (grey inverted triangle), PVDF-HFP (dark blue diamond), PVDF-HFP BTO (blue cross), PVDF-HFP BST (blue triangle), PVDF-HFP PZT (light blue hexagon);

Table 6.3: Calculation of the parameters of ionic conductivity and activation energy for each sample. Values of the Lithium Transfer number.

Sample	Ionic Conductivity (σ) (S/cm) - at 20°C	Activation Energy (E_a) (eV)	Lithium transfer number (t_{Li}^{+})
PVDF-HFP	4.60×10^{-7}	0.853	-
PVDF-HFP BTO	4.31×10^{-7}	0.689	-
PVDF-HFP BST	1.23×10^{-6}	0.729	-
PVDF-HFP PZT	1.38×10^{-6}	0.759	-
PVDF-HFP IL	6.68×10^{-6}	0.682	0.998
PVDF-HFP IL BTO	1.34×10^{-5}	0.746	0.979
PVDF-HFP IL BST	4.36×10^{-6}	0.824	0.907
PVDF-HFP IL PZT	1.45×10^{-5}	0.636	0.867

The sample PVDF-HFP shows an irregular conductivity decrease as temperature drops, in this case, the polymeric structure is more unstable at higher temperatures. When the SSE has ceramics shows better stability, which can be ascribed to the fillers' presence.

The conductivities of the samples increase as the temperature rises in one (for samples with PVDF-HFP and ceramics) or two (for samples with IL) distinct steps. These results indicate that the samples with IL exhibit different phases at different temperatures, namely at room temperature when compared to the data from when there was a temperature input. In these phases, the Li^{+} conduction activation energy can vary with the molecular arrangement. At higher temperatures ($\geq 70°C$), when PVDF-HFP melts, the polymer chain mobility is naturally higher, and the influence of the fillers on conductivity, regardless of type, is small, and all slopes of the log conductivity vs. reciprocal temperature have similar magnitude (Patla, Ray, Karmakar, Das, & Tarafdar, 2019) (Gebreyesus, Purushotham, & Kumar, 2016).

For the purpose of determining the fraction of total ionic current carried by lithium ions within the solid electrolyte chronoamperometry (CA) was conducted (Figure 13).

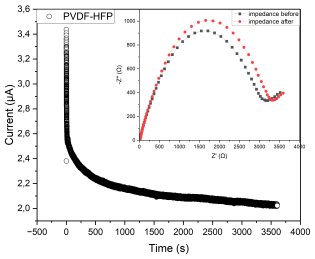

(a) CA measurement for PVDF-HFP

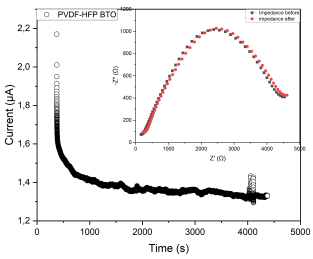

(b) CA measurement for PVDF-HFP/BTO

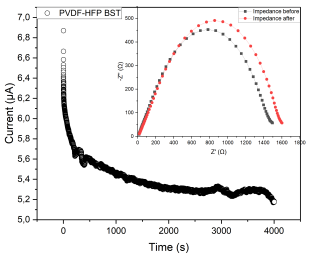

(c) CA measurement for PVDF-HFP/BST

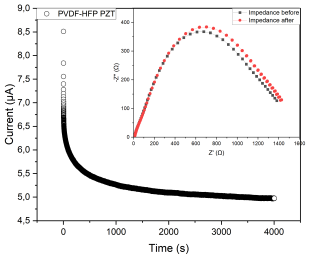

(d) CA measurement for PVDF-HFP/PZT

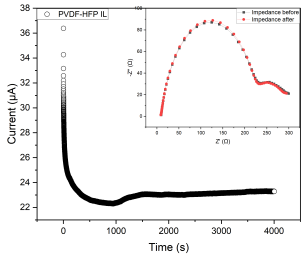

(e) CA measurement for PVDF-HFP/IL

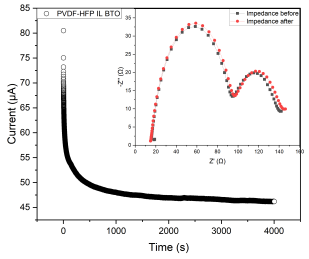

(f) CA measurement for PVDF-HFP/IL/BTO

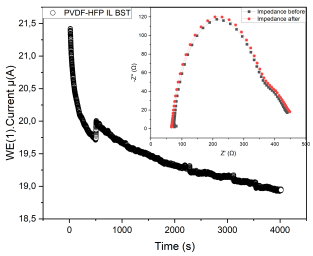

(g) CA measurement for PVDF-HFP/IL/BST

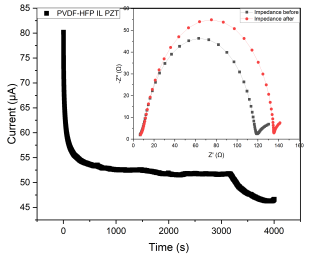

(h) CA measurement for PVDF-HFP/IL/PZT

Figure 13: Chronoamperometry measurements for all samples with both impedance measurements (before and after polarization, and the chronoamperometry typical curve.

As represented in Figure 13, the interfacial resistance of SSE membranes increases in all samples after polarization. Given the values of steady-state current (I_{ss})and from the initial current (I_0), the lithium transfer number (t_{Li+}) was calculated. All samples show similar t_{Li+} values around 0.9 (see Table 6.3). This number is generally higher than what is found in literature - around 0.3 (Liu, Zhang, Wu, & Xiang, 2017) (Zhu et al., 2022) - deducing that the compounds that we synthesized have enhanced characteristics when compared to the literature. The transference

number (close to 1) is desirable in solid electrolytes because it indicates that a significant portion of the ionic current is carried by lithium ions. This leads to improved battery efficiency and faster charging/discharging rates. This value varies slightly because it depends on the fillers used in this work.

6.2.2 Battery Charge and Discharge

In order to assess the **electrochemical performance** of the different SSE films, LFP /SSE/ Li half-cells were tested by **galvanostatic cycling**. Firstly the Battery Cycle Life Testing was analyzed for all the SSE samples containing IL. After the first formation cycle at C/15, the cell is charged at C/10 (1C= 170mAh/g) and discharged at the same C-rate, at a 2.5-4.2V range. Figure 14 displays the attained results. All tests were performed at room temperature.

When we analyzed the behavior of the cell containing PVDF-HFP/IL SSE this shows that the SSE is stable towards the electrode materials. In the cycling test, the cell has an initial capacity of 147.2 mAh/g at C/15 for the first cycle. After the formation cycle, the C-rate was increased to C/10, the capacity dropped to 121.3 mAh/g after 100 cycles, and the capacity retention was around 82%. The capacity of this cell is near the theoretical value (170 mAh/g), around 20% lower. This result further testifies that stable cycling with lithium metal and LFP cathode could be achieved with this composite electrolyte.

When the cells with the ceramic fillers were cycled they showed improved results in comparison with the sample only with IL. The formation cycle for the samples PVDF-HFP/IL/BTO and PVDF-HFP/IL/BST at C/15 reveals an initial capacity of 148.2 and 153 mAh/g, respectively. After 100 cycles at a C-rate of C/10, the capacity remained at 139.1 and 140.3 mAh/g, correspondingly, and the capacity retention was above 90%. Moreover, the addition of the ceramic fillers benefits power capability. These results are corroborated by the ionic conductivity values, as the conductivity values are all similar (6.68×10^{-6} S/cm for PVDF-HFP/IL, 1.34×10^{-5} S/cm , for PVDF-HFP/IL/BTO, and 4.36×10^{-6} S/cm for PVDF-HFP/IL/BST, contributing to the fact that the performance is comparable. This method opens a new approach to optimize ion conduction in composite solid electrolytes for solid-state batteries.

The difference in the performance of the cells can be attributed to the difference in cell resistances which is the sum of the electrolyte, interface layer, and charge transfer resistance. Overall the cells with the ceramic powders exhibit much better capacity retention.

From the last set of data (Figure 14 (g) and (h)), we observed that the SSE doped with PZT is not stable, as is not able to complete the cycling after the first life cycles. The cell suffers from severe capacity fading that results in cell failure at around the fourth cycle. This is explained by its physical properties, the PZT particle lacks the necessary high ionic conductivity that is required for ion transport in SSE, from literature, at room temperature the ceramic has an ionic conductivity in the order of 10^{-15} (Boukamp, Pham, Blank, & Bouwmeester, 2004). These membranes need to facilitate rapid ion movement to ensure efficient energy storage and discharge. On the other hand, from this work's discoveries, there is a clear enhancement in the ionic conductivity in the PVDF-HFP/PZT blend (from (4.60×10^{-7} to 1.38×10^{-6} S/cm^{-1}) this suggests that there is a positive effect of the PZT in the polymeric matrix. Yet, when we perform galvanostatic testing these cells seem to fail. An explanation can be the limited durability when this compound is subjected to constant mechanical stress or vibration. In a battery, that may experience mechanical stress during the time of use. One other reason for this malfunctioning is low chemical compatibility between the different materials in its interphase (the electrode materials). PZT may not fulfill all the requirements needed to be a successful pairing with the other electrode materials in use, potentially leading to their degradation and reduced performance (Soroushian, Nassar, & Balachandra, 2013) (J. Kang et al., 2022).

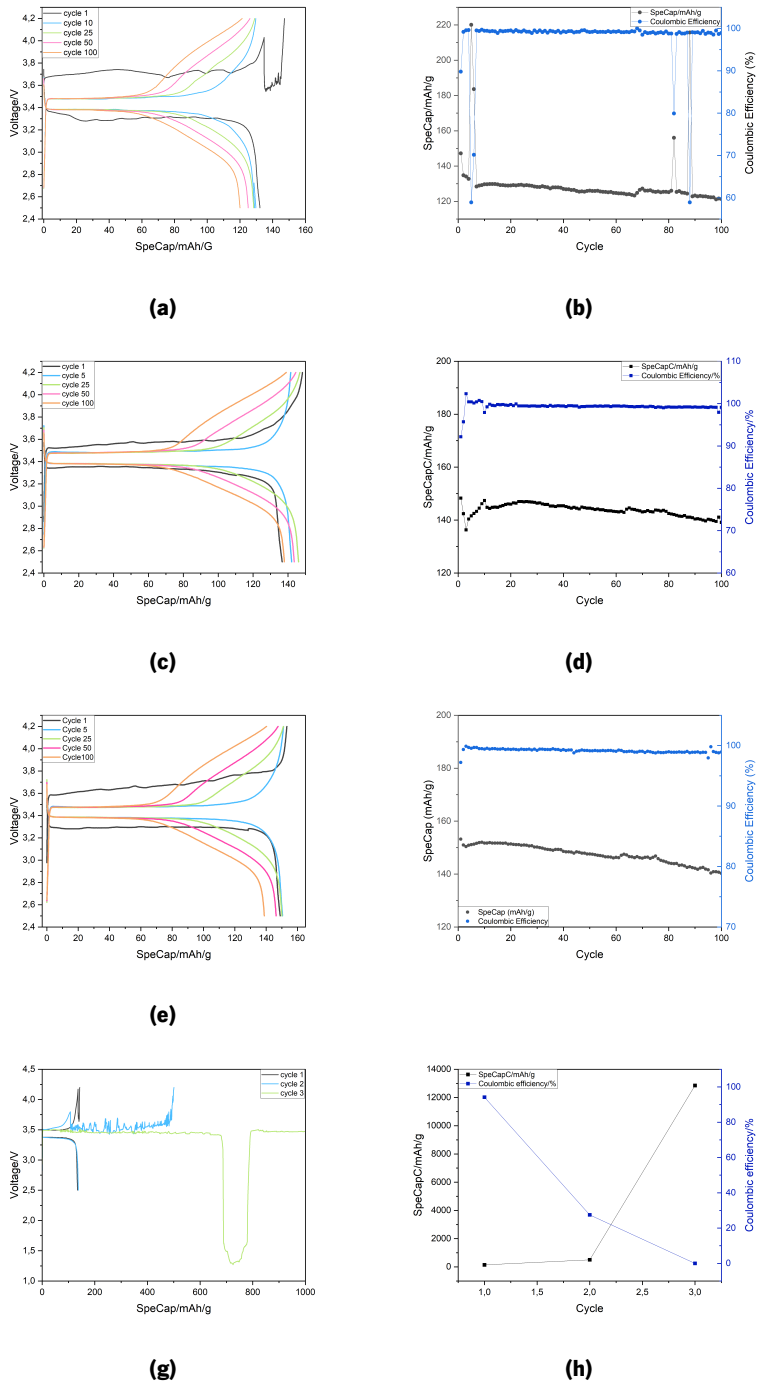

Figure 14: Charge and discharge curves of solid-state batteries with different SSE cycled at C/15 between 2.5 and 4.2 V. Battery Cycle Life testing and the respective specific discharge capacity and Coulombic efficiency vs. cycle number. (a) and (b) PVDF-HFP IL SSE sample. (c) and (d) PVDF-HFP IL BTO SSE sample. (e) and (f) PVDF-HFP IL BST SSE sample. (g) and (h) PVDF-HFP IL PZT SSE sample.

Figure 15 depicts the **electrochemical performance of Li/SSE/LFP cells** with three different film compositions, PVDF-HFP/IL, PVDF-HFP/IL/BTO, and PVDF-HFP/IL/BST. Figure 16 shows the capacity of the cells at different C-rates.

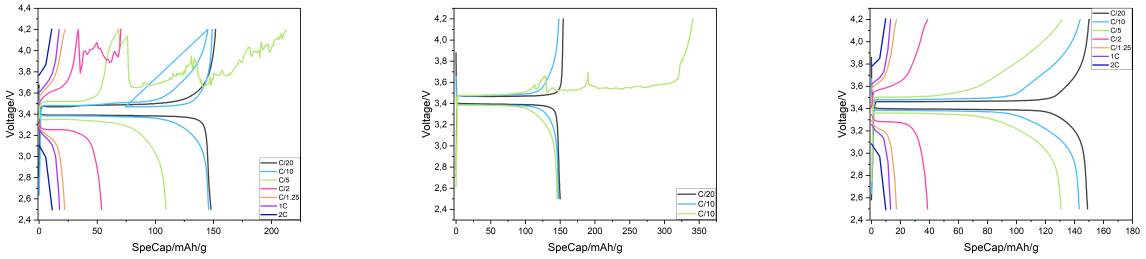

(a) **(b)** **(c)**

Figure 15: Galvanic charge-discharge curves of the Li/SSE/LFP cells. Cycled at C/20 (black), C/10 (blue), C/5 (green), C/2 (pink), C/1.25 (orange), 1C (purple) and 2C (dark blue). The cell was sequentially charged at each C-rate for 10 cycles. The first cycles and the C-rates are labeled on the plot. (a) PVDF-HFP IL; (b) PVDF-HFP IL BTO; (c) PVDF-HFP IL BST.

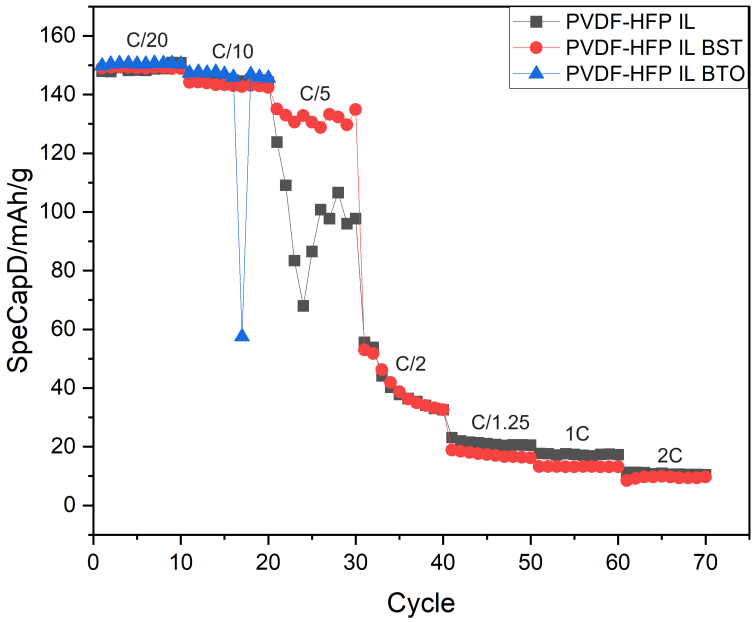

Figure 16: Galvanic charge-discharge curves of the Li/SSE/LFP cells.

On the charge-discharge curves of the cells (Figure 15), the curves show characteristic plateaus of the lithiation and delithiation of LFP at about 3.4V. These values can only be obtained at a very low charge-discharge rate, as for the higher C-rates, the curve slope does not contain a plateau. This shows a clear increase in the charger/discharge overpotential that can be attributed to poor decomposition reaction and low charge transfer kinetics in charge and discharge reactions. This phenomenon translates into a low-performance cathode material (Y. Wang et al., 2020). From the capacity data, it is clear that the SSE sample with BTO as the ceramic filler can not handle high C-rates (> C/10) since it rapidly short-circuits. Unlike what was expected PVDF-HFP/IL shows a slightly higher capacity than the SSE with ceramic filler, yet the specific capacity value does not represent a significant difference. Thus, at C/5 the PVDF-HFP/IL showed an unstable behavior, and PVDF-HFP/IL/BST showed good performance at all C-rates, which contributes to the premise that the doped SSE is more stable. At C/2, the capacity drops more than 50%, and for higher C-rates, both cells barely have capacity, a phenomenon that goes accordingly to Peukert's law, that at higher C-rates, the effective capacity of the battery diminishes faster than at lower C-rates. In this work capacity losses may be related to the solid-electrolyte interface (SEI) layer and gas formation that can occur due to increased electrolyte decomposition. Additionally, these limitations in high charge and discharge rates might be due to electrolyte depletion (Gupta, Mehta, Bahga, & Gupta, 2022) (O'Hanlon, McNulty, Tian, Coleman, & O'Dwyer, 2020) (Li, Wang, & Pecht, 2019).

6.3 Numerical results - Comparison between the 0-D model and experiment

In this section, we show the different results obtained from the developed model (depicted in Chapter 5) using the MATLAB R2023b software. The model was tested by implementing different C-rates, which allowed the visualization of different parameters, such as lithium metal and oxide concentration (C_{Li} and C_{0x}), lithium-ion concentration (c_{ia} and c_{ic}), intensity (I_{tot}), resistance(R_{ext}), and potential (ϕ_a and ϕ_i). This model is applied to a solid-state Li-ion battery.

Numerical conditions

For the numerical simulation, different numerical conditions were prescribed. In order to approximate the simulation to the experimental results the intensity was kept constant, for that a target intensity was selected (corresponding to a 1C-rate), and then several C-rates were applied. By doing so, the resistance was forced to adapt to the fixed intensity. Additionally, in a battery, the initial ion concentration is established during the assembly process. When a battery is compiled, there is the addition of liquid electrolyte (a very small amount as the battery is in a solid state). These initial ion concentrations are carefully controlled to ensure the battery's proper functioning and capacity. And so, the initial concentration was set to a value different from zero, in this case, 1200 mol/m^3. Table 6.4 depicts the main characteristics of the numerical simulations.

Table 6.4: Parameters used for the simulations of the battery's geometry.

Characteristic Values			
Characteristic surface of the anode	$(9e-3)^2 \times \pi$ (m)	Diffusion coeficiente	$2e-12\ m^2/s$
Characteristic surface of the cathode	$(7e-3)^2 \times \pi\ (m)$	Anode open circuit potential	-3.4 V
Characteristic length factor of the anode	$e^5(m)$	Cathode open circuit potential	$0.05\ V$
Characteristic length factor of the cathode	$e^3(m)$	Porosity (in both cathode and anode)	0.4
Anode specific length (thickness)	$500\ \mu m$	BV kinetic rate transfer anode for charge	$3e-11$
Cathode specific length (thickness)	$40\ \mu m$	BV kinetic rate transfer cathode for charge	$3e-11$
Solid electrolyte specific length (thickness)	$50\ \mu m$	BV kinetic rate transfer anode for discharge	$3e-12$
Lithium transfer number	0.9	BV kinetic rate transfer cathode for discharge	$3e-11$
BV maximum metal lithium concentration	$5000\ mol/m^3$	BV maximum oxide lithium concentration	$30000\ mol/m^3$
Initial metal concentration	$10000\ mol/m^3$	Li^+ concentration in the solid electrolyte	$1200\ mol/m^3$
Initial oxide lithium concetration	$1000\ mol/m^3$		

6.3.1 Results for Charge-Discharge Conditions

In order to attain the different C-rate charging and discharging outputs, a Target Intensity ($I_{tot} = I_{Target}$) is set, and so, the resistance would vary in order to maintain the intensity value. The C-rate, often symbolized as "C", is a measurement used in the field of battery technology to describe the speed at which a battery is charged or discharged in relation to its capacity. It's a dimensionless parameter expressed as the ratio of the charging or discharging current (measured in amperes, A) to the battery's capacity (usually in ampere-hours, Ah, or watt-hours, Wh) (Buchmann, 2001).

- C/10-rate numerical tests

When applying a C/10-rate we obtained the following results illustrated in Figure 17. We have in the top row, respectively, the graph of the concentration of Lithium-ion in the cathode and in the anode, the concentration of Lithium and Oxide, and the potential in the anode and in the cathode all over time (in hours). In the bottom row, we have the intensity and resistance over time, respectively.

The graphs depict a charging and discharging regimen characterized by a C/10-rate, meaning that a complete

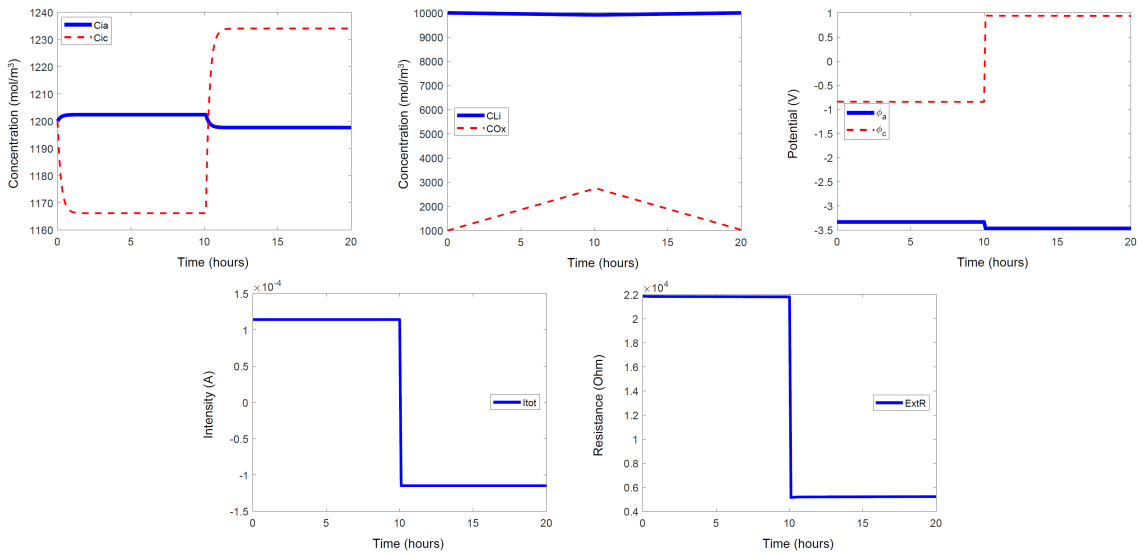

Figure 17: Graphic output of the simulation with C/10-rate. 1 cycle of charge and discharge (20 hours).

charge cycle spans 10 hours, followed by a subsequent 10-hour period for a full discharge. As a result, the entire process of charging and discharging the battery encompasses a 20-hour interval. During the discharging phase, the ionic concentration at the cathode (c_{ic}) experiences an initial decline until it stabilizes at a plateau, approximately at 1165 mol/m^3. This initial drop is attributed to the onset of the chemical reaction of delithiation, wherein Li-ions within the electrolyte swiftly migrate to the cathode, additionally, the ones present at the effective surface are also consumed. The ion concentration (c_{ia}) in the anode reveals an inverse behavior because, at a discharge rate, the ions migrate to the positive electrode. Consequently, the concentration of the oxide material (C_{Ox}) increases in the initial 10-hour (from 1000 to 3000 mol/m^3) duration while the lithium metal (C_{Li}) decreases - this effect might not be visible in the graph as the anode has significantly higher dimensions than the cathode. This indicates that the primary reaction occurring at this stage is:

$$Li_nC_6 + Li_{m-n}FePO_4 \longrightarrow Li_0C_6 + Li_mFePO_4 \tag{6.2}$$

At the 10-hour mark, there is a clear shift in the chemical reaction typically associated with the charging mode. The ionic concentration shift occurs in the same manner as the discharging mode, however, the Li-ions move towards the anode (negative electrode). This movement triggers an increased ionic consumption in the negative pole, while at the cathode (positive electrode) there is a release of ions. This explains the curve behavior, illustrating the inverse chemical reaction present in Equation (6.2).

Remark 6.3.1: Note that the lithium-ion concentration (c_{ia} and c_{ic}) starts at a concentration of 1200 mol/m^3. This is due to the fact that the electrolyte also has a Li-ion concentration that needs to be accounted for.

With the C/15-rate, we get a lower kinetic reaction, meaning that the lithiation-delithiation process occurs in a slow and controlled process. This is correlated to the slow consumption of Li-ions, which favors a high capacity of the

battery and higher stability of the model.

As stated in Chapter 5 the potential in the anode and cathode was maintained constant at charge and discharge. In an experimental scenario during the charging of a battery, the potential (voltage) across its terminals increases. This is because energy in the form of electrical current is converted and stored as chemical energy within the battery. When the battery is discharged, the potential decreases. This is because the stored chemical energy is being released as electrical energy.

As for the intensity and resistance graphs, there is stability at certain values. For discharging we get a value of around $I_{tot} = -1.14 \times 10^{-4}$ A which is the characteristic value for the implemented C-rate. We get the symmetrical value for charging. As for resistance R_{ext}, it shifts between 18000Ω (discharging) and 4000Ω (charging).

Remark 6.3.2: For this simulation, the intensity signal (positive and negative) is determined by the electron movement at charge and discharge.

A parallel experiment was done in order to understand long cycling at this rate, with the $t = 320$ hours. We repost in Figure 18 the concentration of the Lithium and Oxide (left panel) together with the ionic concentration (right panel).

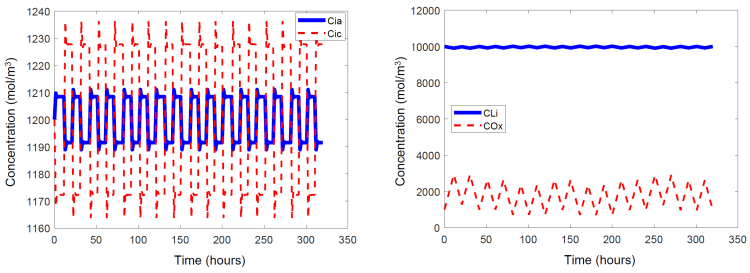

Figure 18: Graphic output of the simulation with C/10. Long cycling of charge and discharge (320 hours).

Overall no differences in the ϕ_a, ϕ_c, I_{tot}, and R_{ext} were noted, the only difference being the applied time and higher number of cycles. In the long cycling, we can see a long-term effect on the concentrations. The Li-ion concentrations (c_{ia} and c_{ic}) develop a peak at the maximum and minimum concentration. This phenomenon is due to a high ion consumption at the electrodes, which leads to the creation of a potential inside the electrolyte. This occurrence is not modulated by the 0D model, consequently triggering an error associated with this model.

- 1C-rate numerical testing

For comparison purposes, the 1C rate was tested. This C-rate is higher, meaning that the ion consumption is faster, leading to rapid ion depletion. The results are in the following Figure 19. We have in the top row, the graph of the concentration of Lithium-ion in the cathode and in the anode, the concentration of Lithium and Oxide, and the potential in the anode and in the cathode all over time (in hours), respectively. In the bottom row, we have the intensity and resistance over time, respectively.

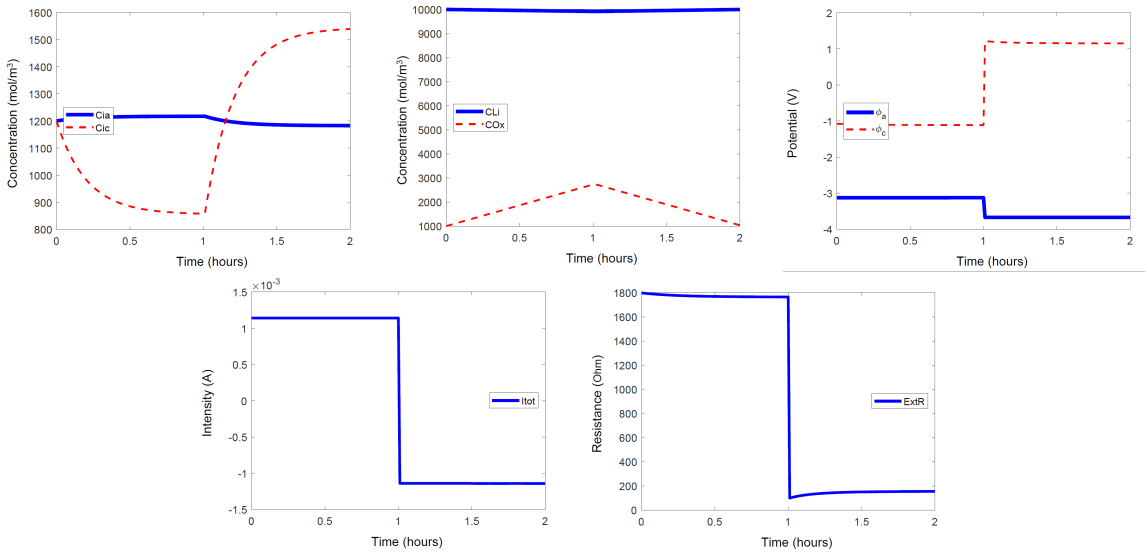

Figure 19: Graphic output of the simulation with 1C. 1 cycle of charge and discharge (2 hours).

It is clear that there is a significant difference in the concentration curves' behavior. There is no clear plateau in the Li-ion lithiation-delithiation curve, this is explained by the rapid migration of Li-ions, as the intensity is higher ($|1.14 \times 10^{-}3|$A) and resistance lower (1800Ω for discharge and 200Ω for a charge). The Li-ion concentration reaches a value of 850 mol/m^3, a significantly higher value when compared to the C/10 cycle. Interestingly, the oxide concentration reaches a similar value to the previous condition. This phenomenon is due to the chemical reaction kinetics. This translates into a high production of Li-ions, but the cathode does not have the capacity to uptake all of this ion migration (most likely the ions remain in the electrolyte).

Results concerning ϕ_a, ϕ_c, I_{tot} and R_{ext} show similar curves to the previous C/10 results.

On the other hand, when applying long cycling to the 1C condition the cycling showed relatively stable concentration curves (Figure 20). It illustrates the concentration of the Lithium and Oxide (left panel) together with the ionic concentration (right panel).

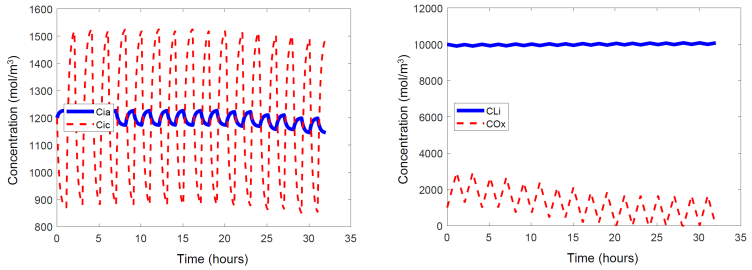

Figure 20: Graphic output of the simulation with 1C. Long cycling of charge and discharge (32 hours).

The Li-ion consumption and creation do not develop a problem in the long term, because there is less time for the kinetic process to occur. Consequently, the peaks are not present in this type of cycling.

- 2C-rate numerical testing

The 2C rate bears a numerical problem for the method, it revealed the need for a very low resistance when charging (<100Ω). Therefore the fixed point numerical procedure can not operate under this condition, revealing a high computational demand. For this reason, this model is not yet suitable for simulating high C-rates (>1C-rate).

- C-rates variations benchmarks

Finally, we varied the C-rate, in order to study the effect of the different intensities in the different parameters. The different C-rates applied were the following C/10, C/5, C/2, C/1.25, and 1C (Figure 21). (The same image scattering as the other C-rates numerical analysis, is presented here.)

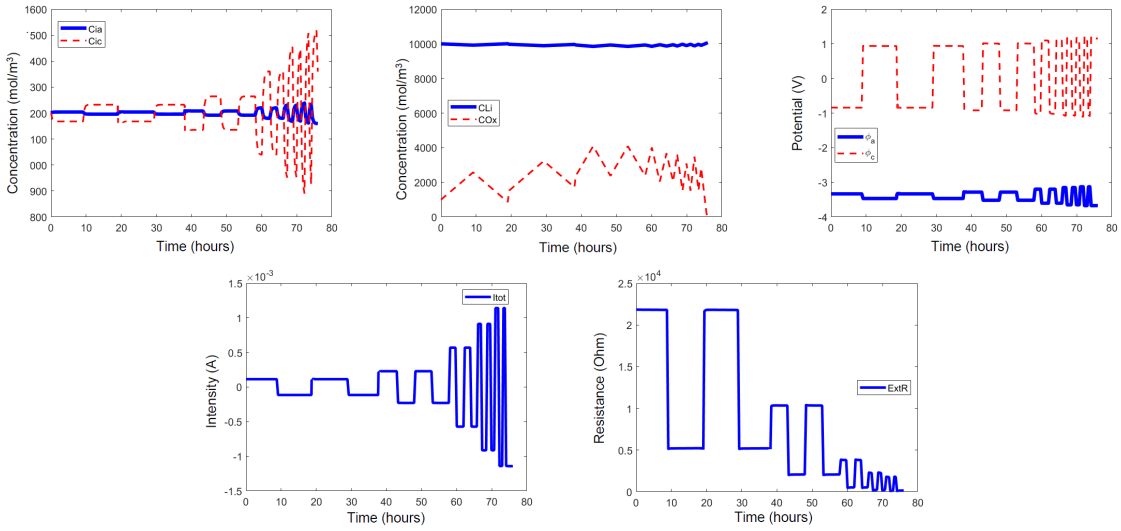

Figure 21: Graphic output of the simulation with variable C-rate. 2 cycles of charge and discharge for each C-rate applied (C/10, C/5, C/2, C/1.25, 1C).

We can conclude that the behavior of this cell is significantly different. Concerning the ionic concentration (c_{ia} and c_{ic}) there is a clear increase in the Li-ion presence at higher C-rates, consequently the ion mobility in the domain increases. On the one hand, we see a slight increase in oxide concentration, on the other hand, this concentration, clearly does not follow the same tendency as the Li-ion concentration, as this value does not shift from around (2000-4000 mol/m^3) in fact by the end of the simulation, at higher C-rates this value seems to diminish slightly. This can represent a lower uptake of Li-ions on the cathode side since the lower oxides are being generated.

The intensity I_{tot} and resistance R_{ext} translate the clear difference between the applied C-rate and the different intensities or resistance values necessary to obtain the achieved data.

Conclusion and future perspectives

In this comprehensive exploration, our thesis ventured into various scientific domains, bringing together experimentation and theoretical analysis to shed light on the intriguing realm of solid-state electrolytes (SSE) for lithium-ion batteries. Our findings serve as a valuable contribution to the ever-evolving landscape of energy storage technology.

From the realm of experimentation, we delved into the intricate world of SSE, examining the impact of distinct compounds on their performance. Among our compelling discoveries, SSE formulations featuring PVDF-HFP/IL combined with ceramics exhibited notably enhanced ionic conductivity and overall performance. Uniquely, the introduction of ceramic fillers, particularly BTO and BST, proved to be a pivotal factor in battery cycle life testing. Here, we witnessed increased capacity (values of 148.2 and 153 mAh/g, respectively), unwavering stability, high ionic conductivity (1.34 $\times 10^{-5}$ and 4.36 $\times 10^{-6}$ S/cm, respectively) and a remarkable absence of significant capacity degradation over time.

Yet, a captivating twist emerged when subjecting these cells to the rigorous demands of capacity testing, specifically under escalating C-rates. The SSE with PVDF-HFP/IL/BTO revealed its limitations, struggling to cope with the demands of high C-rates. Conversely, the SSE PVDF-HFP/IL/BST exhibited remarkable resilience and capacity, succeeding during battery capacity testing. These results underscore the pivotal role played by these piezoelectric elements in enhancing SSE stability, ultimately delivering a superior performance.

In parallel with the experimental insights, the theoretical analysis unveiled the intricate physical and chemical processes unfolding within the battery. Our discerning exploration of the effects of varying C-rates over time provided illuminating aspects. We observed that as C-rates increased, the charge and discharge times decreased, although at the cost of slower lithium ion transfer and diminished charging efficiency.

These highlights bear significance for the scientific community and the broader domain of energy storage technology. The incorporation of ceramics, notably BST, into SSE holds promise as a means to elevate stability. Moreover, our pursuit of numerical analysis contributes to a deeper understanding of battery behavior across diverse operational scenarios, illuminating pathways to enhance battery technology.

As we conclude this chapter, the horizon beckons with exciting prospects for future research. Refinement of our model to accommodate high C-rates and the evolution of our numerical analysis to more complex one-dimensional models, such as the Single Particle Model, lie on the research frontier. The exploration of varying solid electrolyte interface (SEI) layers, and perhaps novel casting methods, promises to unearth new insights. Additionally, the fine-tuning of ceramic particle concentrations within SSE formulations offers an avenue for optimization. With these

directions, we continue to propel the science of energy storage forward, fostering innovations that will power a sustainable future.

In summary, this thesis stands as a testament to the remarkable synergy of experimental and theoretical pursuits, charting a course toward a brighter, more sustainable energy landscape.

Bibliography

Abbrent, S., Plestil, J., Hlavata, D., Lindgren, J., Tegenfeldt, J., & Wendsjö, Å. (2001). Crystallinity and morphology of pvdf–hfp-based gel electrolytes. *Polymer*, *42*(4), 1407–1416.

Agrawal, R., & Pandey, G. (2008). Solid polymer electrolytes: materials designing and all-solid-state battery applications: an overview. *Journal of Physics D: Applied Physics*, *41*(22), 223001.

Aliahmad, N., Shrestha, S., Varahramyan, K., & Agarwal, M. (2016). Poly (vinylidene fluoride-hexafluoropropylene) polymer electrolyte for paper-based and flexible battery applications. *AIP Advances*, *6*(6).

Ara, K. N. I., Rahaman, M. M., & Alam, M. S. (2021). Numerical solution of advection diffusion equation using semi-discretization scheme. *Applied Mathematics*, *12*(12), 1236–1247.

Aravindan, V., Vickraman, P., & Kumar, T. P. (2008). Polyvinylidene fluoride–hexafluoropropylene (pvdf–hfp)-based composite polymer electrolyte containing lipf3 (cf3cf2) 3. *Journal of non-crystalline solids*, *354*(29), 3451–3457.

Association, W. N. (2022). *Carbon dioxide emissions from electricity.* (https://world-nuclear.org/information-library/energy-and-the-environment/carbon-dioxide-emissions-from-electricity.aspx)

Banerjee, A., & Bose, S. (2004). Free-standing lead zirconate titanate nanoparticles: low-temperature synthesis and densification. *Chemistry of materials*, *16*(26), 5610–5615.

Baranchugov, V., Markevich, E., Pollak, E., Salitra, G., & Aurbach, D. (2007). Amorphous silicon thin films as a high capacity anodes for li-ion batteries in ionic liquid electrolytes. *Electrochemistry communications*, *9*(4), 796–800.

Barbosa, J., Correia, D., Gonçalves, R., de Zea Bermudez, V., Silva, M. M., Lanceros-Mendez, S., & Costa, C. (2021). Enhanced ionic conductivity in poly (vinylidene fluoride) electrospun separator membranes blended with different ionic liquids for lithium ion batteries. *Journal of Colloid and Interface Science*, *582*, 376–386.

Bates, A., Mukherjee, S., Schuppert, N., Son, B., Kim, J. G., & Park, S. (2015). Modeling and simulation of 2d lithium-ion solid state battery. *International Journal of Energy Research*, *39*(11), 1505–1518.

Becker-Steinberger, K., Funken, S., Landstorfer, M., & Urban, K. (2010). A mathematical model for all solid-state lithium-ion batteries. *ECS Transactions*, *25*(36), 285.

Bhalla, A. S., Guo, R., & Alberta, E. F. (2002). Some comments on the morphotropic phase boundary and property diagrams in ferroelectric relaxor systems. *Materials Letters*, *54*(4), 264–268.

Bhatt, N. (2011). Model-based estimation of state of charge of lithium cells.

Bischoff, C., Schuller, K., Dunlap, N., & Martin, S. W. (2014). Ir, raman, and nmr studies of the short-range structures of 0.5 na2s+ 0.5 [x ges2+(1–x) ps5/2] mixed glass-former glasses. *The Journal of Physical Chemistry B*, *118*(7), 1943–1953.

Blomgren, G. E. (2016). The development and future of lithium ion batteries. *Journal of The Electrochemical Society*, *164*(1), A5019.

Boddula, R., Pothu, R., Asiri, A. M., et al. (2020). *Rechargeable batteries: History, progress, and applications*. John Wiley & Sons.

Boukamp, B. A., Pham, M. T., Blank, D. H., & Bouwmeester, H. J. (2004). Ionic and electronic conductivity in lead–zirconate–titanate (pzt). *Solid State Ionics*, *170*(3-4), 239–254.

Boutarfaia, A. (2000). Investigations of co-existence region in lead zirconate-titanate solid solutions: X-ray diffraction studies. *Ceramics International*, *26*(6), 583–587.

Buchmann, I. (2001). Batteries in a portable world: a handbook on rechargeable batteries for non-engineers.

Buscaglia, V., Buscaglia, M. T., & Canu, G. (2021). Batio3-based ceramics: Fundamentals, properties and applications.

Cai, X., Lei, T., Sun, D., & Lin, L. (2017). A critical analysis of the α, β and γ phases in poly (vinylidene fluoride) using ftir. *RSC advances*, *7*(25), 15382–15389.

Castle, M. J. (2023). *Mathematical modelling of lithium iron phosphate electrodes* (Unpublished doctoral dissertation). University of Portsmouth.

Chaipanich, A. (2007). Effect of pzt particle size on dielectric and piezoelectric properties of pzt–cement composites. *Current Applied Physics*, *7*(5), 574–577.

Chakraborty, A., Dixit, M., Aurbach, D., & Major, D. T. (2018). Predicting accurate cathode properties of layered oxide materials using the scan meta-gga density functional. *npj Computational Materials*, *4*(1), 60.

Chen, R., Qu, W., Guo, X., Li, L., & Wu, F. (2016). The pursuit of solid-state electrolytes for lithium batteries: from comprehensive insight to emerging horizons. *Materials Horizons*, *3*(6), 487–516.

Chen, X., & Vereecken, P. M. (2019). Solid and solid-like composite electrolyte for lithium ion batteries: engineering the ion conductivity at interfaces. *Advanced Materials Interfaces*, *6*(1), 1800899.

Cheruvally, G. (2008). Lithium iron phosphate: a promising cathode-active material for lithium secondary batteries. *Lithium Iron Phosphate*, 1–148.

Choudhury, N., & Patterson, J. (1971). Performance characteristics of solid electrolytes under steady-state conditions. *Journal of The Electrochemical Society*, *118*(9), 1398.

Colomines, G., Decaen, P., Lourdin, D., & Leroy, E. (2016). Biofriendly ionic liquids for starch plasticization: a screening approach. *RSC advances*, *6*(93), 90331–90337.

Dallaev, R., Pisarenko, T., Sobola, D., Orudzhev, F., Ramazanov, S., & Trčka, T. (2022). Brief review of pvdf properties and applications potential. *Polymers*, *14*(22), 4793.

Dias, F. B., Plomp, L., & Veldhuis, J. B. (2000). Trends in polymer electrolytes for secondary lithium batteries. *Journal of Power Sources*, *88*(2), 169–191.

Do, J.-S., Chang, C.-P., & Lee, T.-J. (1996). Electrochemical properties of lithium salt-poly (ethylene oxide)-ethylene carbonate polymer electrolyte and discharge characteristics of limno2. *Solid State Ionics*, *89*(3-4), 291–298.

Doeff, M. (2012, 01). Batteries: Overview of battery cathodes. In (p. 709-739).

Dudney, N. J. (2005). Solid-state thin-film rechargeable batteries. *Materials Science and Engineering: B*, *116*(3), 245–249.

Esfahanian, V., Dalakeh, M. T., & Aghamirzaie, N. (2019). Mathematical modeling of oxygen crossover in a lithium-oxygen battery. *Applied Energy*, *250*, 1356–1365.

for Biotechnology Information, N. C. (2023a). *Pubchem compound summary for cid 159419, barium titanium oxide.* https://pubchem.ncbi.nlm.nih.gov/compound/Barium-titanium-oxide. (Retrieved October 31, 2023)

for Biotechnology Information, N. C. (2023b). *Pubchem compound summary for cid 159452, lead titanium zirconium oxide.* https://pubchem.ncbi.nlm.nih.gov/compound/Lead-titanium-zirconium-oxide. (Retrieved October 31, 2023)

for Biotechnology Information, N. C. (2023c). *Pubchem compound summary for cid 6228, n,n-dimethylformamide.* https://pubchem.ncbi.nlm.nih.gov/compound/N$_N$ − $Dimethylformamide.(RetrievedOctober31, 2023)$

for Biotechnology Information, N. C. (2023d). *Pubchem compound summary for cid 6369, vinylidene fluoride.* https://pubchem.ncbi.nlm.nih.gov/compound/Vinylidene-fluoride. (Retrieved October 31, 2023)

for Biotechnology Information, N. C. (2023e). *Pubchem substance record for sid 440788327, 12430-73-8, source: Alfa chemistry.* https://pubchem.ncbi.nlm.nih.gov/substance/440788327. (Retrieved October 31, 2023)

Franco, A. A. (2013). Multiscale modelling and numerical simulation of rechargeable lithium ion batteries: concepts, methods and challenges. *Rsc Advances*, *3*(32), 13027–13058.

Gao, J., Xue, D., Liu, W., Zhou, C., & Ren, X. (2017). Recent progress on batio3-based piezoelectric ceramics for actuator applications. In *Actuators* (Vol. 6, p. 24).

Gebreyesus, M. A., Purushotham, Y., & Kumar, J. S. (2016). Preparation and characterization of lithium ion conducting polymer electrolytes based on a blend of poly (vinylidene fluoride-co-hexafluoropropylene) and poly (methyl methacrylate). *Heliyon*, *2*(7).

GSaiz, P., Lopes, A. C., Barker, S. E., de Luis, R. F., & Arriortua, M. I. (2018). Ionic liquids for the control of the morphology in poly (vinylidene fluoride-co-hexafluoropropylene) membranes. *Materials & Design*, *155*, 325–333.

Guo, Y., Wu, S., He, Y.-B., Kang, F., Chen, L., Li, H., & Yang, Q.-H. (2022). Solid-state lithium batteries: Safety and prospects. *EScience*, *2*(2), 138–163.

Gupta, R., Mehta, R., Bahga, S. S., & Gupta, A. (2022). (digital presentation) thermal behaviour prediction of commercial lithium-ion cells under different c-rate and ambient conditions using surrogate modelling. In *Electrochemical society meeting abstracts 241* (pp. 389–389).

Han, T.-H., Nirmala, R., Kim, T. W., Navamathavan, R., Kim, H. Y., & Park, S. J. (2016). Highly aligned poly (vinylidene fluoride-co-hexafluoro propylene) nanofibers via electrospinning technique. *Journal of Nanoscience and Nanotechnology*, *16*(1), 595–600.

Hasegawa, R., Takahashi, Y., Chatani, Y., & Tadokoro, H. (1972). Crystal structures of three crystalline forms of poly (vinylidene fluoride). *Polymer Journal*, *3*(5), 600–610.

Hayes, R., Warr, G. G., & Atkin, R. (2015). Structure and nanostructure in ionic liquids. *Chemical reviews*, *115*(13), 6357–6426.

Hazra, S., Ghatak, A., Ghosh, A., Sengupta, S., Raychaudhuri, A., & Ghosh, B. (2022). Enhanced piezoelectric response in bto nws-pvdf composite through tuning of polar phase content. *Nanotechnology*, *34*(4), 045405.

He, W., Pecht, M., Flynn, D., & Dinmohammadi, F. (2018). A physics-based electrochemical model for lithium-ion battery state-of-charge estimation solved by an optimised projection-based method and moving-window filtering. *Energies*, *11*(8), 2120.

Hirono, T., Usui, H., Domi, Y., Irie, W., Sawada, T., & Sakaguchi, H. (2021). Improvement of the anode properties of lithium-ion batteries for sio x with a third element. *ACS omega*, *7*(1), 1223–1231.

Hu, X., Yan, X., Gong, L., Wang, F., Xu, Y., Feng, L., ... Jiang, Y. (2019). Improved piezoelectric sensing performance of p (vdf–trfe) nanofibers by utilizing bto nanoparticles and penetrated electrodes. *ACS applied materials & interfaces*, *11*(7), 7379–7386.

Hu, X., Zhou, Y., Liu, J., & Chu, B. (2018). Improved flexoelectricity in pvdf/barium strontium titanate (bst) nanocomposites. *Journal of Applied Physics*, *123*(15).

Jayanthi, S., & Sundaresan, B. (2015). Effect of ultrasonic irradiation and tio 2 on the determination of electrical and dielectric properties of peo–p (vdf-hfp)–liclo 4-based nanocomposite polymer blend electrolytes. *Ionics*, *21*, 705–717.

Jiang, Z., Zheng, X., & Zheng, G. (2015). The enhanced electrocaloric effect in p (vdf-trfe) copolymer with barium strontium titanate nano-fillers synthesized via an effective hydrothermal method. *RSC advances*, *5*(76), 61946–61954.

Kang, B.-H., Li, S.-F., Yang, J., Li, Z.-M., & Huang, Y.-F. (2023). Uniform lithium plating for dendrite-free lithium metal batteries: Role of dipolar channels in poly (vinylidene fluoride) and pbzr x ti1–x o3 interface. *ACS nano*, *17*(14), 14114–14122.

Kang, J., Yan, Z., Gao, L., Zhang, Y., Liu, W., Yang, Q., ... Kang, W. (2022). Improved ionic conductivity and enhancedinterfacial stability of solid polymer electrolytes with porous ferroelectric ceramic nanofibers. *Energy Storage Materials*, *53*, 192–203.

Kato, Y., Hori, S., Saito, T., Suzuki, K., Hirayama, M., Mitsui, A., ... Kanno, R. (2016). High-power all-solid-state batteries using sulfide superionic conductors. *Nature Energy*, *1*(4), 1–7.

Kazemi, N., Danilov, D. L., Haverkate, L., Dudney, N. J., Unnikrishnan, S., & Notten, P. H. (2019). Modeling of

all-solid-state thin-film li-ion batteries: Accuracy improvement. *Solid State Ionics*, *334*, 111–116.

Kerman, K., Luntz, A., Viswanathan, V., Chiang, Y.-M., & Chen, Z. (2017). Practical challenges hindering the development of solid state li ion batteries. *Journal of The Electrochemical Society*, *164*(7), A1731.

Khardazi, S., Zaitouni, H., Asbani, B., Mezzane, D., Amjoud, M., Choukri, E., ... Gagou, Y. (2022). Structural, dielectric, ferroelectric and electrical properties of lead-free ba0. 9sr0. 1ti0. 9sn0. 1o3 ceramic prepared by sol–gel method. *Materials Today: Proceedings*, *51*, 2059–2065.

Knauss, L., Pond, J., Horwitz, J., Chrisey, D., Mueller, C., & Treece, R. (1996). The effect of annealing on the structure and dielectric properties of ba x sr1- x tio3 ferroelectric thin films. *Applied Physics Letters*, *69*(1), 25–27.

Laxmayyaguddi, Y., Mydur, N., Shankar Pawar, A., Hebri, V., Vandana, M., Sanjeev, G., & Hundekal, D. (2018). Modified thermal, dielectric, and electrical conductivity of pvdf-hfp/liclo4 polymer electrolyte films by 8 mev electron beam irradiation. *ACS omega*, *3*(10), 14188–14200.

Li, J., Wang, D., & Pecht, M. (2019). An electrochemical model for high c-rate conditions in lithium-ion batteries. *Journal of Power Sources*, *436*, 226885.

Lian, P.-J., Zhao, B.-S., Zhang, L.-Q., Xu, N., Wu, M.-T., & Gao, X.-P. (2019). Inorganic sulfide solid electrolytes for all-solid-state lithium secondary batteries. *Journal of Materials Chemistry A*, *7*(36), 20540–20557.

Liang, C. (1973). Conduction characteristics of the lithium iodide-aluminum oxide solid electrolytes. *Journal of the Electrochemical Society*, *120*(10), 1289.

Liu, W., Zhang, X., Wu, F., & Xiang, Y. (2017). A study on pvdf-hfp gel polymer electrolyte for lithium-ion batteries. In *Iop conference series: Materials science and engineering* (Vol. 213, p. 012036).

Malmonge, L. F., Malmonge, J. A., & Sakamoto, W. K. (2003). Study of pyroelectric activity of pzt/pvdf-hfp composite. *Materials Research*, *6*, 469–473.

Mao, C., Yan, S., Cao, S., Yao, C., Cao, F., Wang, G., ... Yang, C. (2014). Effect of grain size on phase transition, dielectric and pyroelectric properties of bst ceramics. *Journal of the European Ceramic Society*, *34*(12), 2933–2939.

Marquis, S. G., Sulzer, V., Timms, R., Please, C. P., & Chapman, S. J. (2019). An asymptotic derivation of a single particle model with electrolyte. *Journal of The Electrochemical Society*, *166*(15), A3693.

Mizuno, K., Kimura, Y., Morichika, H., Nishimura, Y., Shimada, S., Maeda, S., ... Ochi, T. (2000). Hydrophobic hydration of tert-butyl alcohol probed by nmr and ir. *Journal of Molecular Liquids*, *85*(1-2), 139–152.

Moura, S. J., Argomedo, F. B., Klein, R., Mirtabatabaei, A., & Krstic, M. (2016). Battery state estimation for a single particle model with electrolyte dynamics. *IEEE Transactions on Control Systems Technology*, *25*(2), 453–468.

News, O. S. (2019). *Energy storage could reduce emissions that cause climate change.* (https://news.osu.edu/energy-storage-could-reduce-emissions-that-cause-climate-change/)

Nishi, Y. (2014). Past, present and future of lithium-ion batteries: Can new technologies open up new horizons? In *Lithium-ion batteries* (pp. 21–39). Elsevier.

Olabi, A., & Abdelkareem, M. (2021). *Energy storage systems towards 2050* (Vol. 219). Elsevier.

OU, D. (2017). State of the art of life cycle inventory data for electric vehicle batteries.

O'Hanlon, S., McNulty, D., Tian, R., Coleman, J., & O'Dwyer, C. (2020). High charge and discharge rate limitations in ordered macroporous li-ion battery materials. *Journal of The Electrochemical Society*, *167*(14), 140532.

Pasuk, I., Nea□u, F., Nea□u, □ , Florea, M., Istrate, C. M., Pintilie, I., & Pintilie, L. (2021). Structural details of batio3 nano-powders deduced from the anisotropic xrd peak broadening. *Nanomaterials*, *11*(5), 1121.

Patla, S. K., Ray, R., Karmakar, S., Das, S., & Tarafdar, S. (2019). Nanofiller-induced ionic conductivity enhancement and relaxation property analysis of the blend polymer electrolyte using non-debye electric field relaxation function. *The Journal of Physical Chemistry C*, *123*(9), 5188–5197.

Pradhan, S., Kumar, A., Sinha, A., Kour, P., Pandey, R., Kumar, P., & Kar, M. (2017). Study of ferroelectric properties on pvdf-pzt nanocomposite. *Ferroelectrics*, *516*(1), 18–27.

Quartarone, E., & Mustarelli, P. (2011). Electrolytes for solid-state lithium rechargeable batteries: recent advances and perspectives. *Chemical Society Reviews*, *40*(5), 2525–2540.

Rached, A., Wederni, M., Khirouni, K., Alaya, S., Martín-Palma, R., & Dhahri, J. (2021). Structural, optical and electrical properties of barium titanate. *Materials Chemistry and Physics*, *267*, 124600.

Raijmakers, L., Büchel, M., & Notten, P. (2018). Impedance-based temperature measurement method for organic light-emitting diodes (oleds). *Measurement*, *123*, 26–29.

Ram, F., Kaviraj, P., Pramanik, R., Krishnan, A., Shanmuganathan, K., & Arockiarajan, A. (2020). Pvdf/batio3 films with nanocellulose impregnation: Investigation of structural, morphological and mechanical properties. *Journal of Alloys and Compounds*, *823*, 153701.

Randall, C., Newnham, R., & Cross, L. (2004). History of the first ferroelectric oxide, batio3. *Materials Research Institute, The Pennsylvania State University, University Park, Pa, USA*, *1*.

Rezzolla, L. (2011). Numerical methods for the solution of partial differential equations. *Lecture Notes for the COMPSTAR School on Computational Astrophysics*, 8–13.

Salminen, J., Papaiconomou, N., Kumar, R. A., Lee, J.-M., Kerr, J., Newman, J., & Prausnitz, J. M. (2007). Physicochemical properties and toxicities of hydrophobic piperidinium and pyrrolidinium ionic liquids. *Fluid Phase Equilibria*, *261*(1-2), 421–426.

Saxena, P., & Shukla, P. (2021). A comprehensive review on fundamental properties and applications of poly (vinylidene fluoride)(pvdf). *Advanced Composites and Hybrid Materials*, *4*, 8–26.

Siebert, F., & Hildebrandt, P. (2008). Theory of infrared absorption and raman spectroscopy. *Vibrational Spectroscopy in Life Science*, 11–61.

Singh, S., Bononi, F., Andreussi, O., Karmodak, N., et al. (2023). Thermodynamic and kinetic modeling of

electrocatalytic reactions using a first-principles approach. *The Journal of Chemical Physics*, *159*(11).

Singh, V. K., Singh, R. K., et al. (2015). Development of ion conducting polymer gel electrolyte membranes based on polymer pvdf-hfp, bmimtfsi ionic liquid and the li-salt with improved electrical, thermal and structural properties. *Journal of Materials Chemistry C*, *3*(28), 7305–7318.

Soroushian, P., Nassar, R.-U.-D., & Balachandra, A. M. (2013). Piezo-driven self-healing by electrochemical phenomena. *Journal of intelligent material systems and structures*, *24*(4), 441–453.

Stephan, A. M., Kumar, S. G., Renganathan, N., & Kulandainathan, M. A. (2005). Characterization of poly (vinylidene fluoride–hexafluoropropylene)(pvdf–hfp) electrolytes complexed with different lithium salts. *European Polymer Journal*, *41*(1), 15–21.

Strauss, F., Bartsch, T., de Biasi, L., Kim, A.-Y., Janek, J., Hartmann, P., & Brezesinski, T. (2018). Impact of cathode material particle size on the capacity of bulk-type all-solid-state batteries. *ACS Energy Letters*, *3*(4), 992–996.

Strauss, W. A. (2007). *Partial differential equations: An introduction*. John Wiley & Sons.

Subianto, S., Mistry, M. K., Choudhury, N. R., Dutta, N. K., & Knott, R. (2009). Composite polymer electrolyte containing ionic liquid and functionalized polyhedral oligomeric silsesquioxanes for anhydrous pem applications. *ACS Applied Materials & Interfaces*, *1*(6), 1173–1182.

Tafur, J. P., Santos, F., & Fernández Romero, A. J. (2015). Influence of the ionic liquid type on the gel polymer electrolytes properties. *Membranes*, *5*(4), 752–771.

Tatsumisago, M., Mizuno, F., & Hayashi, A. (2006). All-solid-state lithium secondary batteries using sulfide-based glass–ceramic electrolytes. *Journal of power sources*, *159*(1), 193–199.

Tian, X., Yi, Y., Yang, P., Liu, P., Qu, L., Li, M., ... Yang, B. (2019). High-charge density polymerized ionic networks boosting high ionic conductivity as quasi-solid electrolytes for high-voltage batteries. *ACS applied materials & interfaces*, *11*(4), 4001–4010.

TIP, T. (n.d.). *Interpreting dsc curves part 1: Dynamic measurements.*

Torabi, F., & Ahmadi, P. (2020). Chapter 2 - fundamentals of batteries. In F. Torabi & P. Ahmadi (Eds.), *Simulation of battery systems* (p. 55-81). Academic Press.

Tran, M.-K., DaCosta, A., Mevawalla, A., Panchal, S., & Fowler, M. (2021). Comparative study of equivalent circuit models performance in four common lithium-ion batteries: Lfp, nmc, lmo, nca. *Batteries*, *7*(3), 51.

Tran, N. T., Vilathgamuwa, M., Farrell, T., et al. (2016). Matlab simulation of lithium ion cell using electrochemical single particle model. In *2016 ieee 2nd annual southern power electronics conference (spec)* (pp. 1–6).

Trevey, J., Jang, J. S., Jung, Y. S., Stoldt, C. R., & Lee, S.-H. (2009). Glass–ceramic li2s–p2s5 electrolytes prepared by a single step ball billing process and their application for all-solid-state lithium–ion batteries. *Electrochemistry communications*, *11*(9), 1830–1833.

Ţucureanu, V., Matei, A., & Avram, A. M. (2016). Ftir spectroscopy for carbon family study. *Critical reviews in*

analytical chemistry, *46*(6), 502–520.

Wang, X., Xiao, C., Liu, H., Huang, Q., & Fu, H. (2018). Fabrication and properties of pvdf and pvdf-hfp microfiltration membranes. *Journal of Applied Polymer Science*, *135*(40), 46711.

Wang, Y., Wang, J., Zhao, X., Qiu, W., Song, E., Zhang, W., ... Liu, J. (2020). Reducing the charge overpotential of li–o 2 batteries through band-alignment cathode design. *Energy & Environmental Science*, *13*(8), 2540–2548.

Wang, Z. J., Aoki, Y., Yan, L. J., Kokawa, H., & Maeda, R. (2004). Crystal structure and microstructure of lead zirconate titanate (pzt) thin films with various zr/ti ratios grown by hybrid processing. *Journal of crystal growth*, *267*(1-2), 92–99.

Wu, J., & Xu, J. (2002). Modeling and simulations for electrochemical power systems. In *Recent progress in computational and applied pdes: Conference proceedings for the international conference held in zhangjiajie in july 2001* (pp. 365–381).

Wu, L., Huang, G., Hu, N., Fu, S., Qiu, J., Wang, Z., ... Tang, S. (2014). Improvement of the piezoelectric properties of pvdf-hfp using agnws. *RSC advances*, *4*(68), 35896–35903.

Yang, H., & Wu, N. (2022). Ionic conductivity and ion transport mechanisms of solid-state lithium-ion battery electrolytes: A review. *Energy Science & Engineering*, *10*(5), 1643–1671.

Yang, J., Yao, X., & Meng, Z. (2022). Investigation of molecular mechanisms of polyvinylidene fluoride under the effects of temperature, electric poling, and mechanical stretching using molecular dynamics simulations. *Polymer*, *245*, 124691.

Yao, P., Yu, H., Ding, Z., Liu, Y., Lu, J., Lavorgna, M., ... Liu, X. (2019). Review on polymer-based composite electrolytes for lithium batteries. *Frontiers in chemistry*, *7*, 522.

Yustanti, E., Hafizah, M., & Manaf, A. (2018). Enhanced dielectric properties of nanocrystalline ba (1-x) srxtio3 (x= 0 and 0.3) ceramics. In *Iop conference series: Earth and environmental science* (Vol. 105, p. 012072).

Yusuf, S. N. F., Yahya, R., & Arof, A. K. (2017). Ionic liquid enhancement of polymer electrolyte conductivity and their effects on the performance of electrochemical devices. *Progress and Developments in Ionic Liquids; Handy, S., Ed.; IntechOpen: London, UK*, 157–183.

Zhang, C., Chen, B., Cai, Z., Zhang, F., Huang, R., Yan, M., ... Pan, H. (2022). Suppressing water clusters by using “hydrotropic” ionic liquids for highly stable aqueous lithium-ion batteries. *Journal of Materials Chemistry A*, *10*(38), 20545–20551.

Zhang, S., Xie, S., & Chen, C. (2005). Fabrication and electrical properties of li3po4-based composite electrolyte films. *Materials Science and Engineering: B*, *121*(1-2), 160–165.

Zhu, Y., Chen, D., Su, Y., Yu, L., Kang, P., Lan, J., ... Sui, G. (2022). Multifunctional gel polymer electrolyte suppressing lithium dendrites and stabling cathodes by asymmetric structural design. *Journal of Electroanalytical Chemistry*, *912*, 116263.